Glacier Surge Dynamics on Western Axel Heiberg Island, Nunavut

Benoît Lauzon

A thesis submitted in partial fulfillment of the requirements for the
Master of Science degree in Geography

Department of Geography, Environment and Geomatics
Faculty of Arts
University of Ottawa

Supervisor
Dr. Luke Copland

Thesis Committee
Dr. Anders Knudby
Dr. Laura Thomson

Abstract

Surge-type glaciers experience cyclical variations between long periods of slow flow, followed by shorter periods of rapid flow. These glaciers have been thoroughly analysed in many regions, but detailed studies of surging in the Canadian Arctic are lacking. This thesis provides the first comprehensive reconstruction of the dynamics of Iceberg and Airdrop glaciers, located on western Axel Heiberg Island, and reveals detailed observations of a surge for the first time in the Canadian Arctic. A variety of remotely sensed data, including historical aerial photographs, declassified intelligence satellite photographs, optical satellite imagery (e.g., ASTER, Landsat), and synthetic aperture radar data (e.g., ERS-1, ERS-2) were used to quantify changes in terminus position, ice velocity, and ice thickness since the 1950s.

A surge initiated at the terminus of Iceberg Glacier in 1981 and terminated in 2003, suggesting an active phase length of 22 years. High surface velocities, peaking at ~2300 m a^{-1} at the terminus in summer 1991, were accompanied by a terminus advance of >7 km over the period 1981–1997 and a large transfer of mass down-glacier, causing significant median surface elevation changes reaching >3 ± 1 m a^{-1} across the entire trunk width. The ensuing quiescent period has seen a continual decrease in flow rates to an average centreline velocity of 11.5 m a^{-1} in 2020–2021, a gradual steepening of the glacier surface, and a terminus retreat of >2.5 km.

Observations on Airdrop Glacier show a continuous advance totalling ~6 km since 1950 and notably less variability in its surface velocities in comparison to Iceberg Glacier. This advance can be attributed to consistently high flow rates of Airdrop's entire surface, resulting in significant thickening near its terminus since at least 1977. However, velocities have more than halved within the last 15 years, but without any clear evidence of previous fast flow events, we cannot confirm whether Airdrop's behaviour is cyclic in nature and therefore characteristic of a surge. Instead, Airdrop Glacier could be experiencing a delayed response to positive mass

balance conditions of the Little Ice Age, and its recent slowdown could be indicative of a gradual adjustment to recent climatic conditions.

Acknowledgements

This thesis has been made possible thanks to the help and support of many people and organisations. First and foremost, I am extremely appreciative of the mentorship, guidance, and unwavering support from my supervisor, Dr. Luke Copland, throughout the last two years. Luke has introduced me to the world of glaciology, provided me with wonderful opportunities, and has inspired me to continue my research journey in the cryospheric sciences. I thank you for being the amazing supervisor and mentor that you are, and I look forward to our continued collaboration.

I would like to thank the University of Ottawa, the University of Manitoba, the Northern Scientific Training Program (NSTP), the Natural Sciences and Engineering and Research Council (NSERC), the Polar Continental Shelf Program (PCSP), the Norwegian-Canadian Remote Sensing of the Cryosphere (RemoteEx) exchange program, and ArcticNet Network of Centres of Excellence Canada for supporting this work.

Although I unfortunately still have not gotten the chance to meet all of you in person due to the pandemic, I am grateful for having such excellent lab mates at the Laboratory for Cryospheric Research. It is always a pleasure to hear about all of your amazing research, to share ideas, and to collaborate.

I would like to highlight that this thesis would not have been possible without the help of the following collaborators: Dr. Wesley Van Wychen, William Kochtitzky, and Dr. Robert McNabb. Your expertise has considerably contributed to the accomplishment of this project, and I am very grateful for all of your assistance. I would also like to thank the advice and participation of my thesis committee members Dr. Laura Thomson and Dr. Anders Knudby.

I would to thank my friends and family for always being there for me. None of this would have been doable without the never ending support from my amazing parents, Marc Lauzon and Pascale Beaulieu, who always encourage me to pursue my dreams and from whom I have inherited my work ethic. I would also like to thank my brother, Nicolas Lauzon, who has always been a great role model, and my friends for their company and for taking my mind off of my work every so often. Merci infiniment!

Last but not least, words cannot express how grateful I am for the support from my amazing partner, Annecy Houston, and for her family who are extremely accommodating and have provided me with a second home throughout this pandemic. I would also like to give a special mention to their two dogs, Pablo and Lupin, who are the cutest little creatures in the world and always brighten up my day. Pablo, thank you for all of your wisdom, love, and cuddles, and Lupin for being so full of energy and silliness. Annecy, thank you for your love, encouragement, and for reminding me to take breaks and get out of the house, go to the gym or on walks with your dogs, or watch our TV shows. You are the best partner that I could ask for, and you always push me to be the best version of myself.

Preface

This thesis is written in article format and is separated into four chapters consisting of an introduction (Chapter 1), followed by two manuscripts in Chapters 2 and 3, and a concluding chapter which provides a summary of the findings derived from the thesis as a whole, as well as suggestions for future work (Chapter 5). Figures are placed directly in the text within their respective section or sub-section, and references for the entire thesis are listed at the end. The two manuscripts are presented in a format ready for submission to peer-reviewed journals, such as *Journal of Glaciology*, with the proposed authorship and titles for the submissions as follows:

1. Lauzon, B., Copland, L., Van Wychen, W., Kochtitzky, W., McNabb, R. (in prep). Dynamics throughout a complete surge cycle of Iceberg Glacier on western Axel Heiberg Island, Canadian High Arctic
2. Lauzon, B., Copland, L., Van Wychen, W., Kochtitzky, W., McNabb, R. (in prep). Evolution in surface morphology and velocity of Airdrop Glacier, western Axel Heiberg Island, over a seven decade long advance.

I was responsible for the majority of the data processing, methodology, and manuscript development with support and suggestions provided by Dr. Luke Copland. Dr. Wesley Van Wychen helped significantly with the development of a GAMMA processing scheme to derive velocities from ERS synthetic aperture radar image pairs; William Kochtitzky processed the ASTER DEMs with the MMASTER Python package on the Canada Compute Cedar super computer, helped with deriving trends from the elevation data, and with geocoding of the surface mass balance data from Noël et al. (2018); Dr. Robert McNabb assisted in troubleshooting issues with the processing of historical air photographs and KH-9 imagery with sPyMicMac, and updated the Python package to meet my needs.

Note that these two manuscripts relied on the same general methods for deriving changes in glacier terminus extent, velocity, and elevation, thus the descriptions in their Methods sections are similar, but this is necessary so that each published paper can be read as a standalone document.

Table of Contents

List of Figures

List of Tables

List of Abbreviations

A.S.L.	Above Sea Level
ASF	Alaska Satellite Facility
ASTER	Advanced Spaceborne Thermal Emission and Reflection Radiometer
auto-RIFT	Autonomous Repeat Image Feature Tracking
CAA	Canadian Arctic Archipelago
DEM	Digital Elevation Model
GIV	Glacier Image Velocimetry
GDEM	Global Digital Elevation Model
GRACE	Gravity Recovery and Climate Experiment
InSAR	Interferometric Synthetic Aperture Radar
ITS_LIVE	Inter-mission Time Series of Land Ice Velocity and Elevation
LIA	Little Ice Age
METI	Ministry of Economy, Trade, and Industry
MMASTER	MicMac ASTER
MSP	Modular SAR Processor
NAPL	National Air Photo Library
NASA	National Aeronautics and Space Administration
NCAA	Northern Canadian Arctic Archipelago
RACMO	Regional Atmospheric Climate Model
RCAF	Royal Canadian Air Force
RGI	Randolph Glacier Inventory
SAR	Synthetic Aperture Radar
SLC	Single Look Complex
USGS	United States Geological Survey
UTM	Universal Transverse Mercator

Chapter 1: Introduction

1.1 Background

Glacier surging is characterized by cyclical ice flow instabilities, whereby a glacier oscillates between long periods of slow flow (quiescent phase, typically for ~10-100 years), followed by short periods of faster flow (active phase, typically for ~1-10 years). Ice velocities usually increase by one or two orders of magnitude during a surge (Meier & Post, 1969), but can be as much as 1000 times greater (Murray et al., 2003). Only around 1% of the world's glaciers have been observed to surge (Jiskoot et al., 1998; Sevestre et Benn, 2015). However, surge-type glaciers have a tendency to cluster within certain regions where a large proportion of glaciers are subject to surging behaviour, such as in parts of Alaska and Yukon, Svalbard, and Greenland (Clarke et al., 1986; Jiskoot et al., 2003).

Glacier surges are generally thought to occur as a result of internally driven oscillations in basal thermal conditions and geometric changes of the glacier during the quiescent phase (Murray et al., 2003; Sevestre & Benn, 2015; Dowdeswell et al., 1995). Therefore, they are widely agreed to be decoupled from external triggers (Meier & Post, 1969; Sharp, 1988). However, Sevestre & Benn (2015), and later Benn et al. (2019a), have shown that surging behaviour is linked to specific combinations of climatic conditions (precipitation, temperature) comprising a well-defined climatic envelope, together with glacier geometry (length, slope), and bed properties (hydraulic conductivity). Climate appears to be the primary control on the location of major surge clusters (Sevestre & Benn, 2015), while geometric variables of glaciers within each surge cluster are strongly correlated with surging behaviour (Clarke et al., 1986; Clarke, 1991; Jiskoot et al., 1998, 2000, 2003; Björnsson et al., 2003; Barrand & Murray, 2006; Grant et al., 2009; Sevestre & Benn, 2015). For example, surge-type glaciers tend to be longer, wider and

to have a lower surface slope than normal glaciers, with the fundamental correlation being between length and surge tendency (Clarke, 1991). More broadly, surges on large glaciers appear to be more common than on smaller ones.

During the quiescent phase, flow rates are below the glacier's balance velocity, which typically causes mass to accumulate over a portion of the glacier in its upper area, referred to as the reservoir zone. Once a surge initiates, ice flow increases to rates significantly greater than the balance velocity, which results in a rapid transfer of mass from its higher elevation reservoir zone to its lower elevation receiving zone (Meier & Post, 1969; Dolgoushin & Osipova, 1975). The location that separates the reservoir zone from the receiving zone, and encounters no net changes in surface elevation during a surge, is defined as the dynamic balance line (Dolgoushin & Osipova, 1975; Kochtitzky et al., 2019; Kochtitzky et al., 2020). A notable advance of a glacier's terminus usually accompanies these significant fluctuations in surface velocity and ice thickness.

Surge-type glaciers are commonly separated into two categories based on their surge mechanisms, focusing on basal processes: 1) Alaska-type surges where the build-up of basal water pressure triggers surge initiation and propagation, and the release of water from the glacier bed causes surge termination (Kamb et al., 1985), and 2) Svalbard-type surges where flow acceleration is driven by a switch from cold to temperate basal conditions as the pressure melting point at the glacier bed is reached following mass buildup during the quiescent phase (Clarke, 1976; Murray et al., 2003). Alaska-type surging glaciers, in regions with relatively temperate climates such as Yukon and Alaska, have shorter surge cycles than Svalbard-type surging glaciers in colder, drier climates. For instance, Donjek Glacier located in the Saint Elias Mountains, Yukon, Canada, is characterized by a short ~12 year surge recurrence interval and a

~2 year active phase (Kochtitzky et al., 2019). Conversely, surge-type glaciers in Svalbard have significantly longer surge cycles of 50–500 years, and longer active phases of 3–10 years (Dowdeswell et al., 1991).

In reality, the distinction between the two proposed surge mechanisms is not always clear as there exists a wide range of complex behaviours, including combined thermo-hydrological triggers (e.g., Dunse et al., 2015; Sevestre et al., 2018; Benn et al. 2019b; Haga et al., 2020). In an attempt to unify different mechanisms through a single framework, Sevestre & Benn (2015) as well as Benn et al. (2019a) propose that balances in both enthalpy and mass flux are necessary for a glacier to remain in a stable steady state. Enthalpy (i.e., the internal energy of a glacier system) thus provides a universal characteristic through which ice flow instabilities can be studied. Gains in enthalpy must match enthalpy losses for a glacier to maintain a stable steady state (Sevestre & Benn, 2015; Benn et al., 2019a). Enthalpy is gained at the glacier bed from geothermal and frictional heating (i.e., expenditure of potential energy), which is a result of ice flow (Benn et al., 2019a). On the other hand, enthalpy losses take place by the conduction of heat from the glacier bed to the atmosphere and the runoff of basal meltwater (Benn et al., 2019a). If water discharge or heat conduction is insufficient to evacuate enthalpy gains at a rate to match enthalpy production, then unstable conditions can arise, making surging more likely (Sevestre & Benn, 2015).

1.2 Research objectives

One of the regions with a relatively high concentration of surge-type glaciers is the Canadian Arctic Archipelago (CAA: Ellesmere, Axel Heiberg, and Devon islands), where 51 surge-type glaciers were first inventoried by Copland et al. (2003). The majority of the surge-

type glaciers that were identified in this study were large tidewater glaciers. Subsequent studies have identified additional surge-type glaciers in this region (e.g., Van Wychen et al., 2016; Van Wychen et al., 2022), and showed that they are the largest of any surge cluster worldwide (Sevestre & Benn, 2015). Current evidence suggests that surge-type glaciers in the Canadian Arctic have decades-long quiescent phases, and a likely active phase length that could vary from anywhere between >5 to >70 years (Van Wychen et al., 2014; Medrzycka et al., 2019; Van Wychen et al., 2021; Van Wychen et al., 2022). However, further investigations into the dynamics of surge-type glaciers in this region are needed to better constrain these numbers.

The primary aim of this thesis is to improve our understanding of surge-type glaciers in the Canadian Arctic and to provide insights into the complex behaviour and dynamics of these glaciers by:

a) Reconstructing the surge history and dynamics of Iceberg and Airdrop glaciers from the mid-20th century to 2021 (i.e., for the last ~70 years) in terms of their terminus position, ice surface velocities and surface elevation.
b) Providing observations throughout a quiescent-active-quiescent surge cycle for the first time in the Canadian Arctic.

These objectives are addressed through the application of remote sensing techniques to a variety of datasets, namely historical aerial photographs, declassified intelligence satellite photographs, optical satellite imagery, and synthetic aperture radar (SAR) data. This thesis provides the first detailed study of a complete surge for a glacier in the Canadian Arctic and new insights into the mechanisms that control surging within this region. The results stemming from this thesis are critical in determining how these mechanisms may be affected by changing climatic conditions. This is, in turn, especially important in order to establish how a warming

climate will affect surge frequency in this region and how iceberg discharge to the ocean will evolve considering that large marine-terminating glaciers in the Canadian Arctic are especially prone to surging (Copland et al., 2003; Sevestre & Benn, 2015).

Chapter 2: Dynamics throughout a complete surge cycle of Iceberg Glacier on western Axel Heiberg Island, Canadian High Arctic

2.1 Introduction

A surge-type glacier experiences quasi-periodic cyclical variations between long periods of slow ice flow during the quiescent phase, followed by shorter periods of considerably faster ice flow during the active phase of a surge. Ice motion during the active phase is typically 10–1000 times faster than during the quiescent phase (Murray et al., 2003). While surge-type glaciers represent ~1% of all glaciers worldwide, they have been found to cluster within particular regions, including the Canadian Arctic (Sevestre & Benn, 2015). The first systematic inventory of surge-type glaciers in the Canadian Arctic Archipelago (CAA: Ellesmere, Axel Heiberg, and Devon islands) compiled by Copland et al. (2003) revealed 51 surge-type glaciers, of which most are large tidewater glaciers. More recent studies have identified additional surge-type glaciers (e.g., Van Wychen et al., 2016; Van Wychen et al., 2022), and Sevestre & Benn (2015) state that 54 (0.46%) of the 11,757 glaciers in the Canadian Arctic at that time were classified as surge-type. The cold and dry climate of the Canadian Arctic falls outside of the optimal climatic envelope for surging, thus there are fewer surge-type glaciers than in locations such as Svalbard (Sevestre & Benn, 2015). However, surge-type glaciers in the CAA tend to be larger than average (Copland et al., 2003; Sevestre & Benn, 2015), and therefore occupy a proportionally larger part of the landscape than their raw numbers would suggest.

The greatest terminus advances of the surge-type glaciers inventoried by Copland et al. (2003) occurred on western Axel Heiberg Island, where Airdrop, Iceberg, and Good Friday glaciers advanced by approximately 4.5, 5, and 7 km, respectively, over the 40-year period from

1959 to 1999. Out of 13 glaciers with signs of unstable flow on Axel Heiberg Island, these three large glaciers were the only confirmed surge-type glaciers (Copland et al., 2003; Medrzycka et al., 2019). While a detailed analysis of the dynamics of Good Friday was undertaken by Medrzycka et al. (2019), showing that the glacier has been continuously advancing for at least the last ~70 years, the long-term changes in terminus position, velocity, and ice thickness of Iceberg and Airdrop glaciers remain largely unknown.

In this study, we reconstruct the surge history of Iceberg Glacier from 1950 to 2021 using a variety of remotely sensed data, including historical aerial photographs, declassified intelligence satellite photographs, optical satellite imagery, and synthetic aperture radar (SAR) data. The terminus positions of Iceberg Glacier from the 1950s to present are combined with changes in ice surface velocities and surface elevation to elucidate its surge behaviour over the past ~70 years. Studies of surge-type glaciers in the Canadian Arctic remain sparse (e.g., Copland et al., 2003; Short & Gray, 2005; Medrzycka et al., 2019; Van Wychen et al., 2021; 2022), in part due to a lack of observations through an entire quiescent-active-quiescent cycle. In this study, we have been able to collate data to provide such an insight for the first time and use it to undertake a thorough analysis of Iceberg Glacier's characteristics, including the length and dynamics of its active phase.

2.2 Study site

Axel Heiberg Island, located in the northern CAA (Figure 2.1), has a total land area of ~43,000 km^2 and a glacierised area of ~11,700 km^2 contained within >1100 glaciers (Ommanney, 1969; Copland et al., 2003). The island is home to two major ice caps: Müller Ice Cap located in the north, and Steacie Ice Cap in the south (Ommanney, 1969). This region has

mean annual temperatures of ~-20˚C and mean annual precipitation ranging from 58 mm a^{-1} at sea level measured at Eureka, 100 km to the east (Figure 2.1) to 370 mm a^{-1} at an elevation of 2120 m a.s.l. (Cogley et al., 1996; Thomson et al., 2017). Glaciological measurements on White Glacier, western Axel Heiberg Island, have taken place since 1959 (Cogley et al., 2011; Thomson et al., 2017).

Iceberg Glacier (79.60˚N, 92.19˚W) is a large tidewater surge-type glacier that drains the west side of Müller Ice Cap (Figure 2.1). Iceberg has a basin size of ~1000 km^2 and a main trunk length of ~35 km (Van Wychen et al., 2016), making it significantly larger than the average surge-type glacier area of 627 km^2 in the Canadian Arctic (Sevestre & Benn, 2015). Iceberg Glacier has been observed in both active and quiescent phases of the surge cycle, the only such glacier out of the three confirmed surge-type glaciers on western Axel Heiberg Island (Van Wychen et al., 2016; Medrzycka et al., 2019).

Although knowledge of Iceberg Glacier's dynamics remain limited, the glacier has been referred to in a handful of papers. It was first deemed to show evidence of a past surge by Ommanney (1969), who reported that in 1959, the glacier was stagnant, its terminus showed retreat characteristics, and extensive potholing of the ice surface extended to at least 10 km up-glacier from its terminus, suggesting that the glacier was in its quiescent phase. By 1992 the glacier had advanced by ~3.5 km, followed by a further advance of ~1.5 km from 1992 to 1999 (Copland et al., 2003). In total, Iceberg Glacier underwent a 21.5 km^2 increase in area from 1959 to 2000 (Thomson et al., 2011). Both 1992 and 1999 satellite imagery reveal intense crevassing and large looped moraines across the lower glacier, with manual tracking of surface features indicating motion of ~4 km between these dates, equivalent to a mean velocity of ~575 m a^{-1} (Copland et al., 2003). Subsequently, the glacier was flowing more slowly in the fall of 2000, but maintained a

relatively rapid flow over its lower 15 km of 75–130 m a^{-1}, followed by a drop to <25 m a^{-1} by midwinter 2004 (Short & Gray, 2005). The ensuing slowdown started at the terminus and propagated up-glacier until ~2010, when the entire glacier trunk became essentially stagnant (Van Wychen et al., 2016). This slowdown was coincident with a terminus retreat of ~1.5–2.5 km between 2000 and 2014, and a decrease in dynamic discharge from 0.03 Gt a^{-1} in 2000 to 0.00 Gt a^{-1} from 2001 to 2015 (Van Wychen et al., 2016). Preliminary evidence from these studies suggests that Iceberg Glacier has an active phase between 10 and 30 years (Medrzycka et al., 2019).

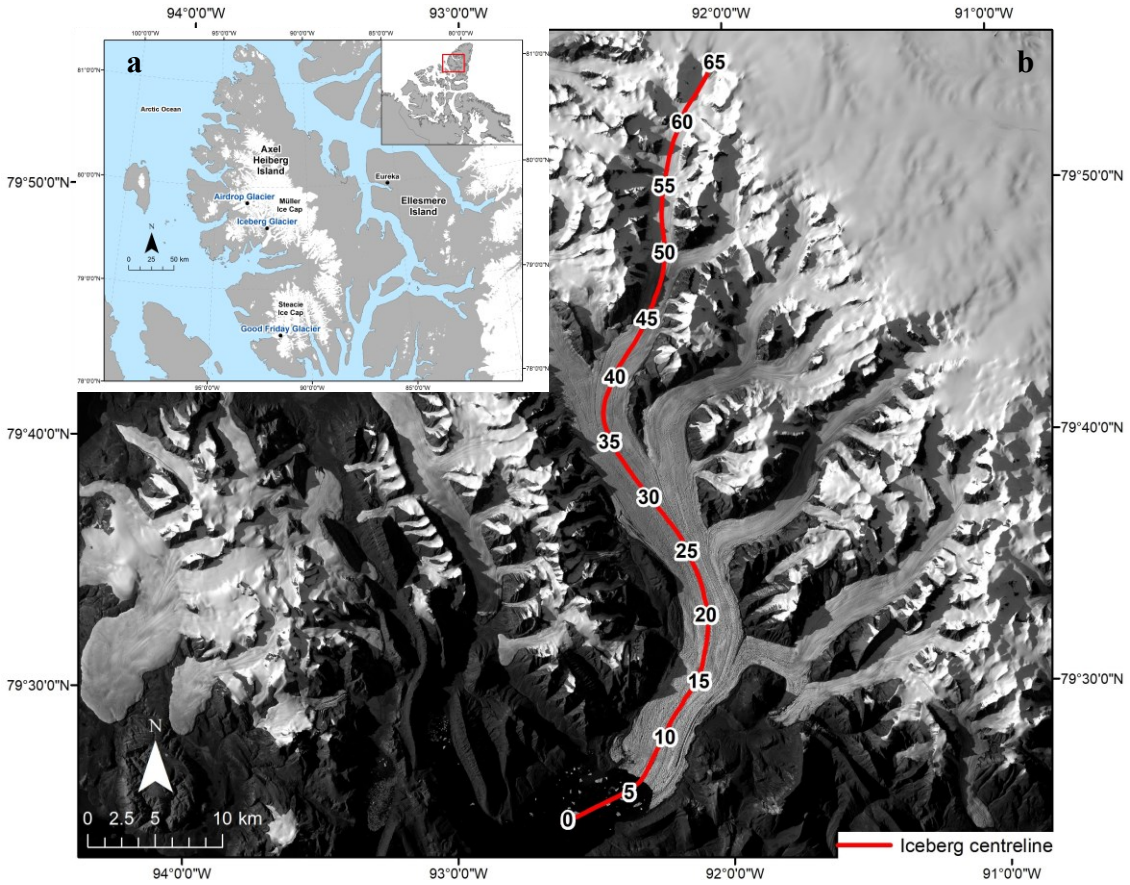

Figure 2.1. (a) Location of Airdrop, Iceberg, and Good Friday Glaciers on Axel Heiberg Island, Nunavut, in the CAA. (b) Iceberg Glacier centreline (red line), with numbers indicating 5 km distance markers starting from the glacier's maximum terminus position in 1997. Base image: Landsat 8, 12 August 2020. Data: Statistics Canada, 2016 Census. Provinces/territories – Cartographic Boundary File (https://www12.statcan.gc.ca/census-recensement/2011/geo/bound-limit/bound-limit-2016-eng.cfm). Natural Resources Canada. Lakes, Rivers and Glaciers in Canada – CanVec Series – Hydrographic Features (https://open.canada.ca/data/en/dataset/9d96e8c9-22fe-4ad2-b5e8-94a6991b744b).

2.3 Methods

2.3.1 Terminus position

Terminus extents of Iceberg Glacier were digitized for the period 1959–2021 using a total of 42 images (Table 2.1). The 1959 terminus position was mapped from a nadir aerial photograph taken at an altitude of ~30,000 ft (~9000 m) a.s.l. by the Royal Canadian Air Force (RCAF). This image was acquired from the National Air Photo Library, Ottawa, Canada. The 1966 terminus outline was mapped from a declassified image from the KH-4 Corona reconnaissance satellite missions, which was ordered from the United States Geological Survey (USGS). The scanned historical aerial photographs and declassified intelligence satellite photos were cropped to cover only the terminus region of Iceberg Glacier and then manually georeferenced using a first order polynomial (affine) transformation and a minimum of 8 tie points in ArcGIS 10.8.1. The terminus positions were then manually outlined in ArcGIS.

All of the terminus positions from 1972 to 2021 were delineated using satellite imagery. European Remote-Sensing Satellite (ERS) synthetic aperture radar (SAR) data from the 1990s was obtained from the Alaska Satellite Facility (ASF; https://search.asf.alaska.edu). These scenes were downloaded in Level 1 (i.e., processed) format and geocoded with the ASF MapReady software. However, some of these scenes were poorly georeferenced and had to be manually adjusted using the Shift tool from the Georeferencing toolbar in ArcGIS to properly align the imagery with recent Landsat 8 scenes. Optical satellite imagery since the 1970s was used from Landsat 1–8, acquired from the USGS Earth Explorer data portal (http://earthexplorer.usgs.gov) in Level 1TP (L1TP; precision and terrain corrected) format. Landsat data products required no pre-processing since L1TP scenes are orthorectified and geometrically/radiometrically corrected. Advanced Spaceborne Thermal Emission and Reflection Radiometer (ASTER) L1T optical

satellite scenes were acquired from USGS Earth Explorer, NASA's Earthdata search (https://search.earthdata.nasa.gov/search), and the METI AIST Data Archive System (https://gbank.gsj.jp/madas/map/index.html). When possible, late summer (July–September) images were selected to ensure minimal snow cover and sea ice. No cloud-free images were available for 1982–1991 other than a single Landsat 5 scene providing partial coverage of Iceberg Glacier's terminus (Table 2.1), resulting in a data gap during that period.

Once all the outlines were completed, the Glacier Termini Change Tracking tool from Urbanski (2018) was used to help determine the mean changes in terminus-wide position between each year. This tool performs a two-dimensional analysis of terminus position changes using a computational geometry algorithm (Urbanski et al., 2018). Total and mean yearly change rates in terminus positions were subsequently quantified for specific periods based on image availability and stages of the surge cycle. A conservative estimate of the maximum uncertainty resulting from the manual delineation of the terminus positions of 2 pixels was determined: 120 m for Landsat 1–3, 60 m for Landsat 4–5, 30 m for Landsat 7–8, 25 m for ERS-1/2, ~12 m for the 1959 historical aerial photograph, and ~8 m for the KH-4 image. Assuming that uncertainties are independent (i.e., caused by random error) and there is no systematic bias, uncertainties for the terminus advance/retreat rate of Iceberg Glacier over the different time periods were calculated from:

$$Uncertainty = \frac{\sqrt{(pixel\ length)^2 + (pixel\ width)^2}}{number\ of\ years} \quad (2.1)$$

Table 2.1. Imagery used for mapping the terminus positions of Iceberg Glacier in this study.

Date of acquisition	Image ID	Resolution (m)	Satellite/Source
25/07/1959	A16753_113	~6	RCAF
14/08/1966	DS1036-1082DF023_d	~4	KH-4 Corona
23/09/1972	LM01L1TP07000119720923	60	Landsat 1
23/05/1973	LM01L1TP06000219730523	60	Landsat 1
19/08/1974	LM01L1TP06300219740819	60	Landsat 1
24/07/1975	LM02L1TP06900119750724	60	Landsat 2
04/09/1976	LM02L1TP06300219760904	60	Landsat 2
29/08/1977	LM02L1TP06200219770829	60	Landsat 2
03/09/1978	LM03L1TP06300219780903	60	Landsat 3
22/09/1979	LM02L1TP06000319790922	60	Landsat 2
30/08/1980	LM02L1TP06100219800830	60	Landsat 2
30/08/1981	LM02L1TP06600219810830	60	Landsat 2
17/04/1984	LM05L1TP05100319840417	60	Landsat 5
09/08/1991	LT05L1TP05300319910809	30	Landsat 5
05/11/1992	E1_06833_STD_F203	12.5	ERS-1
19/08/1993	E1_10941_STD_F204	12.5	ERS-1
07/06/1994	E1_15125_STD_F203	12.5	ERS-1
01/10/1995	LT05L1TP05900219951001	30	Landsat 5
08/04/1997	E2_10278_STD_F203	12.5	ERS-2
24/03/1998	E2_15288_STD_F203	12.5	ERS-2
25/07/1999	LE07L1TP05800219990725	15	Landsat 7
29/09/2000	LE07L1TP05600220000729	15	Landsat 7
19/08/2001	AST_L1T_00308192001200030	15	Terra/ASTER
25/05/2002	AST_L1T_00305252002200046	15	Terra/ASTER
08/07/2003	AST_L1T_00307112003202258	15	Terra/ASTER
20/07/2004	AST_L1T_00307202004003948	15	Terra/ASTER
12/08/2005	AST_L1T_00308122005200430	15	Terra/ASTER
09/07/2006	AST_L1T_00307092006013448	15	Terra/ASTER
15/08/2007	AST_L1T_00308152007193453	15	Terra/ASTER
02/07/2008	LT05L1TP05700220080702	30	Landsat 5
30/07/2009	AST_L1T_00307302009010446	15	Terra/ASTER
12/08/2010	AST_L1T_00308122010014049	15	Terra/ASTER
29/09/2011	AST_L1T_00309292011192136	15	Terra/ASTER
15/09/2012	AST_L1T_00309152012192200	15	Terra/ASTER
11/09/2013	LC08L1TP05600220130911	15	Landsat 8
12/08/2014	LC08L1TP09024220140812	15	Landsat 8
01/09/2015	LC08L1TP05600220150901	15	Landsat 8
29/07/2016	LC08L1TP06000220160729	15	Landsat 8
28/08/2017	LC08L1TP05700220170828	15	Landsat 8
13/09/2018	LC08L1TP05200320180913	15	Landsat 8
19/09/2019	LC08L1TP057002_0190919	15	Landsat 8
07/08/2020	LC08L1TP08724220200807	15	Landsat 8
14/08/2021	LC08L1TP05800220210814	15	Landsat 8

2.3.2 Ice velocities

2.3.2.1 Feature tracking

Landsat 1–3 satellite imagery was used to derive ice surface velocities from 1972 to 1981. The velocities were computed using the Glacier Image Velocimetry (GIV) app developed by Van Wyk de Vries & Wyckert (2021). GIV is an open-source software that provides an easy-to-use interface for rapidly determining high-resolution ice velocities based on a feature-tracking algorithm which matches persistent irregularities on the ice surface between images, which, over time, translate to surface velocity (Van Wyk de Vries & Wyckert, 2021). Velocities were derived from near-annually separated Landsat 1–3 images with the same orbital geometry (i.e., same path and row number) that were subset to a smaller area covering only Iceberg Glacier and its immediate surroundings. Some of the early Landsat images are somewhat poorly georeferenced, even the L1TP products, thus a few Landsat 1–3 images had to be manually shifted, as described in section 2.3.1. This was to ensure that the two images in each pair overlaid each other properly, which helps minimise errors in the resulting velocities.

Subsequently, the velocity data for Iceberg Glacier were filtered based on flow direction. The glacier was separated into two parts where the glacier changes flow direction from approximately SSE to SSW at about 18 km from the terminus, just above the junction between the lowermost tributary and the trunk (Figure 2.1). To account for differences in the flow direction between these two areas, the lower part and the upper part of the glacier were filtered using different values. Cells with a flow direction outside of the range of 150–295˚ for Iceberg's lower part and 100–265˚ for the glacier's upper part were excluded to help filter out false matches. These ranges were chosen to account for ~45˚ in variability relative to the orientation of the centreline in a downstream direction, and for the ice flow at the junctions between tributaries

and trunk. The filtering was undertaken using Raster Calculator in ArcGIS to exclude flow direction cells outside of the specified value range for each part of the glacier, and the Extract by Mask tool was then used to mask the velocity map to the extent of the filtered flow direction map. Automated velocity mapping with Landsat 1–3 imagery can yield relatively large uncertainties (Table 2.2) and incomplete coverage, hence the per-cell mean value for the velocity rasters from 1972 to 1980 was computed to reduce errors and provide complete coverage of the glacier surface. This gives an estimate of Iceberg's pre-surge velocities.

2.3.2.2 GAMMA InSAR

Velocities were derived from ERS-1/2 SAR data for the years 1991, 1992, and 1997. The raw SAR data were downloaded from the ASF website as Level 0 products. Scene pairs with the same orbital geometry (i.e., same path and frame) and a time separation of 12–35 days were acquired. The raw data was then converted to Single Look Complex (SLC) to generate the files required for the computation of displacements using interferometric SAR (InSAR) processing within GAMMA Remote Sensing software. The GAMMA Modular SAR Processor (MSP) was used to calculate SLC and multi-look intensity images in radar range-Doppler coordinates from the raw data. Next, GAMMA InSAR uses these files to compute displacements between pairs of SAR scenes. The second image was first resampled into the geometry of the first image in order to co-register the two SLCs based on orbit and terrain height data. Next, the orbit data were used to determine the offset between the two images, which is refined with a two-dimensional cross-correlation analysis. Range and azimuth displacements between the two images were then estimated with a cross-correlation optimization.

Subsequently, the displacements were converted from RADAR geometry to meters in ground range and from complex to real numbers. The ASTER GDEM was used to create a look-up table between the displacements and the DEM file, which was applied to add the georeferencing information to the centre of every matching window used to calculate the displacements. GeoTIFF files of the outputs were then created and the total displacement between the two images was computed from:

$$Total\ displacement = \sqrt{(range\ displacement^2) + (azimuth\ displacement^2)} \quad (2.2)$$

In order to convert the total displacement to metres per year, the values were divided by the total number of days between the two images to calculate the daily displacements, which was then multiplied by 365.25 to compute the annual displacements. This facilitates comparison between the velocities derived with GIV and the ones acquired from the NASA ITS_LIVE dataset, which are already standardized to annual values.

2.3.2.3 NASA ITS_LIVE

All surface velocities since 1999 were acquired from NASA's Inter-mission Time Series of Land Ice Velocity and Elevation (ITS_LIVE; https://nsidc.org/apps/itslive/) dataset, which provides a near-global record of glacier velocities at high temporal resolution from optical satellite imagery (Gardner et al., 2019). The data were generated using the autonomous Repeat Image Feature Tracking (auto-RIFT v0.1) processing scheme produced by the NASA Jet Propulsion Laboratory (Gardner et al., 2018), with imagery mainly from Landsat 4, 5, 7, and 8. The velocity data have a spatial resolution of either 120 m or 240 m and can be gathered from the data portal either as scene-pair velocities with a time separation ranging from 6 to 546 days, or as monthly or annual velocity mosaics created from the synthesis of all scene-pair velocities.

The regional composite of annual mean surface velocities for Arctic Canada North for 2000–2018 was downloaded and subsetted to Axel Heiberg Island in QGIS 3.6. Some of the velocity mosaics from 2000 to 2008 provide no or partial coverage of Iceberg Glacier, thus scene-pair velocities were downloaded to fill in the gaps during that period. Additionally, scene-pair velocities provided coverage for 1991, 1999, 2019, 2020, and 2021. For years with many available image-pair velocities (i.e., >150) for the area of interest, the data products were filtered by setting a minimum time separation between the two images (i.e., >60 days) and/or a minimum coverage (i.e., the percentage of possible glacier pixels that have reported velocities) of between 10 and 90%, depending on the amount of data available for a given year. After gathering all velocity products for a given year, each velocity file was inspected to keep the scene-pair velocities with the highest coverage over Iceberg Glacier and with the smallest apparent errors (i.e., the lowest velocities over bedrock; Table 2.2). GeoTIFF files of the velocity errors for the annual mosaics for the period 2000–2018 were downloaded. All GeoTIFF files (i.e., velocities and errors) were projected to NAD 1983 UTM Zone 15N.

Uncertainty estimates for all of the scene-pair data from GIV, GAMMA, and ITS_LIVE were determined by computing the median and SD velocity over non-glacierised terrain surrounding Iceberg Glacier (Table 2.2; Appendix A). The median value was used instead of the mean to provide a better measure of central tendency of the uncertainties due to the presence of outliers in the data. For the velocity mosaics, the median yearly error value over Iceberg Glacier from the ITS_LIVE GeoTIFF annual error files (i.e., v_err) was calculated and used to estimate uncertainties (see http://its-live-data.jpl.nasa.gov.s3.amazonaws.com/documentation/ITS_LIVE-Regional-Glacier-and-Ice-Sheet-Surface-Velocities.pdf for an explanation of how errors were quantified for the annual mosaics).

Table 2.2. Landsat (L) and ERS scenes used to derive ice surface velocities with associated uncertainty quantified by the velocities captured over non-glacierised terrain.

Satellite	First scene	Second scene	Uncertainty (m a^{-1}): median/SD
L1	28/08/1972	08/19/1974	15.4 ± 8.2
L1/L2	19/08/1974	07/25/1975	40.3 ± 23
L2	06/08//1975	09/04/1976	32.9 ± 28.6
L2	03/08/1976	29/07/1977	44.7 ± 24.4
L2	12/07/1977	04/07/1978	36.1 ± 27.9
L2/L3	03/09/1978	07/09/1979	37.8 ± 37.4
L2	07/09/1979	30/08/1980	67.9 ± 40.8
L2	30/08/1980	30/08/1981	34.4 ± 25.3
L2	19/07/1981	30/08/1981	387.9 ± 322.0
L5	22/06/1991	09/08/1991	67.0 ± 67.8
ERS-1	06/10/1991	18/10/1991	21.8 ± 21.6
ERS-1	06/02/1992	07/03/1992	23.8 ± 15.9
ERS-2	08/04/1997	13/05/1997	14.5 ± 18.2
L7	06/07/1999	22/07/1999	89 ± 100
L7	20/07/1999	20/06/2000	5.0 ± 4.5
L7	11/06/2000	14/06/2001	6.0 ± 5.0
L7	25/06/2001	12/06/2002	11.0 ± 7.1
L7	29/07/2005	16/07/2006	4.0 ± 5.6
L7	07/07/2006	08/06/2007	7.0 ± 7.7
L8	09/04/2019	11/04/2020	3.0 ± 3.8
L8	11/02/2020	14/05/2021	3.0 ± 4.0

2.3.3 Surface elevation

2.3.3.1. sPyMicMac

A pair of July 1977 KH-9 Hexagon declassified intelligence satellite photos (image ID: DZB1213-500054L001001 and DZB1213-500054L002001) and 18 historical air photographs (photos 098–115 from roll A16754) taken over Iceberg Glacier in July 1959 were used to create DEMs with sPyMicMac, a set of Python tools for processing historical spy satellite and aerial imagery (https://spymicmac.readthedocs.io). This enables glacier surface elevations and volume

changes to be computed for early periods (McNabb et al., 2020), as most global estimates of glacier volume changes are only available since the year 2000 (Zemp et al., 2016; Hugonnet et al., 2021).

Although the general workflow is virtually identical for both KH-9 and historical aerial photographs, which were processed separately, the pre-processing steps differ slightly. Pre-processing of the KH-9 data consisted of joining the two halves of both photographs together since KH-9 images are scanned into two parts (e.g., DZB1213-500054L001001_a and DZB1213-500054L001001_b) because of the large size of the film of ~9"x18", and resampling the two images to correct distortions in the film. The resampling is based on the location of the Reseau markers in KH-9 images, which sPyMicMac automatically finds and resamples to their expected location. The next step consisted of removing the Reseau markers from the KH-9 images and joining the two slightly overlapping image halves together. Since the KH-9 images were relatively low contrast, contrast enhancement was undertaken using one of sPyMicMac's functions which processes the images with a median filter to reduce noise and applies a linear contrast stretch as well as gamma adjustment.

As for the pre-processing of historical air photos, the same contrast enhancement was applied to each image, although no de-striping or de-noising, which can help remove artefacts occasionally found in aerial photos, was necessary. While this is done automatically when processing KH-9 images, some processing files, such as files containing information on the dimension of the images, the focal length of the camera used, and the location of the fiducial markers in the image geometry, had to be created. This information can typically be found in camera calibration reports, and example files of the necessary processing files can be downloaded from sPyMicMac's Read the Docs webpage

(https://spymicmac.readthedocs.io/en/v0.1.1/examples/index.html). Next, the images were resampled to a common geometry using the four fiducial markers found in the corners of the historical air photos, each of which had to be precisely located in all of the 12 images.

Once the KH-9 images and historical air photos were resampled, tie points were computed by matching all pairs of images (i.e., one pair for the KH-9 images and several for the air photos), and these were then used, along with a basic radial distortion model, to estimate the relative orientation of each image (McNabb et al., 2020). Thereafter, the relative (i.e., not georeferenced) orthoimages and DEM were generated using the orientation files from the previous step and a relative orthomosaic was created from the individual orthoimages. Before georeferencing the relative orthomosaic and DEM, control points were found and the absolute orientation was estimated and iteratively refined, which sPyMicMac does automatically using a number of files. These included a 2020 Sentinel-2 mosaic used as the reference orthoimage, the ASTER GDEM used as the reference DEM, image footprints from USGS for the KH-9 scenes or from NAPL for the 1959 air photos, and a modified version of the Randolph Glacier Inventory (RGI) 6.0 glacier outlines used as an exclusion mask to avoid searching for matches over glaciers or the ocean/sea ice. Finally, the orientation files and control points were used to generate the absolute (i.e., georeferenced) orthomosaic and DEM. For a more detailed explanation of each step, see https://spymicmac.readthedocs.io/en/v0.1.1/tutorials/index.html.

2.3.3.2. MMASTER

DEMs were generated for the years 2000–2021 from ASTER imagery using MicMac ASTER (MMASTER; Girod et al., 2017; Table 2.3). Since 1999, ASTER on board the Terra satellite has collected 15 m resolution stereo images, which have been used to produce the

ASTER GDEM (Global Digital Elevation Model) at 30 m grid spacing (https://asterweb.jpl.nasa.gov/gdem.asp). However, the dates of individual elevations in the ASTER GDEM are unknown, and noise is present in the satellite data in the form of "jitter" (i.e., uncorrected errors in the imagery geometry due to sensor motion), which can result in anomalies and artifacts (Girod et al., 2017).

The MMASTER software package enables the production of DEMs from ASTER stereo satellite imagery with reduced overall noise and fewer unmatched areas compared to NASA's standard AST14DMO product, with a horizontal resolution of 30 m or less, and a vertical uncertainty of 10 m (Girod et al., 2017). MMASTER computes Rational Polynomial Coefficient models from ASTER metadata, which identifies and corrects jitter-induced cross-track parallax errors to improve the quality of matching and applies a correction for along-track jitter when differences between DEMs are computed (Girod et al., 2017). 816 ASTER L1A scenes (i.e., reconstructed unprocessed instrument data) were downloaded from NASA's Earthdata Search portal (https://search.earthdata.nasa.gov) for the area of interest using a cloud filter to exclude scenes with a cloud cover greater than 80%. Subsequently, batch processing of the MMASTER workflow was conducted on the Cedar supercomputer from Compute Canada (https://docs.computecanada.ca/wiki/Cedar) to create 816 DEMs from the raw ASTER L1A products. The DEMs were then visually inspected to exclude those with large amounts of noise resulting from cloud cover or otherwise poor coverage of Iceberg Glacier and its tributaries. The DEMs provided relatively good temporal coverage over the period 2000–2021, although no good quality data were available over Iceberg Glacier for 2000, 2008, and 2015, while others years, such as 2010, 2011, 2020, and 2021 did not have complete coverage.

2.3.3.3 Co-registration and trend analysis

All DEMs created with sPyMicMac and MMASTER were iteratively co-registered using the dem-coregistration Python package (https://github.com/iamdonovan/dem-coregistration) created by Robert McNabb, which is based on the co-registration algorithm described by Nuth & Kääb (2011). Post-processing of the ASTER DEMs included spatial and temporal filtering of outliers from each DEM by excluding pixels that had a difference from the ASTER GDEM greater than a specified threshold value. Difference maps between each DEM from 2001 to 2021 and the ASTER GDEM were computed and visually inspected to determine an appropriate threshold to differentiate real elevation changes on the glacier surface from noise due to cloud cover or other biases for 5-year periods (i.e., 2001–2006, 2006–2011, 2011–2016, 2016–2021). Different threshold values were used for the terminus compared to the rest of the glacier since elevation changes were consistently greatest at the terminus region. Threshold elevation changes for the terminus area of Iceberg Glacier ranged from 70 to 100 m, while thresholds for the rest of the glacier were between 30 and 55 m. This spatial and temporal filtering of outliers was automated using models created with ModelBuilder in ArcGIS. The use of overlapping DEMs from within the same year was avoided to minimise the computation of false trends arising from vertical uncertainties, which are exacerbated when the time separation between two DEMs is short.

Finally, the make_stack.py Python script from the pygeotools Python package was used to compute the trend in elevation changes for Iceberg Glacier from the ASTER DEMs for the 5-year periods 2001–2006, 2006–2011, 2011–2016, 2016–2021, as well as for 2001-2011, 2011-2021, and 2001-2021. This script computes various statistics (e.g., min, max, mean, trend) using a raster time series object (i.e., a stack of input rasters) from which a linear regression is

calculated. When the temporal coverage of DEMs is sufficient, computing the trend in elevation changes between multiple DEMs using make_stack.py yields lower uncertainties than differencing just one DEM from another, which is why make_stack.py was used for 2001–2021.

For the 1959 and 1977 DEMs created with sPyMicMac, elevation changes were computed by calculating the difference between two DEMs using the Minus tool in ArcGIS, which subtracts the value of the second input raster from the value of the first input raster on a cell-by-cell basis. Elevation changes were determined between 27/07/1959 (air photos) and 13/07/1977 (KH-9), and between 13/07/1977 and an ASTER DEM mosaic from 26 May and 28 May 2003. The 2003 DEM was used instead of the one from 20 May 2001 to include surge termination, which occurred in 2003. This way, the 1977–2003 DEM differencing approximately coincides with the active phase of the surge. Elevation trends were then standardized to annual values by dividing the result by the number of years elapsed between the two DEMs.

To minimize noise from individual grid cells, plots of the results were made showing the average change in elevation across the glacier surface for each 10 m elevation contour based on the glacier's 2001–2021 mean elevation computed from all the available ASTER DEMs. Uncertainties in the trends and DEM differencing results were determined by calculating the median absolute value over stable (i.e., non-glacierised) terrain (Appendix A).

2.4 Results

2.4.1 Terminus position changes, surge initiation, and termination

Historical air photos, spy satellite imagery, and Landsat 1–3 scenes show that the terminus of Iceberg Glacier was retreating from 1950 to 1981. The glacier front underwent a ~1.9 km mean terminus-wide retreat in 22 years between 1959 and 1981 at a mean rate of -145.2

± 1 m a^{-1} for the period 1959–1966, -54 ± 7.5 m a^{-1} for 1966–1972, and -64 ± 9.4 m a^{-1} for 1972–1981 (Figure 2.2a; Table 2.3). This retreat was especially pronounced over the eastern side of the terminus, while the westernmost ~2 km of the terminus saw very little change. Subsequently, Iceberg experienced a pronounced terminus advance of ~5.3 km from 1981 to 1991, at a mean rate of 532.4 ± 6.4 m a^{-1} during those ten years (Figure 2.2b; Table 2.3). In addition, a Landsat 5 scene from 1984 with partial coverage of Iceberg Glacier's terminus shows that the eastern half of the terminus advanced by about 2.3 km between 1981 and 1984 at a mean rate of >750 ± 42.4 m a^{-1} (Figure 2.2b; Table 2.3). This indicates that Iceberg Glacier was likely surging in 1984. A further advance of ~1.2 km followed from 1991 to 2000, which occurred at a mean rate of 145 ± 2.7 m a^{-1} (Figure 2.2b; Table 2.3). The glacier reached its maximum observable surge extent in the winter of 1997 at a distance of ~7.6 km from its 1981 position, with parts of the terminus having advanced by more than 10 km.

The terminus positions from 1991 to 2000 were digitised from a combination of summer optical satellite imagery (1991, 1995, 1999, and 2000) and winter ERS-1 and ERS-2 SAR scenes (1992, 1993, 1994, 1997, and 1998). The winter ERS scenes show that as the glacier's front pushed forward, it frequently splayed out into the adjacent sea ice, forming a digitate terminus that later would break apart once the sea ice started retreating from Iceberg Bay during the following summer months. These seasonal fluctuations make it more challenging to determine the temporal evolution of the terminus extent during the active phase of the surge. However, it is clear that Iceberg Glacier reached its maximum position around 1996–1997 since the terminus was less extensive in the winter of 1995, 1998, and 1999.

In 2000–2010, which marks the transition from the active phase to the quiescent phase of the surge cycle, the terminus of Iceberg Glacier retreated by ~0.7 km at a mean rate of 70.6 ± 2.3

m a^{-1}. The ice front then started retreating at an accelerated pace of 175.5 ± 1.9 m a^{-1} from 2010 to 2021, equating to a total retreat of ~1.9 km over approximately the last decade (Figure 2.2c; Table 2.3). A large calving event occurred between 12 August 2014 and 1 September 2015, resulting in a terminus retreat of up to ~1 km (average of 432 m across the terminus width) and a loss of >2 km^2 of ice.

On average, Iceberg Glacier retreated by >2 km between 1950 and 1980, followed by a ~6.5 km advance from 1981 to 2002 during the active phase, and a >2.5 km retreat since the glacier became quiescent in 2003. These results are in line with observations made by Copland et al. (2003) and Van Wychen et al. (2016), who reported a terminus advance of ~5 km from 1959 to 1999 followed by a retreat of ~1.5–2.5 km from 2000 to 2014.

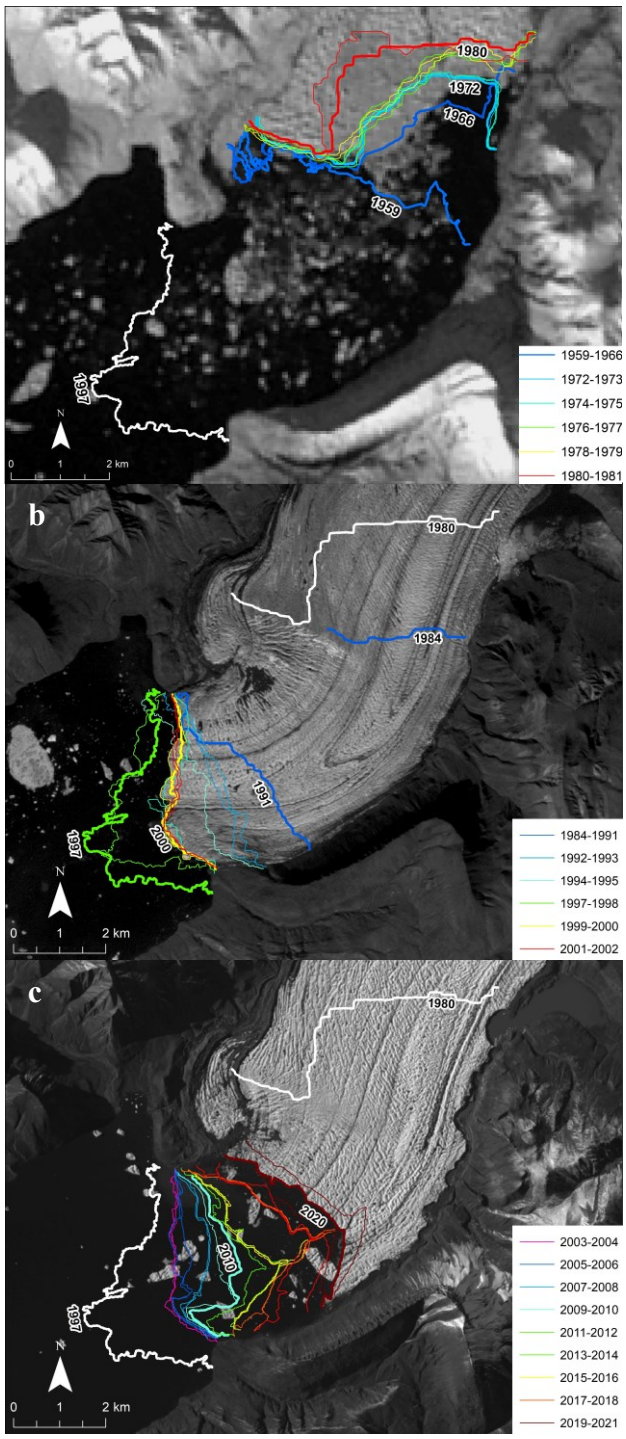

Figure 2.2. Terminus positions of Iceberg Glacier for: (a) 1959–1981 (pre-surge), (b) 1984–2002 (surge), and (c) 2003–2021 (post-surge). The colour palette ranges from blue (earliest) to red (latest) while certain years are annotated and their respective terminus lines are thicker to help with visual interpretation. The pre-surge (1980) and maximum surge (1997) terminus positions are included in each plot for reference. Base images: (a) Landsat 2, 30 August 1981, (b) Landsat 7, 25 July 1999, (c) Landsat 8, 7 August 2020.

High-resolution historical aerial photographs from 1950 and 1959 reveal that Iceberg Glacier's surface was heavily potholed (Figure 2.3a). Spy satellite imagery from 1966 and 1977 also show potholing, although it was less extensive than in the 1950s. This observation, along with the glacier's retreating terminus during that period suggest that the glacier was in its quiescent phase of the surge cycle and had previously surged. Distorted medial moraines located at the intersection of the lower two tributaries and the glacier trunk (Figure 2.3b) from 1959 to 1981 indicate that they are subject to irregular ice flow and could have surged in the past.

Conversely, the glacier had a heavily crevassed surface (Figure 2.3e), large looped moraines (Figure 2.3f), and clearly visible shear margins from SAR scenes in the 1990s (Figure 2.3d). Moreover, a photograph taken by Miles Ecclestone, a field technician, during a flight from Expedition Fiord in 1989 shows that Iceberg Glacier had a highly broken up surface, indicating that the glacier was flowing at a very rapid rate and that it had started surging before 1989. Ice mélange was present at the glacier front in August–September 1980 and throughout 1981. This could be indicative of increased ice velocities and calving rates at the terminus of Iceberg Glacier in the early 1980s.

Meanwhile, the surge termination was inferred from optical and SAR imagery to have occurred in the early 2000s on account of the terminus retreat that started after 1997, and the progressive decrease in the extent of crevassing and shear margins. Ice surface velocities can help to further constrain the timing of surge initiation and termination, which will be examined in the following section.

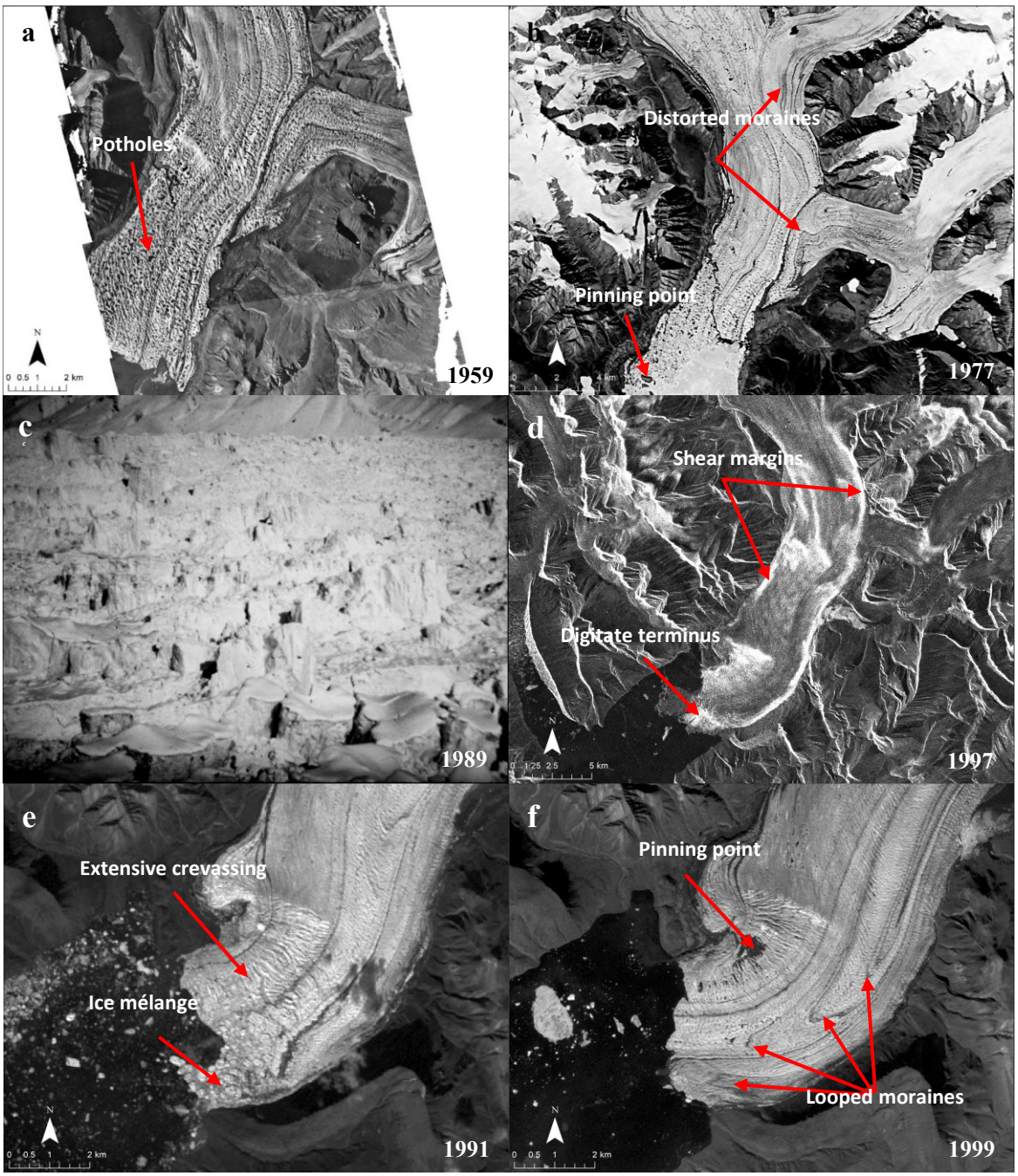

Figure 2.3. Iceberg Glacier surface features indicative of surging. (a) Clearly visible extensive potholing on the glacier surface during quiescence. (b) 13 July 1977 KH-9 image showing distorted medial moraines at the junction between the two lower tributaries and the trunk and a pinning point in front of the terminus. (c) Low-altitude oblique aerial photograph taken by Miles Ecclestone in 1989 showing the glacier's highly broken up surface. (d) Shear margins and Iceberg's terminus splaying out onto the sea ice forming a digitate terminus observable from an 8 April 1997 ERS-1 SAR scene. (e) Landsat 5 image 9 August 1991 displaying extensive crevassing near the terminus and ice mélange at the ice front. (f) Medial moraines from Iceberg Glacier's tributaries that were displaced far downstream by fast moving ice creating looped moraines (25 July 1999, Landsat 7). The same pinning point as in (b) is also visible.

Table 2.3. Mean total changes and mean change rates of Iceberg Glacier's terminus position for different periods from 1959 to 2021. Negative values indicate a terminus retreat while positive values indicate a terminus advance.

Time period	Mean total change (m)	Mean change rate (m a^{-1})	Uncertainty (m a^{-1})
1959–1966	-1016.7	-145.2	1.0
1966–1972	-324.2	-54.0	7.5
1972–1981	-576.3	-64.0	9.4
1981–1991	+5324.4	+532.4	6.4
1991–2000	+1160.3	+145.0	2.7
2000–2010	-705.5	-70.6	2.3
2010–2021	-1930.2	-175.5	1.9

2.4.2 Velocity patterns

The surface velocities of Iceberg Glacier varied significantly throughout the study period as the glacier underwent a surge cycle. The mean centreline velocity of Iceberg's trunk from 1972 to 1980 derived from Landsat 1–3 imagery was ~89 m a^{-1}. Velocities reached >100 m a^{-1} from 14 to 23 km up-glacier from the 1997 terminus position, which roughly equates to the area between the junctions of the two lowermost tributaries with the trunk. Conversely, velocities near the terminus were typically below 50 m a^{-1}, but appear to have generally increased throughout the 1970s, reaching values of >100 m a^{-1} in 1979–1980. Although coverage of single image-pair velocities are often fairly poor, velocities downstream of 26 km from the 1997 terminus seem to have increased throughout this period (Figure 2.4). Iceberg Glacier flowed at a median rate of 27 m a^{-1} (SD of 30 m a^{-1}) over the entire trunk width downstream of 26 km, with a maximum velocity of 134 m a^{-1} in 1972–1974 (Figure 2.4). Over 1979–1980, a median velocity of 95 m a^{-1} (SD of 41 m a^{-1}) and a maximum velocity of 264 m a^{-1} was derived (Figure 2.4), with the majority of the acceleration occurring within the terminus area.

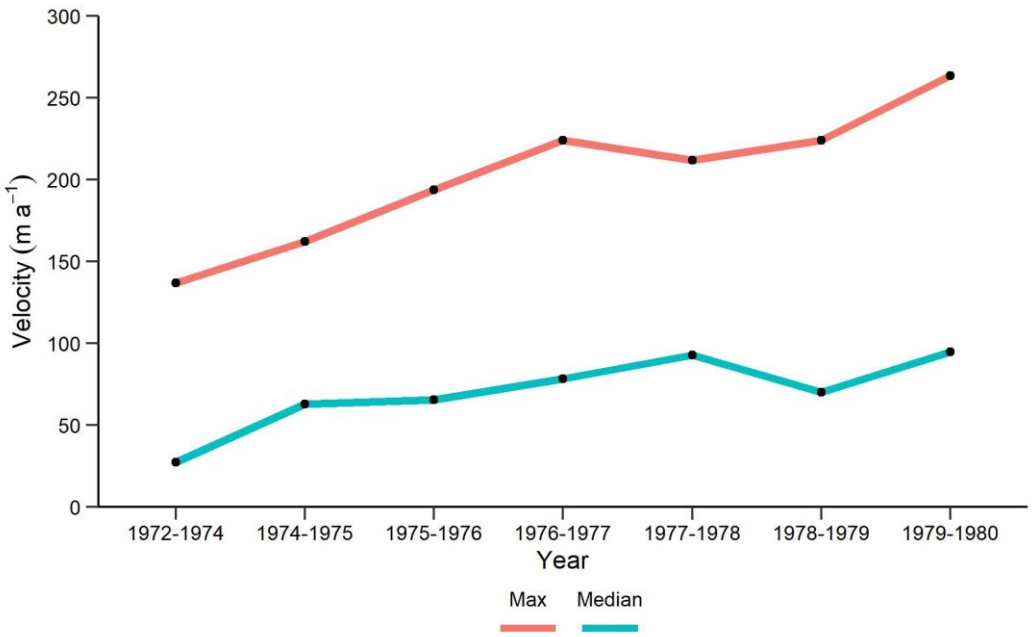

Figure 2.4. Evolution of Iceberg Glacier's median and maximum surface velocities below 26 km from the 1997 terminus for 1972–1980. Velocities were derived from feature-tracking on Landsat 1–3 imagery.

Iceberg Glacier's flow rate within its terminus region underwent a drastic increase in summer 1981, with velocities reaching up to ~1500 m a^{-1} (Figure 2.5). This represents a more than 50-fold increase in ice surface velocities in parts of the terminus region compared to the 1972–1980 average. The velocities derived for 19 July 1981 to 30 August 1981 have large uncertainties, but manual tracking of features between these images reveals velocities at the terminus region reaching >1700 m a^{-1}. This acceleration was accompanied by a ~100–400 m advance of the easternmost ~1.5 km of the terminus, where velocities attained >1000 m a^{-1}. The marked increase in surface velocities observed in summer 1981, along with the appearance of ice mélange in front of the terminus in 1980, suggests that a surge likely started in the early 1980s.

Although velocities are unknown from 1982 to 1990 due to a lack of available imagery, results show particularly high velocities in 1991, indicating that Iceberg Glacier was certainly still surging at that time. The average centreline ice flow derived from June–July 1991 NASA ITS_LIVE image-pair velocities was 910 m a^{-1}, with a maximum centreline value of ~1800 m a^{-1}

(Figure 2.5). Velocities of >2000 m a^{-1} were recorded over the northern half of the terminus with a highest value of 2320 m a^{-1}. Ice flow along the centreline in summer 1991 remained above 1000 m a^{-1} within 24 km from the 1997 terminus position, constituting the year with the highest velocities on record. Meanwhile, average centreline velocities during fall 1991 quantified from a pair of ERS-1 scenes dropped to 690.3 m a^{-1}, peaking at >1500 m a^{-1} at the terminus (Figure 2.5). In the subsequent year, centreline velocities remained below 1000 m a^{-1} with a mean of 490.2 m a^{-1}, which then further decreased to a mean velocity of 348.4 m a^{-1} in 1997 when 75% of the glacier's velocity profile remained below 500 m a^{-1} (Figure 2.5).

The 1999 velocities were ~57% higher than in 1997, with a mean centreline velocity of 546.2 m a^{-1} and ice flow consistently greater than 500 m a^{-1} up to 26 km from the 1997 terminus position (Figure 2.5). It is unclear whether this constitutes an actual speedup or whether the differences in velocities could be explained by the large median uncertainties of 89 m a^{-1} for 1991 and/or by the fact that velocities in 1997 were derived from spring (April–May) scenes, while the 1999 velocities were extracted from summer (July) images. During the surge, the distorted medial moraines found at the junction between the two lowermost tributaries and the trunk (Figure 2.3b) were pushed toward the glacier margin by up to ~1 km due the main trunk's rapid flow. Some medial moraines from these two tributaries were also displaced by the fast moving ice and brought several kilometers downstream to form looped moraines that are visible in optical imagery from the 1990s and early 2000s (Figure 2.3f).

Thereafter, velocities showed a steady decrease from the beginning of the 21st century until present. The most drastic deceleration occurred between 1999 and 2000, when velocities dropped by a factor of three to an average of 189.5 m a^{-1} across the centreline (Figure 2.5). This slowdown is in accordance with results extracted from RADARSAT-1 speckle tracking by Short

& Gray (2005), which showed that the glacier's flow rate had decreased to 75–130 m a^{-1} by fall 2000. The majority of the remaining slowdown during the transition to the quiescent phase occurred between 2000 and 2003. Centreline velocities dropped to an average of 132.9 m a^{-1} in 2000–2001, followed by another drop to 94 m a^{-1} in 2001–2002 and finally to 17 m a^{-1} in 2003 at a distance of approximately 7.5–15 km from the 1997 terminus (Figure 2.6). By 2004, the average summer velocity was 39.1 m a^{-1} across the centreline while the terminus region was entirely stagnant (Figure 2.6). This is also consistent with findings by Short & Gray (2005), which show that the ice flowed at a rate of <25 m a^{-1} in mid-winter 2004. This suggests that surge termination likely occurred in 2003.

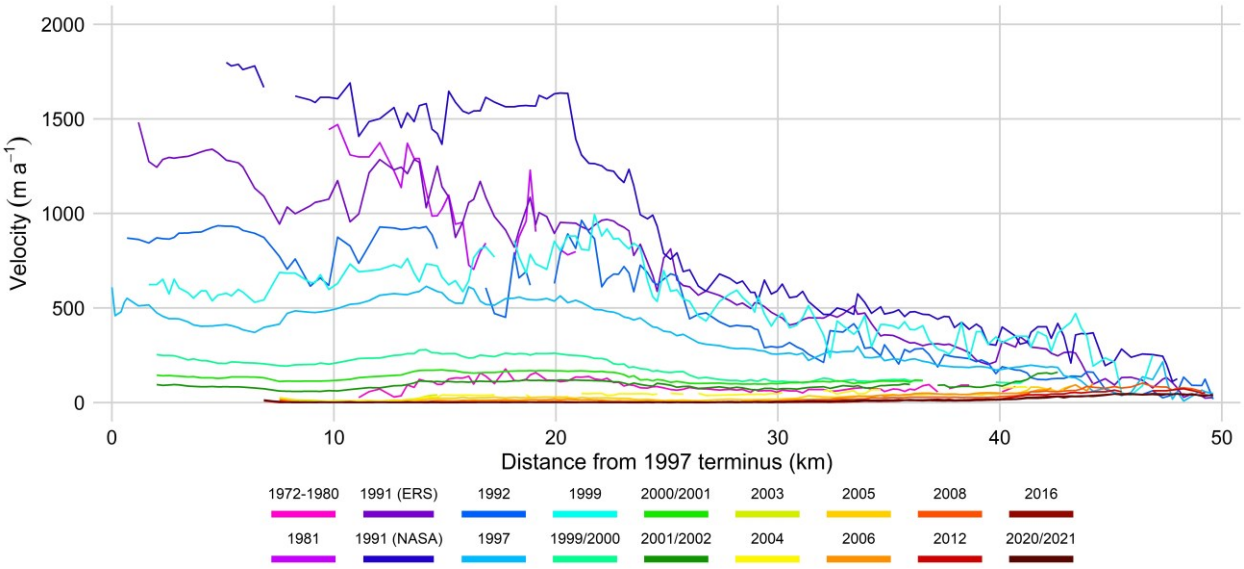

Figure 2.5. Iceberg Glacier centreline (Figure 2.1) surface velocities from 1972 to 2021, based on distance from the terminus at the glacier's maximum surge extent in 1997. Velocities for the period 1972–1980 represent the mean of several annually separated velocity scenes derived from feature-tracking. The velocity profiles prior to 1999 were extracted from Landsat 1–3, ERS-1/2, and NASA ITS_LIVE scene pairs, while all profiles since 1999 were derived from NASA ITS_LIVE (Gardner et al., 2019) scene pairs or annual mosaics.

Contrary to the velocity profiles during the active phase of the surge where velocities were highest in the lower half of the glacier and started decreasing upstream of ~20–25 km from

Iceberg Glacier's maximum surge terminus position (Figure 2.5), velocities in the post-surge quiescent period were highest above 30 km from the terminus (Figure 2.6). By 2009, velocities remained below 25 m a^{-1} across the entire glacier trunk, confirming the findings of Van Wychen et al. (2016, 2021) that the entire trunk had become essentially stagnant by ~2010. Velocities continued to decrease to values of <10 m a^{-1} over most of the glacier trunk within the last decade, and ice motion has been < 50 m a^{-1} along the entire velocity profile since 2016 (Figure 2.6).Since the end of the surge in ~2003, the average centreline velocities of Iceberg Glacier have decreased from 39.1 m a^{-1} in 2004 to 11.5 m a^{-1} in 2020–2021 (Figure 2.6).

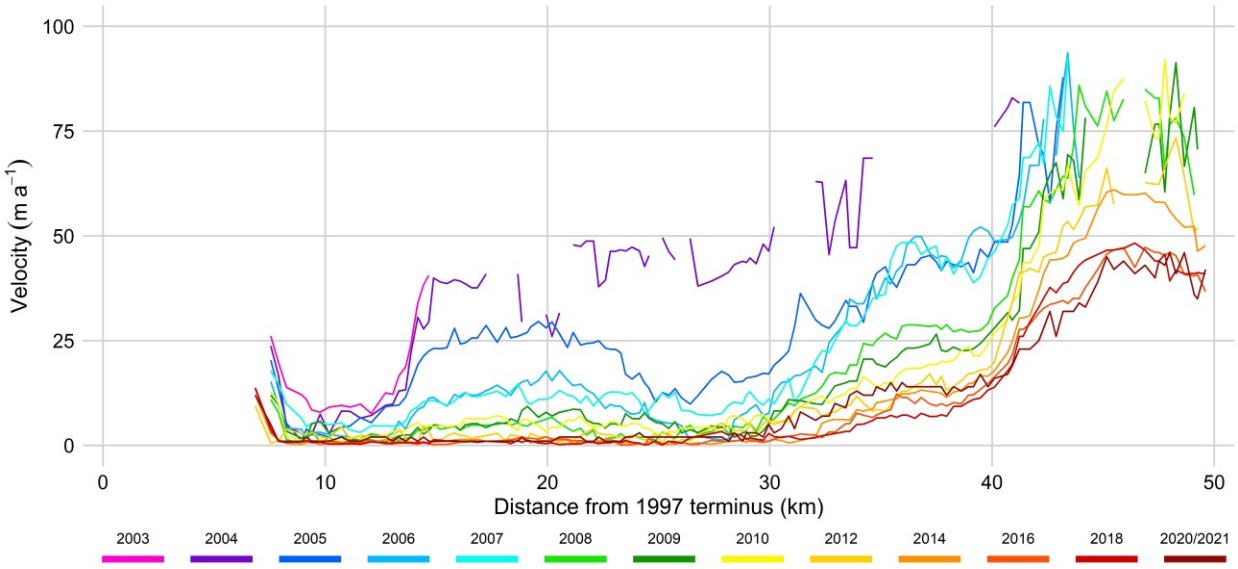

Figure 2.6. Iceberg Glacier centreline (Figure 2.1) surface velocities from 2003 to 2021 showing the start of the quiescent phase of the surge cycle. All velocity profiles come from the NASA ITS_LIVE dataset. Distance from the terminus is based on the glacier's maximum surge extent in 1997. Note difference in velocity scale from Figure 2.5.

2.4.3 Elevation changes

While large changes in terminus position and notable variations in glacier velocities are evident manifestations of surging behaviour, patterns in ice surface elevation changes can also be indicators of dynamic instabilities. From 27 July 1959 to 13 July 1977, the glacier experienced

thickening over most of the main trunk and its upper tributary, while parts of the other tributaries and the trunks' lowermost ~3–4 km thinned. Thickening was especially pronounced in the upper region of Iceberg's trunk with typical values ranging from ~4-6 ± 1.3 m a^{-1} and peaking at >7 ± 1.3 m a^{-1} (Figure 2.7a), indicating that parts of the glacier's upper region gained more than 100 ± 24.1 m of ice. Thinning rates reached approximately -7 ± 1.3 m a^{-1} on the eastern side of the terminus, but mainly remained below -3 ± 1.3 m a^{-1} (Figure 2.7a).

During the active phase, opposite elevation change trends were observed, with differencing of the 13 July 1977 KH-9 DEM and 26 May 2003 ASTER DEM showing ice thickness gains in the lower part of the glacier and losses in the upper part (Figure 2.7b; Figure 2.8). This period roughly coincides with the glacier's active phase that lasted from approximately 1981 to 2003. Below 16 km from the 1997 terminus position, the glacier thickened at an average rate of ~1.7 ± 1 m a^{-1} across the glacier's 10 m elevation bands and experienced the most pronounced thickening of >3 ± 1 m a^{-1} at 7–12 km (Figure 2.8), consisting of up to >80 ± 16.8 m in elevation gains over the 26-year period. The highest single-cell value of ~7 ± 1 m a^{-1} was recorded on the western side of the ice front (Figure 2.8). The remainder of the main trunk and upper tributary's surface at ~16–60 km from the 1997 terminus position lost, on average, -2 ± 1 m a^{-1} of ice across the glacier's 10 m hypsometric bands (Figure 2.8).

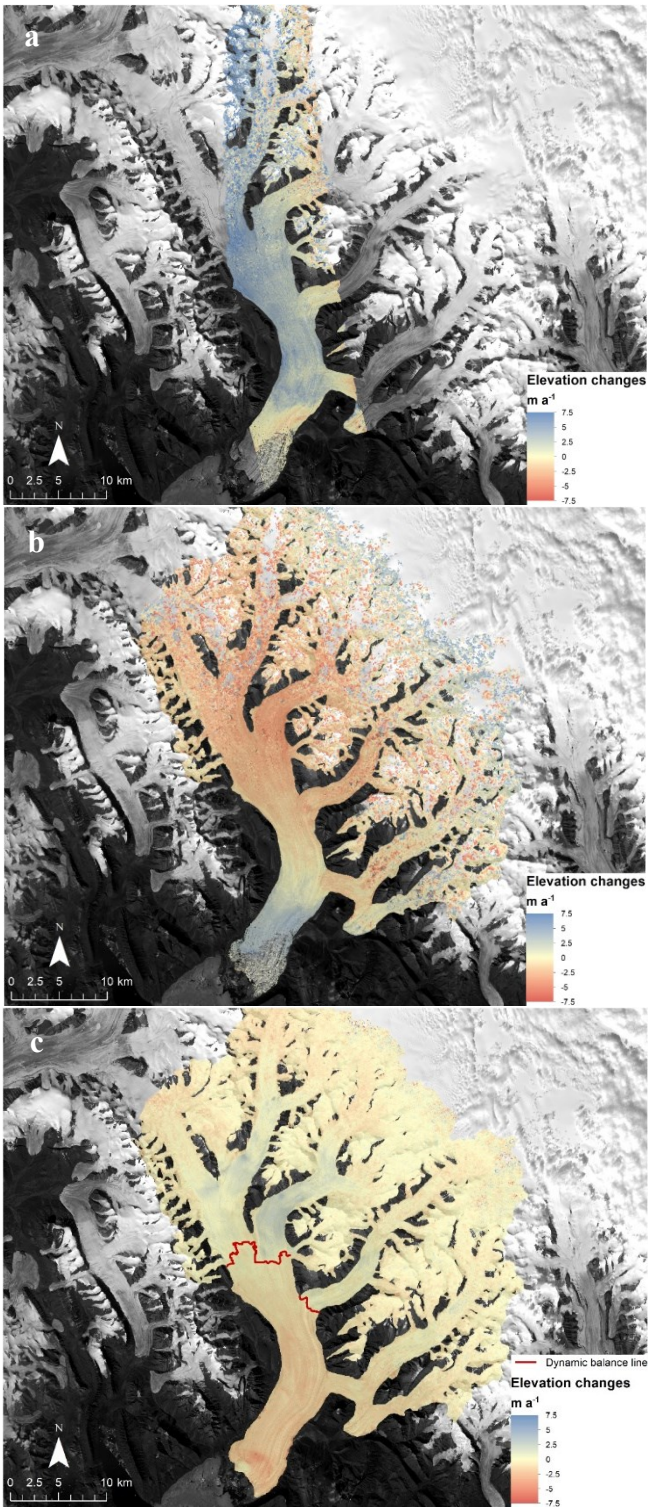

Figure 2.7. Surface elevation change trends (m a^{-1}) for Iceberg Glacier and its tributaries for the periods (a) 1959–1977, (b) 1977–2003, and (c) 2003–2021. Maps (a) and (c) represent elevation changes when the glacier was quiescent, while (b) roughly coincides with the timing of the glacier's active phase. The glacier's dynamic balance line is shown as a red line in (c). Base image: Landsat 8 composite image.

After 2003, the elevation change patterns reversed once again, reflecting the accumulation of mass over Iceberg's upper area. The gains in surface elevation occurred between approximately 32 and 49 km from the 1997 terminus position at a mean rate of ~0.6 ± 0.4 m a^{-1} along the glacier's 10 m hypsometric bands (Figure 2.8), and at a maximum single-cell rate of ~3 ± 0.4 m a^{-1} at ~42.5 km (Figure 2.7c). Meanwhile, the elevation bands downstream of ~32 km from the 1997 position lost mass at an average rate of -1.1 ± 0.4 m a^{-1} across the glacier's 10 m elevation bands (Figure 2.8), and the terminus region encountered the most substantial thinning, reaching mean single-cell rates over the entire 2003–2021 period as high as nearly -5 ± 0.4 m a^{-1} (Figure 2.7c) at ~8 km from the 1997 terminus. These patterns persisted throughout the current quiescent period, although the magnitude of the elevation changes appears to have decreased since 2003, and the patterns were less apparent in 2015–2021 in comparison to the previous twelve years.

The 2003–2021 trends computed from the high temporal resolution ASTER data were used to outline the dynamic balance line over Iceberg Glacier trunk, the location that separates the reservoir and receiving zones. This is located between approximately 30 and 33 km from the 1997 terminus position across the main trunk or at ~400 m a.s.l. (Figure 2.7c; Figure 2.8).

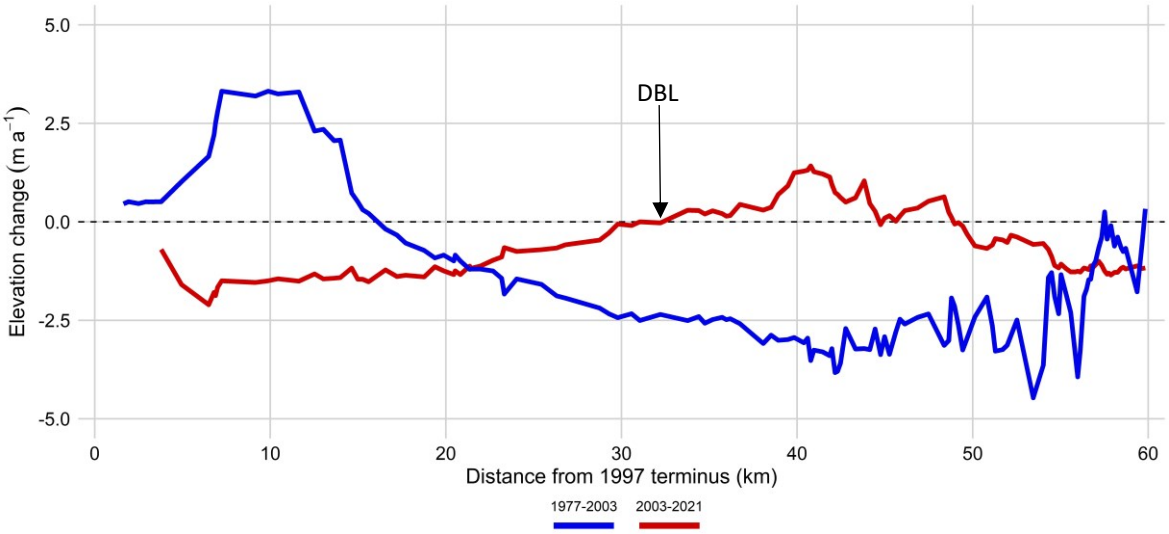

Figure 2.8. Mean glacier surface elevation change trends (m a^{-1}) for Iceberg Glacier in each 10 m elevation band for the periods 1977–2003 (active phase; blue) and 2003–2021 (quiescent phase; red). The distance from the terminus is based on Iceberg's maximum surge extent in 1997. DBL: dynamic balance line.

2.5 Discussion

An abrupt terminus advance, an increase in surface velocities, formation of new crevasses and/or surface elevation changes are all indicators of a possible surge initiation (Meier & Post, 1969; Raymond, 1987; Sund et al., 2009; Kochtitzky et al., 2019). Therefore, the marked increase in ice flow in 1981, the >7 km terminus advance that occurred between 1981 and 1997, as well as the crevasses, shear margins, and looped moraines visible on the glacier in the 1990s strongly suggests that a surge occurred with a likely initiation in the early 1980s. Surge termination occurred in 2003 when the average surface velocity over the glacier's lowermost ~7.5 km dropped to below 20 m a^{-1}.

2.5.1 Mass redistribution

As shown in the results, Iceberg Glacier exhibited a surface evolution marked by a net movement of mass down-glacier during the active phase of the surge with high velocities,

followed by an accumulation of mass over the upper part of the glacier during quiescence and a period of low velocities. The location of the dynamic balance line during the current quiescent period (Figure 2.7c) suggests that glacier ice will be drawn down from upstream areas during the next surge. Elevation changes for 1959–1977 during the previous quiescent phase suggest that the dynamic balance line would have been located much lower on the glacier during that period, although it is not possible to say whether this reflects a long term up-glacier migration of the dynamic balance line related to changes in surface mass balance (SMB), or higher errors of the 1959–1977 trends stemming from the differencing of two older DEMs, or some other factor.

To assess the relative importance of glacier dynamics versus SMB in accounting for the surface elevation changes observed over Iceberg Glacier, SMB data from Noël et al. (2018) were used for the periods 1958–1995 and 1996–2015, derived with the regional climate model RACMO2.3 (https://doi.pangaea.de/10.1594/PANGAEA.881315). SMB is defined as the difference between the processes adding mass to a glacier surface (e.g., precipitation, drifting snow) and those removing mass (e.g., melt, runoff, sublimation), and in this study were determined for every 50 m elevation band across Iceberg Glacier's trunk and upper tributary (Appendix A). The geodetic mass balance data were downsampled to 1 km to match the resolution of the SMB data, and the dynamic balance was computed by subtracting the SMB from the geodetic mass balance. Volume changes per 50 m elevation band were then calculated by multiplying the median elevation change (i.e., geodetic mass balance) of each band by the band's area. The SMB data were converted from water equivalent to ice equivalent values using a density of 850 ± 60 kg m^{-3}, following the recommendations of Huss (2013). The median SMB values over each elevation band from 1958 to 1995 were used for 1977–2003 (active phase),

while the median 1996–2015 values over each elevation band were used for 2003–2021 (quiescent phase).

The SMB data showed negative values up to elevations of 600–650 m (~43 km from the 1997 terminus) and an average ice loss of -1.0 ± 0.2 m a^{-1} across the entire glacier surface for 1958–1995. SMB values from 0–400 m a.s.l. for that period show a negative mass balance of around -2 ± 0.2 m a^{-1}, which reduced the amplitude and upstream extent of positive geodetic mass balance changes during the surge; Iceberg Glacier gained mass geodetically up to an elevation of 150–250 m a.s.l. (<20 km from the 1997 terminus) compared to 350–400 m a.sl. (>25 km from the 1997 terminus) dynamically (Figure 2.9a). Positive elevation changes peaked over the 50–100 m elevation band at values of 3.3 ± 1.0 m a^{-1} (5.1 ± 1.0 m a^{-1} dynamically), equivalent to a volume gain of 0.07 ± 0.001 km^3 a^{-1} (Figure 2.9a). Conversely, the glacier experienced the greatest rate of thinning of -5.2 ± 1.0 m a^{-1} at an elevation of 600–650 m, but saw the greatest volume loss of -0.06 ± 0.001 km^3 a^{-1} over the 350–400 m elevation band due to its largest area of 26.4 km^2.

The 1996–2015 SMB data reveal more negative mass balance conditions over Iceberg Glacier than in 1958–1995, with an average value of -1.4 ± 0.2 m a^{-1} over the main trunk and the upper tributary (Appendix A), and an up-glacier extension of the SMB equilibrium line altitude from 600–650 m a.s.l. (~43 km from the 1997 terminus) in 1958–1995 to 950–1000 m (~54 km from the 1997 terminus) in 1996–2015. As before, geodetic mass balance changes were generally more negative due to the inclusion of SMB, and the dynamic mass balance suggests that the glacier gained mass at an average rate of 1.0 ± 0.4 m a^{-1} up to an elevation of 950–1000 m a.s.l. (Figure 2.9b).

Mass loss during quiescence does not necessarily reflect the climatic mass balance of surge-type glaciers because the ablation area can be dynamically refilled from an area above the reservoir zone immediately after a surge, causing it to gain mass (Gardelle et al., 2013; Kochtitzky et al., 2019). In the case of Iceberg Glacier, mass being added to the trunk from the upper parts of tributaries, which have maintained a higher flow rate than the trunk during quiescence, could perhaps explain some of the observed dynamic thickening. Positive geodetic mass balance and volume changes both peaked around an elevation of 500–600 m a.s.l. at values of 1.6 ± 0.4 m a^{-1} and 0.007 ± 0.0004 km^3 a^{-1} (Figure 2.9b). Higher elevations (>800 m) continued to thin, possibly due to a continuing drawdown of mass driven by the relatively high velocities that were sustained over the upper regions of Iceberg's tributaries throughout the quiescent phase. In fact, Iceberg Glacier's upper three tributaries appear to play a key role in refilling the reservoir zone during quiescence owing to their relatively high flow rates and, consequently, high rates of mass transfer.

Summing of the volume changes over each elevation band for the 1977–2003 active phase indicates that a total geodetic mass gain of 4.3 ± 0.1 km^3 of ice occurred over the lower 200 m elevation band of Iceberg Glacier, compared to a total mass loss of 8.0 ± 0.4 km^3 over the rest of the surface, equivalent to a glacier-wide mean annual mass balance of -0.14 ± 0.02 km^3 a^{-1}. During the quiescent phase to date (2003–2021), the glacier has gained a total of 0.5 ± 0.1 km^3 of ice from 400–800 m elevation and lost a total of 2.9 ± 0.1 km^3 of ice in the receiving zone below 400 m elevation, equivalent to a mean annual mass balance of -0.15 ± 0.01 km^3 a^{-1}. Previous findings suggest that the movement of large quantities of mass to lower, warmer elevation during a surge can result in a strongly negative surface mass balance (Aðalgeirsdóttir et al., 2005; Kochtitzky et al., 2019), although the similarity in mean annual geodetic mass balance

between the active and quiescent phases suggests that Iceberg is dominated by long-term negative mass balance conditions, irrespective of surge phase.

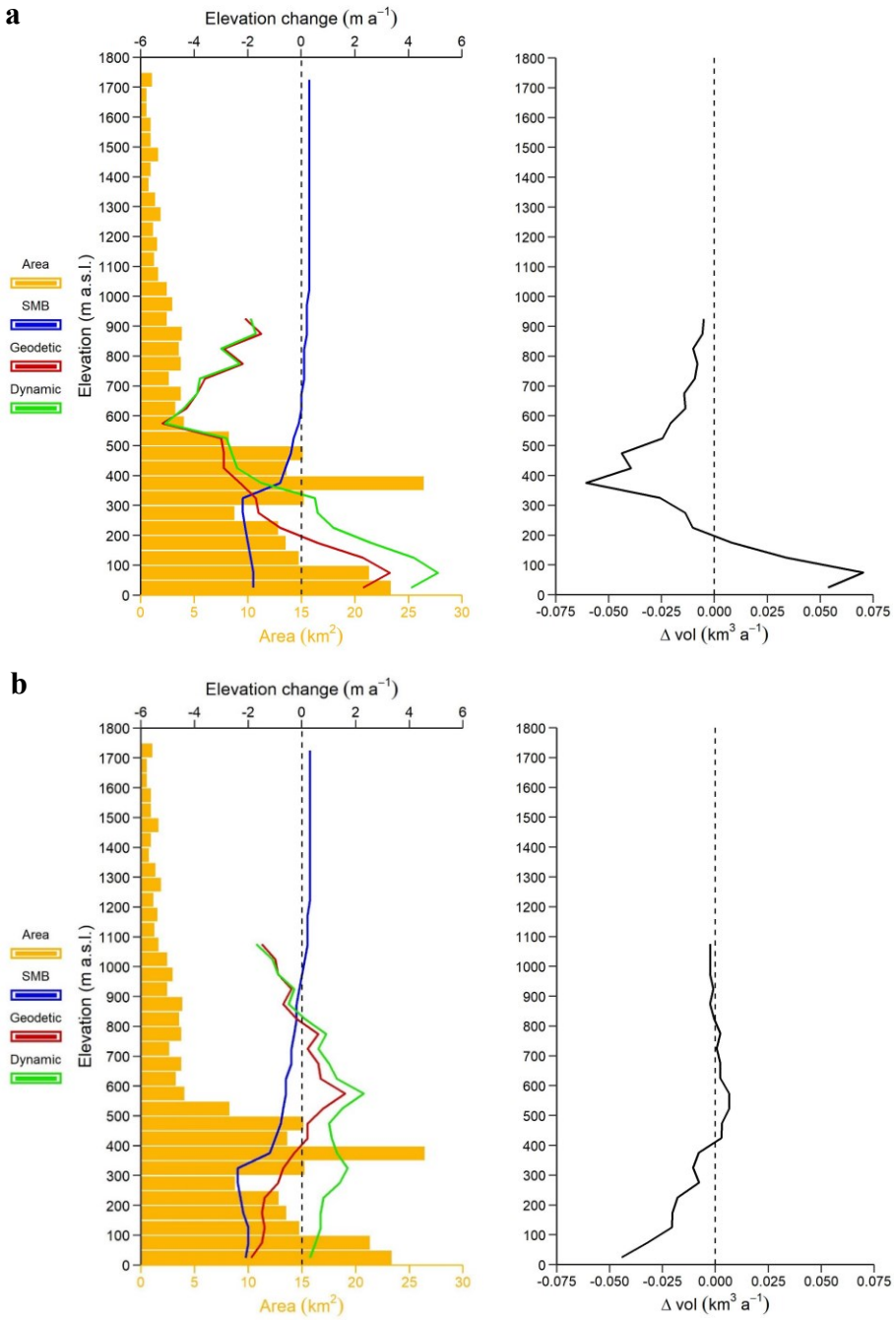

Figure 2.9. Iceberg Glacier median ice surface elevation change (geodetic mass balance), surface mass balance (SMB) and dynamic balance for each elevation band (left), and the median ice volume loss per elevation band (right), during: (a) the active phase (1977-2003), and (b) the quiescent phase (2003–2021). Glacier area in each 50 m elevation band (hypsometry) derived from 2001–2021 mean.

2.5.2 Length of the active phase and surge mechanisms

Surge initiation is inferred to have occurred in 1980 or 1981 based on the formation of ice mélange, a marked increase in surface velocities in summer 1981, and the significant terminus advance that ensued. The surge likely terminated in 2003 as velocities dropped to an average velocity of 17 m a^{-1} over the glacier's lowermost 7.5 km, although velocities continued to decrease over the entire glacier during the following >10 years (Figure 2.6). Consequently, it is likely that Iceberg Glacier surged for a total of ~22 years.

Previous studies on glaciers located in Svalbard and parts of Greenland have shown that surge initiation and termination can occur over several years (Mouginot et al., 2018), but that surge initiation can happen much more rapidly than surge termination (Murray et al., 2003), which seems to be the case for Iceberg Glacier. However, Iceberg Glacier was flowing at a much faster rate in 1972–1980 than during its current quiescent period, which raises the question of whether the glacier started accelerating prior to the 1970s. In fact, Iceberg was flowing at virtually the same average rate from 1972 to 1980 as during the end of the active phase in 2001–2002, and following a similar pattern, with both years having average centreline velocities of ~90 m a^{-1} (Figure 2.5). Additionally, our velocity results show a gradual increase in flow rates from 1972 to 1980 that, despite the poor spatial coverage of image-pair velocities derived from Landsat 1–3 images, appear to have resulted in more than a tripling of median velocities within 26 km from the 1997 terminus (Figure 2.4), particularly within the terminus region. Nevertheless, the glacier did not have any surface features indicative of surging throughout the 1970s, such as new crevasses, indicating that the glacier was likely not actively surging during that period. Instead, it seems that Iceberg's velocities underwent a long build up before the surge-triggering event that occurred in the early 1980s. The glacier's main tributaries, and

particularly the lowermost two tributaries, were flowing at much higher rates in 1972–1980 near their junction with the trunk than they presently are, with velocities reaching up to ~200 m a^{-1}. It has been shown that ice motion generally increases downstream of the junction between a glacier tributary and trunk (e.g., Gudmundsson, 1999), which seems to have occurred for Iceberg's lower two tributaries for 1972–1980, where average centreline velocities of >100 m a^{-1} were found between 14 and 23 km from the 1997 terminus. Therefore, the higher velocities during the 1970s in comparison to the current quiescent phase could be at least partly related to tributary dynamics.

The causes of glacier surging have been generally separated into two categories based on basal processes, with surge initiation either driven by a build-up of water pressure at the glacier bed due to the collapse of subglacial channels as ice overburden pressure increases during quiescence (Alaska-type surges; Kamb et al., 1985), or by a switch from cold to temperate basal conditions due to an increase in ice thickness during quiescence (Svalbard-type surges; Clarke, 1976; Murray et al., 2003). Hydrologically-regulated Alaska-type surges occur in regions with relatively temperate climates such as Alaska and Yukon, have shorter surge cycles and typically higher velocities than thermally-regulated Svalbard-type surges that are generally found in colder, drier climates, such as Svalbard and the Canadian Arctic (Murray et al., 2003). For example, surge-type glaciers in Svalbard experience surge cycles of 50–500 years and active phases of 3–10 years (Dowdeswell et al., 1991), while Donjek Glacier located in the St Elias Mountains, Yukon, has a significantly shorter ~12 year surge recurrence interval and a ~2 year active phase (Kochtitzky et al., 2019). Alaska-type surges are also subject to a much shorter surge initiation and termination on the order of days to months (Murray et al., 2003; Kamb et al., 1985).

Iceberg Glacier, with its active phase of more than 20 years and slow surge termination, seem to best fit under the category of a thermally-regulated surge. Nevertheless, there is a wide range of observed surge behaviour that do not properly fit in one of the two proposed categories of surges, including combined thermo-hydrological triggers, making the distinction between the two suggested surge mechanisms unclear in certain instances (Dunse et al., 2015; Sevestre et al., 2018; Benn et al. 2019b; Haga et al., 2020).

2.5.3 Relation to enthalpy theory of surging

Benn et al. (2019a) proposed a general theory of surging that uses enthalpy as a universal unit through which ice flow instabilities can be studied and that unifies different surge mechanisms. Enthalpy quantifies the internal energy of a glacier system that is primarily a function of ice temperature and water content (Aschwaden et al., 2012; Benn et al., 2019a). Enthalpy is gained at the glacier bed through geothermal heating, frictional heating and the supply of melt water. Meanwhile, enthalpy losses occur through heat conduction from the bed to the glacier surface and drainage of meltwater (Benn et al., 2019a). When balances in both enthalpy and mass flux are not met, this prevents the glacier from remaining in a stable steady state by periodically increasing mass flux to evacuate the buildup of excess enthalpy at the glacier bed (Sevestre & Benn, 2015; Benn et al., 2019a).

In the CAA, where climate is cold and dry, low basal enthalpy production and efficient conductive heat losses from cold atmospheric temperatures typically does not favour surging (Sevestre & Benn, 2015). Small glaciers especially have a high probability of being able to evacuate basal enthalpy by conductive heat losses due to their low balance velocities and, therefore, low frictional heating (Sevestre & Benn, 2015). However, larger glaciers in such

environments are less likely to find a balance between enthalpy production and enthalpy losses because they tend to have higher balance velocities and, as a result, higher basal enthalpy production. Indeed, surge-type glaciers in the Canadian Arctic are the largest of any surge cluster worldwide, with an average area of 627 km^2 (Sevestre & Benn, 2015). In addition, larger glaciers tend to be thicker, which reduces the capability of the glacier to evacuate enthalpy by conductive heat losses to the atmosphere (Sevestre & Benn, 2015). Unlike some smaller glaciers, larger glaciers may also be unable to evacuate cumulative discharge via inefficient, distributed subglacial drainage systems, leading to increased basal water storage and velocity-strain heating feedbacks (Sevestre & Benn, 2015).

Iceberg Glacier's large total basin size (~1000 km^2), low surface slope, high length and large altitude range fit the geometric profile of surge-type glaciers in the CAA (Sevestre & Benn, 2015). To test whether the observed sequence of events match predictions made by the enthalpy balance model, key elements of the enthalpy budget would have to be quantified at different stages of the glacier's surge using equations provided by Benn et al. (2019b). However, the lack of observations during most of the 1980s prevents the testing of the theory for the first half of the surge, and the absence of high-resolution optical imagery prior to 1999 make it challenging to accurately map crevasse distribution throughout the surge.

2.5.4 Location of surge initiation

The presence of ice mélange at the glacier front in 1980–1981, the high (>1000 m a^{-1}) velocities recorded over the terminus region in 1981, and the ~100–400 m advance of the easternmost ~1.5 km of the terminus between 1980 and 1981, strongly suggests that Iceberg Glacier's surge initiated at the terminus. Up-glacier surge propagation from the terminus

accompanied by extensional crevassing has been reported several times for tidewater surge-type glaciers in Svalbard (e.g., Rolstaed et al., 1997; Luckman et al., 2002; Dowdeswell & Benham, 2003; Murray et al., 2003; Flink et al., 2015 Sevestre et al., 2018). Sevestre et al. (2018) suggest that during the late quiescent phase, internal thermodynamic processes resulting from the gradual steepening of the glacier surface, such as a velocity-strain heating feedback, and/or retreat from a pinning point, leads to the acceleration of the glacier front and the development of terminal crevasse fields. Crevasses then channel meltwater and rainwater to the glacier bed, resulting in flow acceleration and an upward migration of the crevasse field, which coincides with surge propagation (Sevestre et al., 2018). The westernmost ~2 km of Iceberg's terminus was located on a bedrock pinning point in 1981, which is visible as a rock ridge in front of the terminus in Figure 2.11a as well as in Figure 2.3b, while the rest of the terminus had retreated by more than 2 km from that bedrock perturbation. The centre part of the bedrock perturbation is also clearly visible at ~7 km from the 1997 terminus in Figure 2.10, which shows the 2014 ice surface and bed elevations along the centreline from 3D tomography radio-echo sounding data (https://data.cresis.ku.edu/) collected during a NASA Operation IceBridge flight on 25 March 2014. The retreat of a marine-terminating glacier from a pinning point into deeper water has been shown to increase thinning and retreat rates, while increasing ice velocities (O'Neel et al., 2005). Therefore, this process could have driven the large retreat of the eastern part of Iceberg's terminus from 1959 to 1981 and accelerated its thinning rate by increasing extension at the terminus.

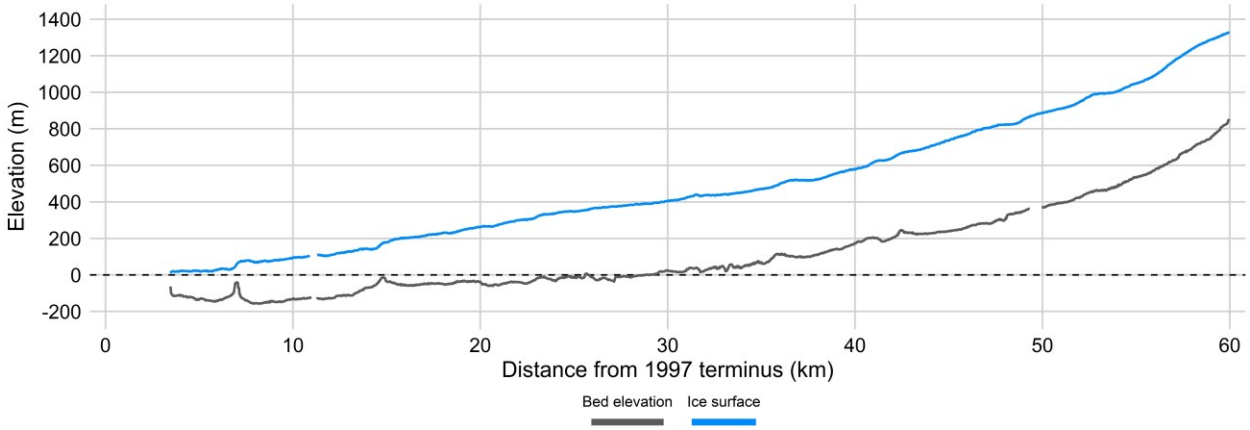

Figure 2.10. Ice surface (blue) and bed elevation (dark grey) profiles extracted along the centreline from 3D tomography radio-echo sounding data (https://data.cresis.ku.edu/) collected by NASA Operation IceBridge on 25 March 2014.

Substantial thinning of the terminus region results in an increase in buoyancy until the terminus reaches flotation, which is, in turn, followed by an acceleration of ice flow (O'Neel et al., 2005). To determine whether Iceberg Glacier was close to flotation near the start of its surge, we used the following equation presented in Cuffey & Paterson (2010) to quantify the thickness in excess of flotation by comparing the ratio of ice thickness to water depth:

$$H_b = H_M - \frac{\rho_w}{\rho_i} H_w \tag{2.3}$$

where H_M is total ice thickness, ρ_w is the density of water, ρ_i is the density of ice, and H_w is water depth. H_M was computed by subtracting the absolute bed elevation from Iceberg's surface elevation, while the absolute bed elevation was used to determine H_w. NASA Operation IceBridge 3D tomography radio-echo sounding data (https://data.cresis.ku.edu/) from 2014 was used for the bed elevation, while the 1977 KH-9 DEM and a 2016 ArcticDEM tile were used for the surface elevation. Flotation is likely to occur in areas where H_b approaches 0 or is negative.

The data from Iceberg Glacier shows that the majority of the ice front in 1977 had H_b values below 0, and reaching as low as approximately -30 m. While the KH-9 DEM has relatively high vertical uncertainties, and negative elevation values over parts of the terminus are

possibly due to the presence of deep potholes, these results suggest that a large part of Iceberg's terminus had reached flotation by 1977. The westernmost portion of the terminus remained far from flotation (up to ~25 m from flotation) due to the presence of the bedrock perturbation, which reaches elevations of up to ~100 m above sea level and stabilised that part of the terminus during the quiescent phase. That portion of the terminus also saw a much less pronounced acceleration in 1981 than the eastern portion, overall lower velocities during the active phase due to the compressional flow, increased driving stress resulting from the higher surface slope due to the bedrock perturbation, and significantly less thinning than the eastern side of the terminus from 1959 to 1977 (Figure 2.7a). Downstream from the bedrock pinning point, the glacier switched to extensional flow, leading to extensive transverse crevassing (Figure 2.3e).

In comparison, Iceberg Glacier's terminus was significantly less likely to float in 2016, with typical values of >10 m of thickness in excess of flotation (Figure 2.11b). Fundamentally, the lower ice thickness and deeper fiord waters over which the eastern half of the terminus was located in 1977 would have increased its buoyancy. Ice mélange developed between 6 July 1980 and 30 August 1980 as sea ice appears to have thinned and retreated from part of the glacier front during that period, which would have caused a reduction in buttressing at the terminus and coincident increase in ice movement and calving. Sea ice did not fully retreat from the glacier front in 1980, but in 1981 sea ice fully disappeared from Iceberg Bay between 19 July and 30 August, during which time the terminus region underwent a dramatic acceleration.

When the sequence of observed changes at Iceberg Glacier are put together, a likely sequence for the surge initiation is as follows: (1) more than half of Iceberg's terminus had retreated from a bedrock pinning point by 1966 and more than two thirds by 1981, which enhanced further retreat and increased extension, resulting in higher thinning rates and velocities;

(2) gradual steepening of the glacier surface throughout the quiescent period likely caused an increase in internal and basal temperatures as well as an increase in driving stress; (3) probable flotation of a large portion of Iceberg Glacier's eastern terminus occurred in the 1970s; and (4) the complete retreat of sea ice from the ice front in summer 1981 for the first time since September 1978 removed a major resistive buttressing force at the terminus, likely contributing to the initiation of Iceberg Glacier's surge in the early 1980s. Channeling of meltwater to the glacier bed as crevasses developed probably also played a role in flow acceleration and the up-glacier propagation of the surge from the terminus as described by Sevestre et al. (2018), although we lack sufficiently high spatial and temporal resolution data to confirm this.

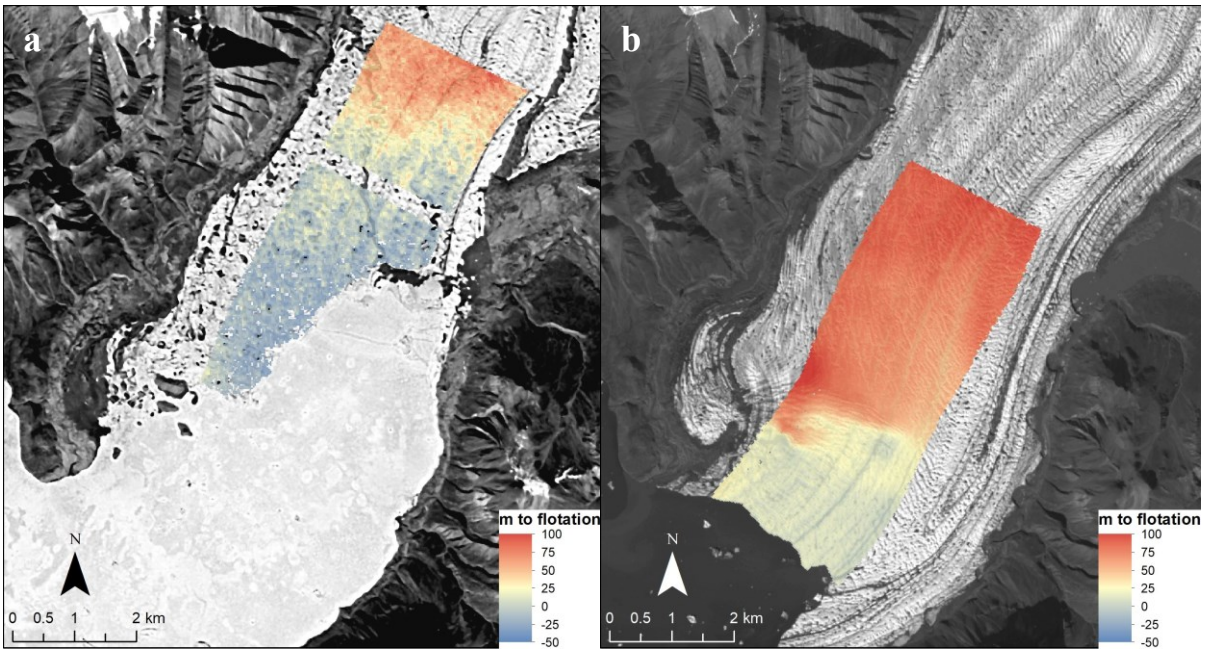

Figure 2.11. Thickness in excess of flotation for the terminus region of Iceberg Glacier in: (a) 1977 and (b) 2016 quantified by comparing the ratio of ice thickness to water depth (Equation 2.3). Ice thickness and water depth was derived from 3D tomography radio-echo sounding data (https://data.cresis.ku.edu/) collected by NASA Operation IceBridge on 25 March 2014 along with an (a) KH-9 DEM and (b) ArcticDEM tile (b). Base images: (a) KH-9, 13 July 1977 and (b) Landsat 8, 29 July 2016.

2.5.5 Comparison to other surge-type glaciers in the CAA

Besides Iceberg Glacier, the two other largest outlet glaciers on western Axel Heiberg Island, Airdrop (~600 km^2; land-terminating), and Good Friday (~800 km^2; marine-terminating), have also been previously classified as surge-type (Müller, 1969; Copland et al., 2003). These glaciers were deemed to be subject to surging behaviour based on the presence of surface features diagnostic of surging activity, such as large looped moraines, heavy crevassing, significant terminus advance over the period 1959–1999, and high ice surface velocities (Copland et al., 2003). However, neither Good Friday nor Airdrop have shown any cyclic variations in their dynamics characteristic of surge-type glaciers since observations began in the 1950s. Instead, both glaciers appear to have continuously advanced over the last seven decades and have maintained relatively high velocities during that period (Medrzycka et al., 2019; Chapter 3). However, Iceberg Glacier's highest measured velocity of ~2300 m a^{-1} at the terminus in summer 1991 is more than an order of magnitude higher than Airdrop's highest flow rate on record (Chapter 3). Nevertheless, both Good Friday and Airdrop have started slowing down nearly synchronously since the mid-2000s. Good Friday Glacier decelerated by ~50–100 m a^{-1} over that period (Medrzycka et al., 2019), while Airdrop Glacier slowed down by a factor of ~2.3 between 2006 and 2020–2021 within 7 km from its 2018 terminus position (Chapter 3). This deceleration has been interpreted as a possible slow transition to the quiescent phase of the surge cycle that spans more than a decade (Medrzycka et al., 2019; Van Wychen et al., 2021; Chapter 3), although alternate explanations for both glaciers' behaviour have been proposed, including a delayed response to positive mass balance conditions of the Little Ice Age and an unstable advance related to perturbations in Good Friday Glacier's bedrock topography (Medrzycka et al., 2019; Chapter 3).

If Good Friday and Airdrop are indeed surging, their several-decade-long active phase would likely fall under the category of a slow surge (Jiskoot, 2011; Chapter 3). Slow surges typically last longer than an ordinary surge with an active phase of >20 years, are subject to lower flow speeds and sometimes result in no change in terminus position (Jiskoot et al., 2011). Split Lake Glacier, a land-terminating glacier located on SE Ellesmere Island that has been actively surging for 50+ years and flowing at a velocity of up to >600 m a^{-1}, is the first to have been classified as a slowly surging glacier in the Canadian Arctic (Van Wychen et al., 2022). Considering Iceberg Glacier's active phase length of ~22 years, its significant terminus advance of ~7 km and sudden acceleration to velocities of >1500 m a^{-1}, it appears to best fit under the category of a classical (i.e., "normal") surge rather than a slow surge.

Other glaciers in the CAA have been shown to experience classical surges, which is best exemplified by the dynamics of Otto and Mittie glaciers on northern Ellesmere Island. Otto Glacier was reported by Hattersley-Smith (1964, 1969) to be undergoing a surge in 1963–1964 that began between 1950 and 1959 and reached a maximum measured velocity of 7.7 m d^{-1} (equivalent to 2800 m a^{-1}) in July–August 1959. The glacier started surging again in ~2000 and peaked at velocities of ~600–700 m a^{-1} in 2007/2008 over the glacier's lower 5 km (Van Wychen et al., 2016). The active phase of Otto's surge lasted for ~13 years, and the glacier is now flowing at a rate of <50 m a^{-1} (Van Wychen et al., 2021). Assuming that surging of that glacier is cyclical, these observations suggest a surge recurrence interval of ~30–35 years (Van Wychen et al., 2021).

Mittie Glacier, located on southern Ellesmere, was actively surging in 1999, with surface velocities of 1000 m a^{-1} over its entire 25 km length (Copland et al., 2003) and continued high velocities of up to ~1000 m a^{-1} at the terminus in 2003 and ~700 m a^{-1} in 2004 (Short & Gray,

2005). The glacier had reached stagnation by 2012, suggesting an active phase length of at least 5 years (Van Wychen et al., 2014). Ultimately, CAA glaciers appear to experience long surges when compared to the active phase length of 3–10 years for surge-type glaciers in Svalbard (Dowdeswell et al., 1991) and a generally slow transition from the active phase to the quiescent phase of the surge cycle. The length of the active phase for surge-type glaciers in the Canadian Arctic appears to vary between anywhere from >5 years to possibly up to >70 years, indicating that there exists a wide range of complex surge behaviour and dynamics within this region.

2.6 Conclusions

By combining remotely sensed data from a variety of sources from 1950 to 2021, our results support previous observations that suggested cyclic variations of Iceberg's dynamics (Copland et al., 2003; Short & Gray, 2005; Van Wychen et al., 2016), thus confirming its surge-type classification. Iceberg Glacier experienced a prolonged period of terminus retreat from 1950 to 1980, during which time the glacier was in the quiescent phase and velocities remained low within the terminus region throughout most of the 1970s. However, velocities within ~26 km from the 1997 terminus appear to have gradually increased from 1972 to 1980, with the greatest acceleration occurring over the eastern portion of the terminus between 1979 and 1980, while the westernmost ~2 km remained grounded on a bedrock pinning point. Ice mélange appeared at the glacier front in summer 1980, which was accompanied by an acceleration in ice movement at the terminus, following thinning and a slight retreat of the sea ice from the ice front. However, the sea ice did not completely retreat from the ice front until August 1981, which is when velocities reached up to ~1500 m a^{-1} within Iceberg Glacier's terminus region and the active phase of the surge began.

We hypothesize that the retreat of the eastern portion of Iceberg Glacier's terminus from the bedrock pinning point leading to greater retreat and thinning rates, internal thermodynamic processes, a large portion of the terminus becoming subject to flotation in the 1970s, and the removal of the buttressing force exerted by the sea ice on the ice front in 1981, all likely played a role in surge initiation at the terminus. The surge resulted in a maximum terminus advance of >7 km in 1997 compared to pre-surge extent in 1980, a peak velocity of ~2300 m a^{-1} in summer 1991, and a large drawdown of mass causing pronounced thickening at the terminus. Iceberg Glacier started decelerating after its maximum recorded velocity in 1991 and became quiescent again in 2003, suggesting an active phase length of 22 years. During the current quiescent phase, a high rate of terminus retreat has been accompanied by a long-term decrease in ice velocities that reached an average centreline flow rate of ~11.5 m a^{-1} in 2020–2021, while surface elevation trends show mass accumulation over the glacier's upper reservoir zone and mass loss over the lower receiving zone. The 2003–2021 elevation change trends indicate a dynamic balance line at ~30–33 km from the 1997 terminus position along the main trunk (Figure 2.7c).

This study provides the first detailed reconstruction of an entire surge cycle for a glacier in the Canadian Arctic and reveals insights into the mechanisms that drive surging in this region. We conclude that Iceberg Glacier's surge most closely resembles a thermally-triggered Svalbard-type surge, however, hydrological changes at the glacier bed through channeling of meltwater via crevasses could also play an important role in regulating surging (e.g., Dunse et al., 2015; Sevestre et al., 2018; Benn et al., 2019b; Haga et al., 2020). If Airdrop and Good Friday glaciers are indeed surge-type, it would be puzzling as to why two nearby surge-type glaciers would behave this differently from Iceberg Glacier, with an active phase length of possibly more than 3 times that of Iceberg's. Additional research is needed to understand the precise mechanisms

causing certain glaciers to undergo long-term advances and/or slow surges, while other glaciers of similar geometries and subject to similar environmental conditions undergo shorter, more intense surges. Ultimately, comprehensive studies of glacier surging in the Canadian Arctic and testing the enthalpy balance theory of surging (Benn et al., 2019a,b) on a regional basis could help elucidate the factors triggering these velocity fluctuations and causing the observed variety of glacier dynamic behaviour, which is necessary to improve our understanding of how these glaciers are responding to a warming climate.

Chapter 3: Evolution in surface morphology and velocity of Airdrop Glacier, western Axel Heiberg Island, over a seven decade long advance

3.1 Introduction

Glaciers in the Canadian Arctic Archipelago (CAA: Ellesmere, Axel Heiberg, and Devon islands) demonstrate a high degree of spatial and temporal variability in their dynamics. The negative mass balance conditions that have prevailed in this region during the last few decades (Koernet, 2005; Gardner et al., 2011; Lenaerts et al., 2013; Millan et al., 2017; Thomson et al., 2017; Mortimer et al., 2018; Noël et al., 2018; Ciracì et al., 2020) have been accompanied by widespread terminus retreat, lower ice velocities, and glacier thinning (Schaffer et al., 2017; Strozzi et al., 2017; Thomson et al., 2017; Thomson & Copland, 2018; Mortimer et al., 2018). Nevertheless, some large tidewater glaciers, such as Trinity, Wykeham, and Belcher glaciers have undergone a dramatic acceleration as a result of dynamic thinning (Van Wychen et al., 2016, 2017; Harcourt et al., 2020). Moreover, other tidewater glaciers have experienced marked interannual velocity variations, accompanied by changes in their terminus position and ice thickness (Van Wychen et al., 2014, 2016). A few tidewater glaciers have also undergone pulse-like variations in their velocities, with these glaciers differing from surge-type glaciers due to the fact that the flow variability is typically restricted to the lowermost terminus regions that are grounded below sea-level, with bed elevations rising above sea level appearing to limit the up-glacier propagation of the pulse (Van Wychen 2016, 2017).

Despite being outside of the optimal climatic envelope for surging, more than 50 surge-type glaciers have been identified in the Canadian Arctic (Copland et al., 2003; Sevestre & Benn, 2015). The most significant terminus advances out of the 51 surge-type glaciers inventoried by

Copland et al. (2003) in the CAA occurred on western Axel Heiberg Island, in the northern CAA. Out of 13 glaciers with signs of unstable flow on Axel Heiberg Island, the three largest (Airdrop, Iceberg, and Good Friday), were the only ones defined as 'confirmed' surge-type by Copland et al. (2003). Iceberg, Airdrop, and Good Friday glaciers underwent 4.5, 5, and 7 km of terminus advance from 1959 to 1999, respectively (Copland et al., 2003). However, only the dynamics of Good Friday Glacier have been analysed in detail thus far in the literature, with Medrzycka et al. (2019) reporting that it underwent an uninterrupted terminus advance of ~9.3 km between 1948 and 2018, although ice velocities have been decreasing since the late 1980s. Medrzycka et al. (2019) state that it is unclear whether this advance is the result of the active phase of a surge, or whether it was caused by a delayed response to positive mass balance conditions of the Little Ice Age (LIA), or some other type of dynamic instability, such as perturbations in bedrock topography.

The aim of this study is to improve our understanding of the complex behaviour and dynamics of glaciers in the Canadian Arctic by reconstructing the changes of Airdrop Glacier from 1950 to 2021. The terminus of this glacier is significantly more advanced now than it was in 1950, but the details of the timing of this advance along with the associated changes in ice motion and surface elevation are currently poorly constrained, and it is unclear whether the advance can be best explained by surging or another mechanism. Our assessment is undertaken by utilising a wide array of remotely sensed data, such as historical aerial photographs, declassified intelligence satellite photographs, optical satellite imagery, and synthetic aperture radar (SAR) data.

3.2 Study site

More than a quarter of Axel Heiberg Island's total land area of 43,000 km^2 is covered by glaciers, with Steacie Ice Cap in the south and Müller Ice Cap in the north (Ommanney, 1969; Thomson et al., 2011). This region has a cold and dry climate with mean annual temperatures of ~-20˚C and mean annual precipitation ranging from 58 mm a^{-1} at sea level measured at Eureka, 100 km to the east (Figure 3.1), to 370 mm a^{-1} at 2120 m a.s.l. (Cogley et al., 1996a; Thomson et al., 2017). The surface motion in the interior of the two ice caps on Axel Heiberg, where the majority of the ice is frozen to its bed and flowing as a result of internal deformation alone, remains below 20 m a^{-1} (Van Wychen et al., 2016). As the ice is channeled down-glacier towards glacier termini, which raises the potential for a transition from cold to warm basal conditions as well as changes in bedrock topography (sills and steps), velocities typically increase along the main trunk of outlet glaciers (Van Wychen et al., 2016). Surface velocities of land-terminating glaciers generally remain below 75 m a^{-1}, with the two only exceptions being Airdrop Glacier and the upper half of Thompson Glacier (Van Wychen et al., 2016; 2021). Müller Ice Cap's sole marine-terminating glacier, Iceberg Glacier, is currently stagnant along its main trunk (<20 m a^{-1}), but its tributaries have velocities of up to ~75 m a^{-1} (Van Wychen et al., 2021), and terminus velocities reached >2000 m a^{-1} during a surge between the early 1980s and 2003 (Chapter 2). On the other hand, Good Friday Glacier, the only marine-terminating glacier draining Steacie Ice Cap, has velocities of 100–250 m a^{-1} along its main trunk and >350 m a^{-1} at the terminus (Medrzycka et al., 2019).

Airdrop Glacier (79.84˚N, 93.28˚W; Figure 3.1) is a land-terminating glacier with a basin size of ~600 km^2 that drains the west side of Müller Ice Cap that was first identified as a surge-type glacier by Copland et al. (2003). "Airdrop Glacier" is an unofficial name, and is sometimes

also referred to as “Middle Glacier” since the glacier feeds Middle Fiord. The glacier showed signs of surging both in 1959 and 1999, with extensive surface folding and looping of surface moraines apparent in both years, and intense crevassing in 1999 satellite imagery (Copland et al., 2003). The glacier had advanced by ~4.5 km between 1959 and 1999, and saw an 18.45 km^2 increase in its area from 1959 to 2000 (Thomson et al., 2011). In the year 2000 the glacier had a velocity of ~150–180 m a^{-1} and was determined to have a latest surge initiation of 1975 (Thomson et al., 2011). According to a subsequent study by Van Wychen et al. (2016), Airdrop Glacier advanced by a further ~1 km from 2000 to 2014 and reduced in velocity from 165 m a^{-1} in 2000 to 75 m a^{-1} in 2015, which they argued could be indicative of a transition to the quiescent phase of the surge cycle.

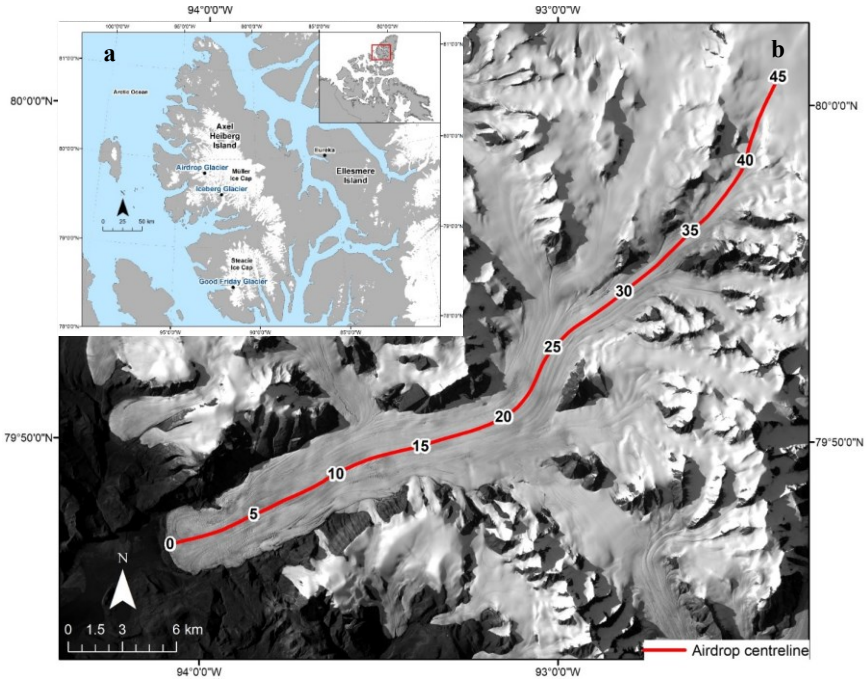

Figure 3.1. (a) Location of Airdrop Glacier, Iceberg Glacier, and Good Friday Glacier on Axel Heiberg Island, Nunavut. (b) Airdrop Glacier centreline (red line) and 5 km markers starting from the glacier’s 2018 terminus position. Base image: Landsat 8, 12 August 2020. Data: Statistics Canada, 2016 Census. Provinces/territories – Cartographic Boundary File (https://www12.statcan.gc.ca/census-recensement/2011/geo/bound-limit/bound-limit-2016-eng.cfm). Natural Resources Canada. Lakes, Rivers and Glaciers in Canada – CanVec Series – Hydrographic Features (https://open.canada.ca/data/en/dataset/9d96e8c9-22fe-4ad2-b5e8-94a6991b744b).

3.3 Methods

3.3.1 Terminus position

A total of 43 historical aerial photographs, declassified spy satellite images, optical satellite images, and synthetic aperture radar (SAR) scenes were used to manually outline the terminus position of Airdrop Glacier in ArcGIS 10.8.1 from 1959 to 2021 (Table 3.1). Nadir and oblique historical aerial photographs from 1950 and 1959 were acquired from the National Air Photo Library (NAPL), Ottawa, Canada. The 1950 photos were acquired by the Royal Canadian Air Force (RCAF) during a trimetrogon survey (i.e., one camera pointing nadir and two pointing to either side of the flight path) at an altitude of 19500–22000 ft (5944–6706 m) above sea level (a.s.l.), with each nadir image covering a ground area of ~14 km x 14 km (Cogley & Adams, 2000). The 1959 survey acquired nadir images at an altitude of ~30000 ft (~9000 m) a.s.l., which were used by Ommanney (1969) to create the first inventory of Axel Heiberg Island's ice masses.

A pair of declassified spy satellite images from the KH-4 Corona Cold War era reconnaissance satellite from 1966 and 1977, respectively, were downloaded from the United States Geological Survey (USGS) Earth Explorer data portal (http://earthexplorer.usgs.gov). These were acquired in stereoscopic (stereo) mode and provide a ground resolution of approximately 4.7.

For the purpose of terminus delineation, the scanned historical aerial photographs and declassified spy satellite images were cropped to the terminus region of Airdrop Glacier and manually georeferenced using a first order polynomial (affine) transformation and a minimum of 8 tie points in ArcGIS. The 1959 and 1966 outlines were delineated using a historical aerial photograph and a KH-4 Corona declassified spy image, respectively (Table 3.1). No 1950 nadir

air photographs covered the terminus of Airdrop, so oblique photos of the terminus were used to determine its approximate position in relation to the 1959 position.

All of the terminus positions since 1972 were mapped using satellite imagery, the majority of which was optical (Table 3.1). This imagery consists of Landsat 1–8 Level 1TP (i.e., precision and terrain corrected) scenes obtained from the USGS Earth Explorer data portal (http://earthexplorer.usgs.gov) and Advanced Spaceborne Emission and Reflection Radiometer (ASTER) L1T (i.e., calibrated-at-sensor radiance that is geometrically corrected and projected in UTM coordinates) acquired from the USGS Earth Explorer data portal, NASA's Earthdata search portal (https://search.earthdata.nasa.gov/search), and the METI AIST Data Archive System (https://gbank.gsj.jp/madas/map/index.html). When available, July to September (i.e., late summer) images were preferentially chosen to ensure minimal snow cover and sea ice. The Landsat and ASTER scenes were all radiometrically/geometrically corrected, and thus no pre-processing was required.

The synthetic aperture radar (SAR) data used for the terminus analysis consists of several European Remote-Sensing Satellite (ERS) 1 and 2 scenes for the period 1991–2011, along with a single 1996 RADARSAT-1 scene, obtained from the Alaska Satellite Facility Data Search portal (https://search.asf.alaska.edu). The SAR data were downloaded as Level One (i.e., processed) products and geocoded to NAD 1983 Zone 15N with the ASF MapReady software to create a GeoTIFF file of each scene. Some of the ERS scenes were not accurately georeferenced and, therefore, had to be manually adjusted using the Shift tool from the Georeferencing toolbar in ArcGIS to properly align bedrock features in the terminus region with the same features in recent Landsat 8 scenes. Due to the limited high latitude coverage of the early Landsat satellites, the

ERS imagery was used to fill some data gaps in the 1990s (Table 3.1). Unfortunately, no imagery was available from 1982 to 1991.

Total and mean yearly changes in terminus position were quantified along Airdrop Glacier's centreline for different periods (e.g., 1959–1966, 1966–1972, 1972–1981). The maximum uncertainty resulting from the manual outlining of the terminus position of Airdrop Glacier was conservatively estimated to be 2 pixels (Kochtitzky et al., 2019). This translates to a total uncertainty of 120 m for Landsat 1–3, 60 m for Landsat 4–5, 30 m for Landsat 7–8, 25 m for ERS-1/2 and RADARSAT-1, ~11.4 m for the 1959 historical aerial photograph, and ~9.4 m for the KH-4 image. With the assumption that uncertainties are caused by random error (i.e., independent from one another) and there is no systematic bias, uncertainties for the mean terminus position change rate of Airdrop Glacier over the different time periods were calculated from:

$$Uncertainty = \frac{\sqrt{(pixel\ length)^2 + (pixel\ width)^2}}{number\ of\ years} \quad (2.1)$$

Table 3.1. Imagery used for mapping the terminus positions of Airdrop Glacier in this study.

Acquisition date	Image ID	Resolution (m)	Satellite/Photographer
28/07/1959	A16754_053	~5.7	RCAF
14/08/1966	DS1036-1082DF023_d	~4.7	KH-4 Corona
28/08/1972	LM01_L1T06200219720828	60	Landsat 1
23/05/1973	LM01_L1T06300219730526	60	Landsat 1
19/08/1974	LM01L1TP06300219740819	60	Landsat 1
24/07/1975	LM02L1TP06900119750724	60	Landsat 2
22/09/1976	LM02L1TP06300219760922	60	Landsat 2
29/08/1977	LM02L1TP06200219770829	60	Landsat 2
03/09/1978	LM03L1TP06300219780903	60	Landsat 3
29/07/1979	LM03L1TP06800119790729	60	Landsat 3
19/09/1980	LM02L1TP06300219800919	60	Landsat 3
31/08/1981	LM02L1TP06600219810830	60	Landsat 2
09/08/1991	LT05L1TP05300319910809	30	Landsat 5
05/11/1992	E1_06833_STD_F203	12.5	ERS-1
06/11/1993	E1_12072_STD_F203	12.5	ERS-1
07/10/1994	E1_16876_STD_F203	12.5	ERS-1
29/09/1995	LT05L1TP06100219950929	30	Landsat 5
29/10/1996	R1_05151_ST6_F199	12.5	RADARSAT-1
07/11/1997	E2_13327_STD_F203	12.5	ERS-2
24/03/1998	E2_15288_STD_F203	12.5	ERS-2
25/07/1999	LE07L1TP05800219990725	15	Landsat 7
29/09/2000	LE07L1TP05600220000729	15	Landsat 7
26/06/2001	LE07L1TP06000220010626	15	Landsat 7
12/06/2002	LE07L1TP05800220020615	15	Landsat 7
11/07/2003	AST_L1T_00307112003202307	15	ASTER
20/07/2004	AST_L1T_00307202004003948	15	ASTER
29/07/2005	AST_L1T_00307292005195221	15	ASTER
09/07/2006	AST_L1T_00307092006013457	15	ASTER
15/08/2007	AST_L1T_00308152007193453	15	ASTER
02/07/2008	LT05L1TP05700220080702	30	Landsat 5
16/07/2009	LT05L1TP05400320090716	30	Landsat 5
05/07/2010	AST_L1B_00307052010004005	15	ASTER
23/07/2011	AST_L1T_00309232011195817	15	ASTER
20/07/2012	AST_L1T_00309202012194021	15	ASTER
14/09/2013	LC08L1TP06100220130914	15	Landsat 8
12/08/2014	LC08L1TP09024220140812	15	Landsat 8
01/09/2015	LC08L1TP05600220150901	15	Landsat 8
29/07/2016	LC08L1TP06000220160729	15	Landsat 8
28/08/2017	LC08L1TP05700220170828	15	Landsat 8
21/08/2018	LC08L1TP09224120180821	15	Landsat 8
19/09/2019	LC08L1TP05700220190919	15	Landsat 8
07/08/2020	LC08L1TP08724220200807	15	Landsat 8
15/08/2021	LC08L1TP09024220210815	15	Landsat 8

3.3.2 Ice velocities

3.3.2.1 Feature-tracking

Velocities from 1972 to 1981 were extracted from Landsat 1–3 imagery using the Glacier Image Velocimetry (GIV) app developed by Van Wyk de Vries & Wyckert (2021). GIV, like most other software used to derive glacier motion, uses a feature-tracking algorithm, which matches offsets by finding corresponding features or image patches in two or more images (Debella-Gilo & Kääb, 2011). The measurement of the displacement of features between images over a specific time interval is used to compute ice surface velocities. Landsat 1–3 near annually separated satellite images with a matching orbital geometry (i.e., same path and row) were clipped to Airdrop Glacier and its immediate surroundings before inputting the data into GIV. Due to slightly inaccurate georeferencing of some of the early Landsat images, a few of the scenes had to be manually shifted, as described in Section 3.3.1.

Once the surface velocities were extracted from all image pairs with GIV, filtering of the velocity data based on flow orientation was undertaken to exclude cells with an orientation value outside of the range of 165–300˚. This helps filter out potentially erroneous velocities resulting from false matches. The range of flow direction value accounts for ~45˚ in variability relative to the orientation of Airdrop's centreline in a downstream direction. Raster Calculator in ArcGIS was used to exclude flow direction cells outside of the specified range. Subsequently, the Extract by Mask tool was used to mask the velocity map to the extent of the filtered flow direction map. The per-cell mean value of all velocity rasters derived from Landsat 1–3 imagery (i.e., 1972–1981) was then calculated using the Cell Statistics tool in ArcGIS to provide near complete coverage of the glacier surface, as automated velocity mapping with the coarse resolution of

early Landsat satellites often results in poor coverage and noisy results from individual scene pairs.

3.3.2.2 GAMMA InSAR

Interferometric SAR (InSAR) processing of ERS-1/2 data with GAMMA software was used to derive velocities for 1992 and 1997 at a time when optical satellite imagery was sparse at high latitudes. The ERS-1/2 scene pairs were acquired with the same orbital geometry (i.e., same path and frame) with a time separation of 30 and 35 days for 1992 and 1997, respectively, and downloaded as Level 0 (i.e., unprocessed) products from the ASF Data Search website. To compute displacements (offsets) between each pair of SAR scenes, the raw SAR data was converted to Single Look Complex (SLC) and multi-look intensity images in radar range-Doppler coordinates with the GAMMA Module SAR Processor.

For each scene pair in GAMMA InSAR, the first step consisted of co-registering the two images using orbit and terrain height data by resampling the second image into the geometry of the first. The offset between the two images was then computed using the orbital data and refined with a two-dimensional cross-correlation analysis. Next, the filtered offset map was used to estimate range and azimuth displacements with a cross-correlation optimization between both scenes. The displacements were thereafter converted from RADAR geometry to meters in ground range. To convert the displacements from SAR range/Doppler coordinates into UTM map projection coordinates, a lookup table was created from the ASTER GDEM and was applied to add the georeferencing information to the centre of every matching window used to calculate the displacements. The total displacement values were computed from:

$$Total\ displacement = \sqrt{(range\ displacement^2) + (azimuth\ displacement^2)} \quad (2.2)$$

3.3.2.3 NASA ITS_LIVE

NASA's Inter-mission Time Series of Land Ice Velocity and Elevation (ITS_LIVE) dataset (https://its-live.jpl.nasa.gov/; Gardner et al., 2019) was used to acquire all surface velocities of Airdrop Glacier since 1999–2000. The NASA Jet Propulsion Laboratory derived these data predominantly from Landsat 4, 5, 7, and 8 imagery using the autonomous Repeat Image Feature Tracking (auto-RIFT v0.1) processing scheme (Gardner et al., 2018). The data are available either as individual image-pair velocities with a time separation of 6 to 546 days, or as monthly or annual velocity mosaics created from the compilation of all scene-pair velocities. They have a spatial resolution of either 120 m or 240 m.

The 2000–2018 ITS_LIVE annual mean surface velocity composites for Arctic Canada North were subsetted to Axel Heiberg Island. Scene-pair velocities were also acquired to fill in data gaps because some years between 2000 and 2008 have limited coverage of Airdrop Glacier. In addition, image-pair velocities were used for 2019–2021 since version 1 of the annual mosaics does not cover those years. Some years, such as 2019–2021, had a few thousand available scene-pair velocities and, therefore, had to be filtered by setting a minimum time separation between the two scenes of >60 days and/or a minimum coverage (i.e., the percentage of possible glacier pixels that have reported velocities) of 10–90% based on the amount of data available for a specific year. After downloading all of the image-pair data, the datasets with the best coverage of Airdrop Glacier and smallest apparent uncertainties were kept.

The GeoTIFF velocity files, along with all other rasters used in this study, were projected to NAD 1983 Zone 15N and standardized to annual values. The uncertainties for the GIV, GAMMA, and NASA ITS_LIVE scene-pair data were estimated by quantifying the median and SD velocity over non-glacierised terrain (i.e., bedrock) surrounding Airdrop Glacier (Table 3.2;

Appendix A). Due to the presence of outliers in the data, the median value was used rather than the mean in order to provide a more accurate measure of central tendency. ITS_LIVE files of the velocity errors for the annual mosaics between 2000 and 2018 were downloaded, and the median error value over Airdrop was computed to estimate ice flow uncertainties (http://its-live-data.jpl.nasa.gov.s3.amazonaws.com/documentation/ITS_LIVE-Regional-Glacier-and-Ice-Sheet-Surface-Velocities.pdf provides a description of how the errors were quantified).

Table 3.2. Landsat (L) and ERS scene pairs used to derive surface velocities of Airdrop Glacier, with associated uncertainty quantified by the apparent motion over adjacent non-glacierised terrain.

Satellite	First scene	Second scene	Uncertainty: median/SD (m a^{-1})
L1	23/09/1972	12/09/1974	17.3 ± 12.52
L1/L2	19/08/1974	06/08/1975	34.9 ± 24.2
L2	10/09/1975	04/09/1976	38.3 ± 28.5
L2	03/08/1976	29/07/1977	55.8 ± 27.3
L2	12/07/1977	04/07/1978	18.2 ± 16.8
L2/L3	03/09/1978	07/09/1979	34.4 ± 22.8
L2	07/09/1979	19/09/1980	43.2 ± 29.9
L2	19/09/1980	30/08/1981	26.8 ± 24.7
ERS-1	06/02/1992	07/03/1992	23.8 ± 15.9
ERS-2	08/04/1997	13/05/1997	14.5 ± 18.2
L7	20/07/1999	20/06/2000	5.0 ± 4.5
L7	11/06/2000	14/06/2001	6.0 ± 5
L7	15/06/2001	18/06/2002	7.0 ± 6.7
L7	15/06/2004	02/06/2005	4.0 ± 4.2
L7	09/06/2005	14/07/2006	4.0 ± 3.2
L8	05/05/2019	07/05/2020	5.0 ± 4.5
L8	11/05/2020	14/05/2021	3.0 ± 4.0

3.3.3 Surface elevation

3.3.3.1. sPyMicMac

A DEM was generated from a pair of stereo KH-9 Hexagon declassified images (DZB1213-500054L001001 and DZB1213-500054L002001) from 13 July 1977, enabling the

surface elevation change record of Airdrop Glacier to be extended prior to the year 2000. The processing was done using sPyMicMac, a set of Python tools for processing historical aerial photos and spy satellite imagery (https://spymicmac.readthedocs.io). Before going through the general workflow, the KH-9 images need to be processed, which includes resampling, removal of Reseau marks, image joining, and contrast enhancement. Distortions in the film, caused by storage and other conditions, were rectified by resampling the images based on the locations of Reseau marks, which were automatically detected and removed by sPyMicMac. USGS scans each KH-9 image in two halves due to the large size of the film (~9”x18”), leaving a small amount of overlap that sPyMicMac uses to join the two halves together. Next, the two joined images were processed with a median filter to reduce noise, followed by the application of a contrast stretch and a gamma adjustment to enhance the initially low contrast of both KH-9 images.

Once the pre-processing of the images was complete, the first step of the general workflow consisted of computing tie points by matching all pairs of images. Afterwards, the relative orientation of each image was determined using a basic radial distortion model and holding a fixed focal length. Using the orientation files created from this process, relative orthoimages and DEM were generated, and a relative orthomosaic was created from the individual orthoimages. Georeferencing the relative DEM and orthomosaic to absolute space was completed automatically with sPyMicMac by finding control points using a 2020 Sentinel-2 mosaic as the reference orthoimage, the ASTER GDEM (Global Digital Elevation Model) as the reference DEM, image footprints gathered from USGS, as well as a modified version of the Randolph Glacier Inventory (RGI) 6.0 outlines as an exclusion mask to avoid searching for matches over glaciers or the ocean/sea ice. The control points that were computed, and the folder

containing the absolute orientation files, were then used to compute the absolute (i.e., georeferenced) orthomosaic and DEM. A more detailed description of each step of sPyMicMac's workflow can be found at https://spymicmac.readthedocs.io/en/v0.1.1/tutorials/index.html.

3.3.3.2. MMASTER

MicMac ASTER (MMASTER; Girod et al., 2017) was used to derive DEMs from stereo ASTER imagery for the period 2000–2021. ASTER imagery has previously been used to produce the ASTER global digital elevation model (GDEM), but this is a blended product, meaning that the dates of individual elevations are unknown. In addition, noise is present in the satellite data in the form of "jitter" (i.e., uncorrected errors in the imagery geometry due to sensor motion), which can result in anomalies and artifacts (Girod et al., 2017). The MMASTER software package was therefore produced by Girod et al. (2017) with the goal of computing DEMs from ASTER stereo imagery that has less overall noise and unmatched areas in comparison to the ASTER GDEM and NASA's AST14DMO product. The resulting DEMs have a horizontal resolution of 30 m or less and a vertical uncertainty of 10 m (Girod et al., 2017).

Using a cloud filter to exclude scenes with a cloud cover greater than 80%, a total of 816 L1A ASTER scenes (i.e., reconstructed unprocessed instrument data) were downloaded over Airdrop Glacier and its surrounding area from NASA's Earthdata Search portal. DEMs from the raw L1A raster data products were generated with batch processing of the MMASTER workflow. Running MMASTER is a computationally intensive process, so batch processing was conducted on the Cedar supercomputer from Compute Canada (https://docs.computecanada.ca/wiki/Cedar). Visual inspection of the resulting DEMs was

undertaken to remove those with high levels of noise due to factors such as cloud cover and those with minimal coverage of Airdrop Glacier.

3.3.3.3 Co-registration and trend analysis

The dem-coregistration Python package (https://github.com/iamdonovan/dem-coregistration) by Robert McNabb, which is based on the co-registration algorithm described by Nuth & Kääb (2011), was used to iteratively co-register the DEMs created with sPyMicMac and MMASTER. Overlapping bedrock elevations, which were extracted by masking glacierised pixels using the RGI 6.0 glacier outlines, were used in the batch processing of the co-registration process.

The co-registered DEMs were then post-processed by spatially and temporally filtering outliers using automated models created with ModelBuilder in ArcGIS. This was done by computing the differences between each DEM and the ASTER GDEM and excluding pixels with a difference value greater than a certain threshold. An appropriate threshold value for each 5-year period (i.e., 2001–2006, 2006–2011, 2011–2016, 2016–2021) that would allow differentiation of real elevation changes on the glacier surface from noise due to cloud cover or other biases was determined by visually analysing the elevation difference maps. Large elevation changes were consistently most notable at the terminus region of Airdrop Glacier, so a second-order spatial filtering was undertaken to use a smaller threshold for the remainder of the glacier surface while keeping the original threshold value for the terminus region. Thresholds for the terminus area of Airdrop Glacier for the 5-year periods were between 35 and 40 m, while thresholds for the remainder of the glacier ranged from 85 to 110 m

Subsequently, trends in elevation changes for Airdrop Glacier were computed using the make_stack.py script from the pygeotools Python package for the for the 5-year periods 2001–

2006, 2006–2011, 2011–2016, 2016–2021, as well as for 2001-2011, 2011-2021, and 2001-2021. The make_stack.py script uses a raster time series object (i.e., a stack of input rasters) from which a linear regression is calculated to compute a variety of statistics from the input DEMs, such as the minimum, maximum, mean, and trend value on a per-pixel basis. Differencing and computing trends from multiple DEMs in this way typically results in lower uncertainties than differencing just one DEM from another. Since no other elevation datasets exist between the 1977 KH-9 DEM and the ASTER DEMs, elevation changes between 1977 and 2001 had to be calculated by computing the difference between the two DEMs using the Minus tool in ArcGIS, which subtracts, for each cell, the value of the second input raster from the value of the first input raster. Elevation change trends were standardized to annual values. The median elevation change trend value for 1977–2001 and 2001–2021 was computed for each 10 m elevation contour (hypsometric band) across the glacier surface, based on the mean 2001–2021 elevation values. The uncertainties for the glacier surface elevation change trends were quantified by calculating the median absolute value over stable (i.e., non-glacierised) terrain (Appendix A).

3.4 Results

3.4.1 Terminus position

The terminus of Airdrop Glacier underwent a ~6 km advance over the 1950–2021 study period (Figure 3.2). Most years with available imagery show an advance outside of the terminus delineation uncertainty of two pixels, indicating that the glacier experienced a continuous advance over the last ~70 years. Despite this large advance, Airdrop has remained land-terminating throughout the study period, and its terminus is currently located ~4.5–5 km east of the ocean. Although the advance was uninterrupted over the entire study period, it occurred at

varying rates. From 1950 to 1959 the terminus appears to have slightly advanced, although it is difficult to precisely quantify this since the 1950 RCAF aerial photograph was taken in an oblique orientation pointing down-glacier from Airdrop's upper half. The rate of terminus advance increased after the 1950s to average rates of >100 m a^{-1} from 1966 to 2000, and reached a peak of 131.2 ± 6.4 m a^{-1} in 1981–1991, after which it has been slowing down towards present day (Table 3.3). Airdrop's terminus advanced by a total of ~2.3 km from 1981 to 2000, but has only experienced ~1.2 km of additional advance since 2000. This decrease in the rate of terminus advance has been most notable over the last 11 years, with the 2010–2021 average advance rate of 31.5 ± 1.9 m a^{-1} being nearly 3 times lower than in the previous decade (89.8 ± 1.9 m a^{-1}) and more than 4 times lower than the peak advance rate in 1981–1991 (Table 3.3).

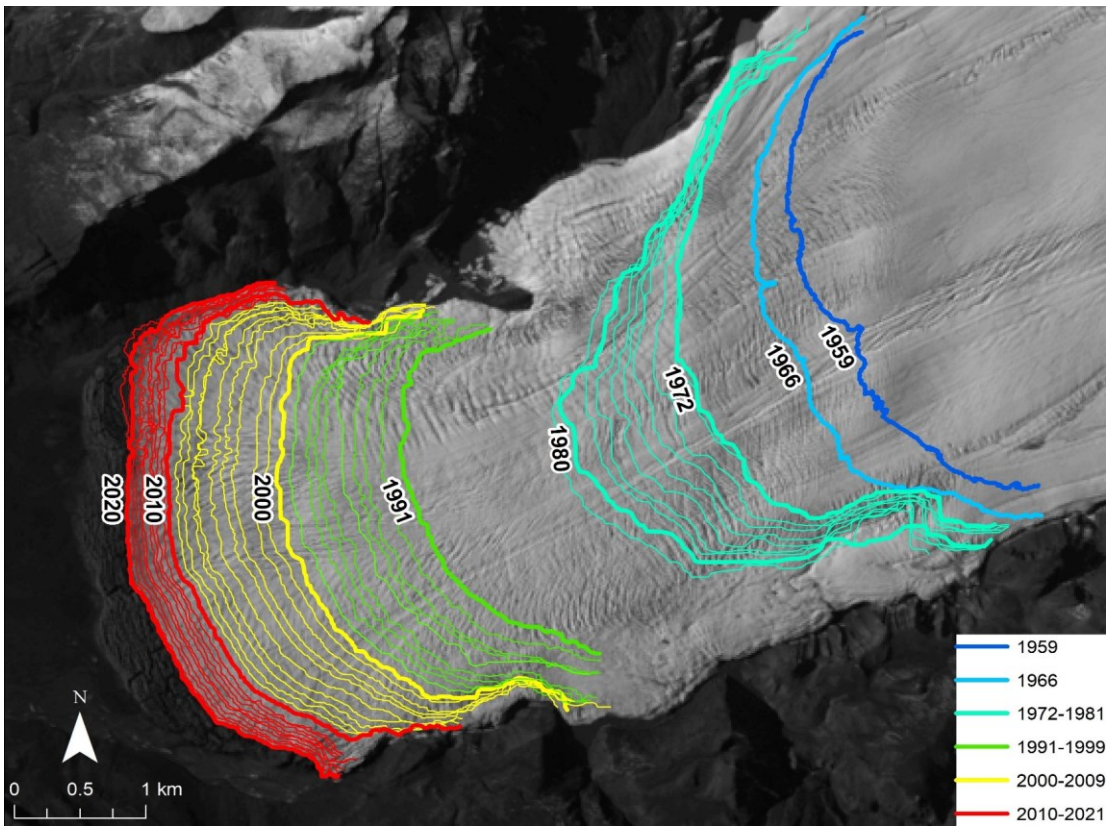

Figure 3.2. Evolution of the terminus position of Airdrop Glacier from 1959 to 2021. The colour palette ranges from blue (earliest) to red (latest) while certain years are annotated and their respective terminus lines are thicker to help with visual interpretation. Base image: Landsat 8, 7 August 2020.

Table 3.3. Total centreline advance and mean yearly advance rates of Airdrop Glacier's terminus as well as the associated uncertainty for different periods from 1959 to 2021.

Time period	Total advance (m)	Mean advance rate (m a^{-1})	Uncertainty (m a^{-1})
1959–1966	412.9	59	1.1
1966–1972	777.6	129.6	7.6
1972–1981	1132.3	125.8	9.4
1981–1991	1311.8	131.2	6.4
1991–2000	976.3	108.5	2.6
2000–2010	897.6	89.8	2.5
2010–2021	346.1	31.5	1.9

The shape of the terminus has altered throughout the study period as the glacier passed through a topographic constriction in the 1970s at the narrowest point of the valley, which is visible in front of the terminus in the 1959 RCAF air photo (Figure 3.3a). The southern end of Airdrop's terminus had reached the topographic constriction by 1966, while the northern end of the terminus had reached it by 1972, restricting the transverse flow of the ice and resulting in a much narrower ice front as the ice was channeled through the constriction. Airdrop's terminus attained its largest width at less than 1 km from the ice front in 1959 (Figure 3.3a) and at >2 km in 1977 (Figure 3.3b). The absence of transverse ice flow is reflected by the absence of splaying crevasses along the terminus region during the 1970s (Figure 3.3b), which later reappeared in the 1990s once the terminus started spreading out laterally again to cover a larger area as Airdrop Glacier had passed the narrowest part of the valley constriction (Figure 3.3c). Images from 1959, 1977, 1999, and 2021 show surface features diagnostic of surging, such as heavy crevassing as well as extensive folding and looping of surface moraines (Figure 3.3). Copland et al. (2003) used these observations from the 1959 aerial photography and a 1999 Landsat 7 image to classify Airdrop as a 'confirmed' surge-type glacier.

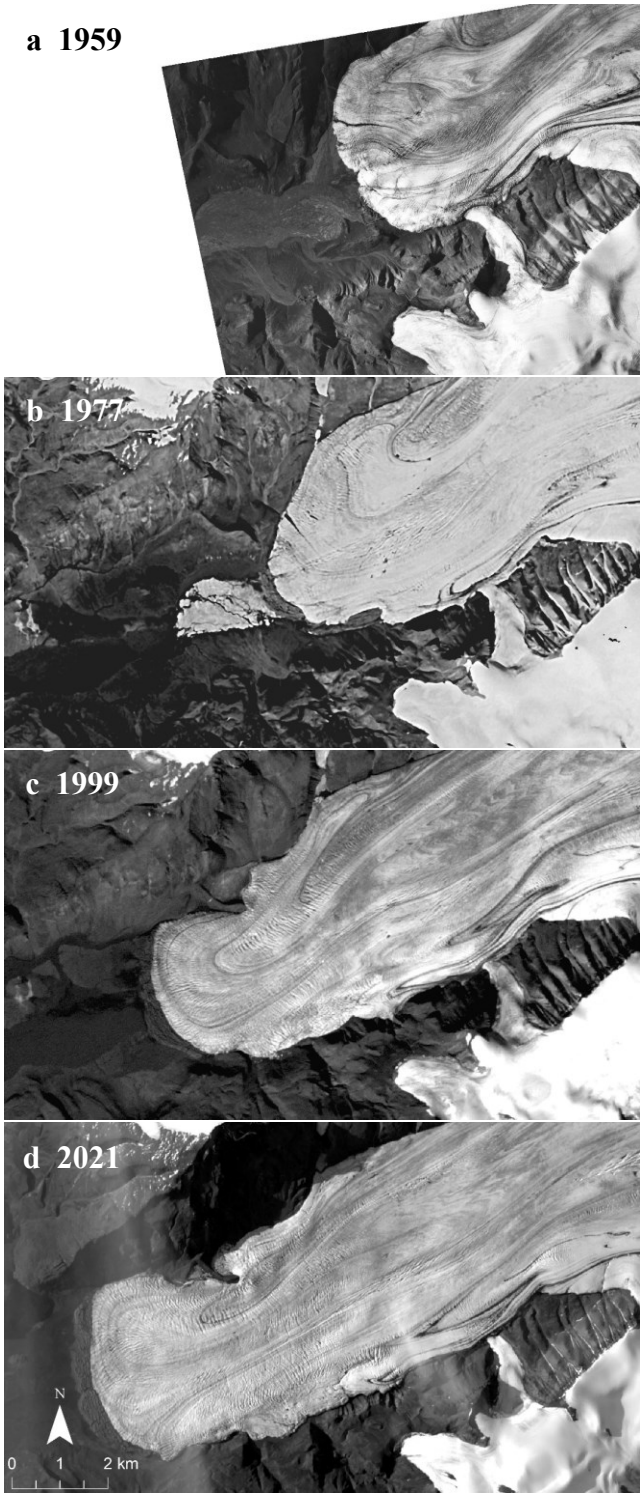

Figure 3.3. Progression of Airdrop Glacier's terminus advance throughout the study period. (a) Historical air photo taken on 28 July 1959 by the RCAF; (b) declassified KH-9 spy satellite photo from 13 July 1977 (note that the white region in front of the terminus is from aufeis, rather than glacier ice); (c) Landsat 7 image from 25 July 1999; (d) Landsat 8 scene from 15 August 2021. Each image shows the presence of ice-surface features indicative of possible surge activity such as looped moraines and moderately heavy crevassing.

3.4.2 Velocity patterns

Ice surface velocities derived from Landsat 1–8 optical satellite imagery and ERS-1/2 SAR data show that Airdrop Glacier did not undergo any rapid variations in flow speed since the 1970s. Instead, the glacier maintained a relatively fast centreline flow rate of over 100 m a^{-1} for most of the study period, reaching nearly 200 m a^{-1} in the early 2000s (Figure 3.4). In contrast, land-terminating glaciers in the CAA typically flow at speeds of 25 to 50 m a^{-1} across most of their length, and peak at <75 m a^{-1} near the terminus (Van Wychen et al., 2014). However, Airdrop has recently experienced a notable slowdown (Figure 3.4).

The glacier had a mean centreline velocity of 130 m a^{-1} during the period 1972–1981 over its lowermost ~10 km (Figure 3.4), albeit with a rather large uncertainty of 36.2 m a^{-1} (Table 3.2) resulting from the low spatial resolution of Landsat 1–3 imagery. Nevertheless, manual tracking of some matching features between image pairs yielded comparable velocities. The flow rate in the 1990s were similar with a mean centreline velocity of 144 m a^{-1} in 1992 and 138 m a^{-1} in 1997 within 12.5 km from the 2018 terminus position. The velocities peaked at >150 m a^{-1} at ~8 km from the 2018 terminus in 1992 and at ~7 km in 1997 (Figure 3.4). Subsequently, the scene pair velocities from 1999–2000 to 2005–2006 show that the glacier sustained a fast flow rate during the early 2000s, with average centreline speeds ranging from 141 to 153 m a^{-1} within ~7–19 km from the terminus. Airdrop's flow rate then dropped below 130 m a^{-1} in 2007 and has continued to decrease since, reaching an average centreline velocity of <70 m a^{-1} in 2020–2021, with the slowdown most pronounced over the lower parts of the glacier (Figure 3.4). From 2008 to 2020–2021, mean centreline velocities decreased by 51 m a^{-1} in the lowermost 10 km while they decreased by 23 m a^{-1} over a distance of 20–30 km from the 2018 terminus.

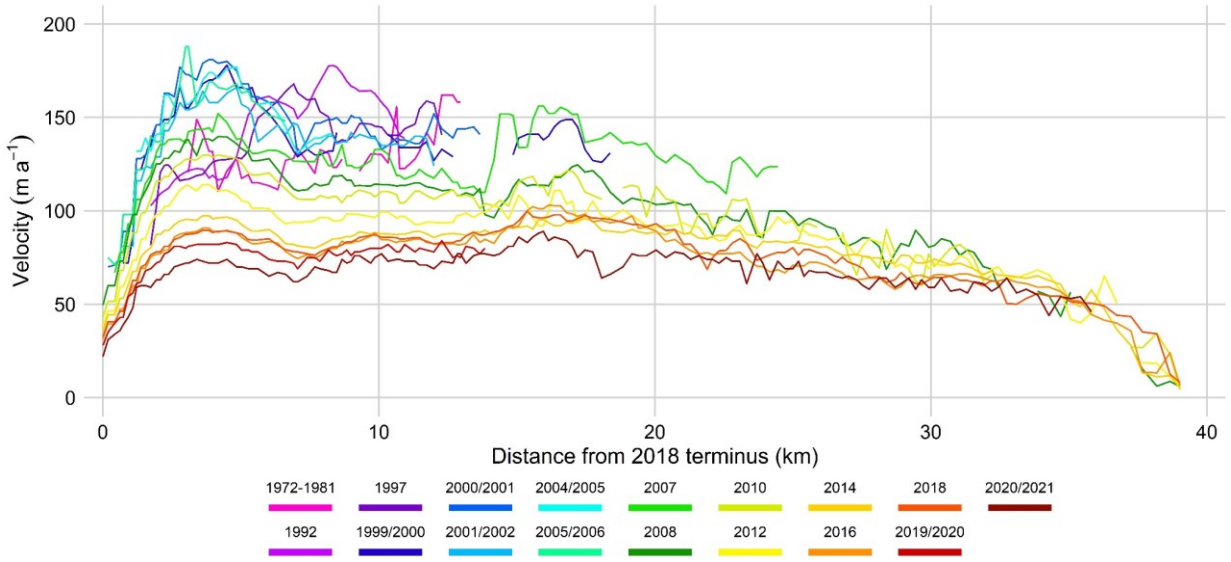

Figure 3.4. Centreline surface velocities from 1972 to 2021 for Airdrop Glacier. Velocities from 1972 to 1980 represent the mean of several annually separated early Landsat velocity scenes derived from feature-tracking. The velocity profiles prior to 1999 were extracted from Landsat 1–3, ERS-1/2, and NASA ITS_LIVE (Gardner et al., 2019) scene pairs, while all profiles since 1999 were derived from NASA ITS_LIVE scene pairs or annual mosaics.

3.4.3 Elevation changes

The continuous terminus advance and high velocities have been accompanied by considerable gains in surface elevation near the terminus of Airdrop Glacier (Figures 3.5; 3.6). Thickening occurred within 3–9.5 km of the 2018 terminus between 13 July 1977 and 20 May 2001 at an average rate of 3.2 ± 0.7 m a^{-1} and with a maximum single-cell value of 10 ± 0.7 m a^{-1}. Airdrop thickened at a similar rate of 3.1± 0.3 m a^{-1} over the period 20 May 2001 to 13 August 2021, but this was limited to within ~4.5 km of the 2018 terminus and peaked at a lower single-cell value of ~7 m a^{-1} ± 0.3 (Figures 3.5; 3.6). In total, these changes translate to a thickening of up to 250 ± 17 m between 1977 and 2001 and 140 ± 6 m from 2001 to 2021. These large elevation changes record the forward movement of large volumes of ice as the glacier advances over previously unglaciated terrain, as well as a redistribution of mass from the upper parts to the lower parts of Airdrop Glacier. Although no elevation data are available prior to

1977, we infer that a similar pattern would be observed from 1950–1977 since the glacier was also advancing during that period.

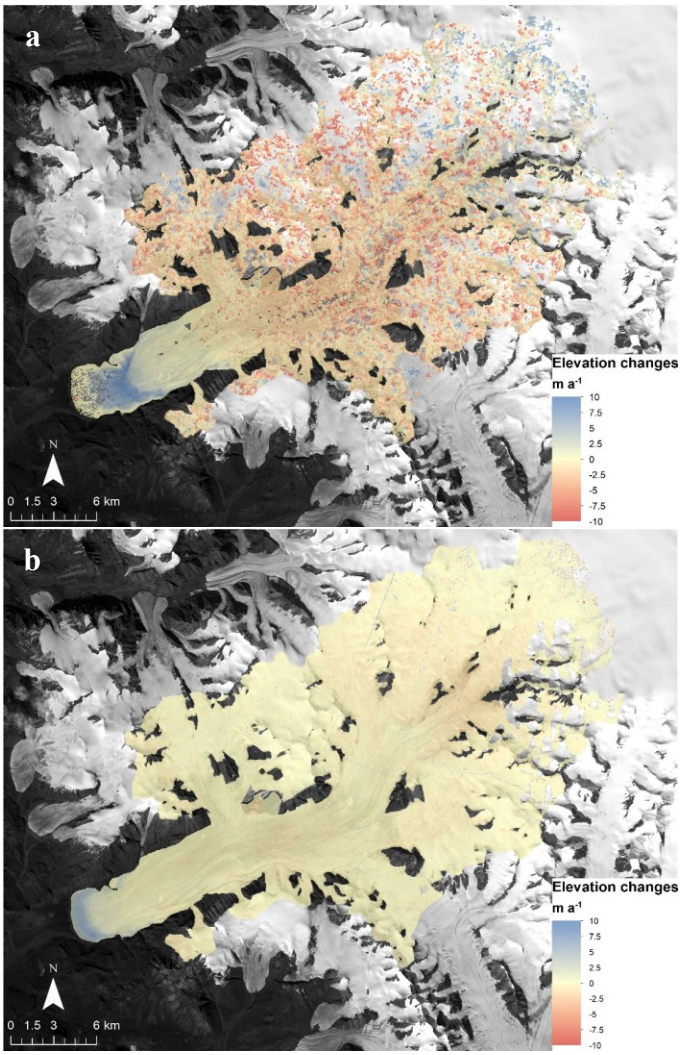

Figure 3.5. Airdrop Glacier surface elevation change trends for the periods (a) 1977–2001 and (b) 2001–2021. The 1977–2001 trends were computed by subtracting the 1977 DEM from the 2001 DEM, while the 2001–2021 trends were derived from multiple DEMs using the make_stack.py script from Shean et al. (2016). Base image: Landsat 8 composite image.

The remainder of the glacier encountered thinning at an average rate of -1.7 m a^{-1} ± 0.7 across the glacier's 10 m elevation bands upstream of 9.6 km from the 2018 terminus for 1977–2001 and -0.5 ± 0.3 m a^{-1} upstream of 4.4 km from the 2018 terminus for 2001–2021 (Figure 3.6). Speckling in the accumulation area in the 1977–2001 elevation difference results (Figure

3.5a) could be the result of feature matching issues in the KH-9 imagery in these high elevation and highly glaciated areas. Median uncertainties over nunataks in this region are ~1.4 m a^{-1}. The elevation trends computed for each 5-year period from 2001 to 2021 reveal constant thickening near the terminus across the glacier's elevation bands at median rates of up to ~14.6 ± 1.8 m a^{-1} in 2001–2006, ~10.3 ± 1.7 m a^{-1} in 2006–2011, ~6.4 ± 2.6 m a^{-1} in 2011–2016, and ~2.1 ± 2 m a^{-1} in 2016–2021. These results show a substantial decrease in the magnitude of the surface elevation changes that have occurred within Airdrop Glacier's terminus region since the beginning of the 21st century.

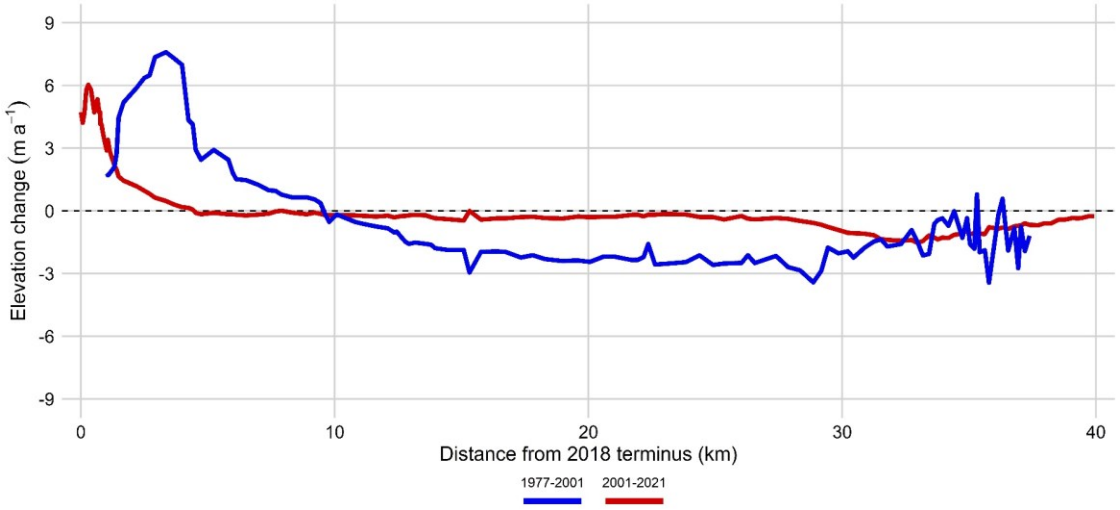

Figure 3.6. Median glacier surface elevation change trends observed in each 10 m hypsometric band for the periods 1977–2001 (blue) and 2001-2021 (red). The 1977–2001 trends were calculated from the differencing of the 1977 and 2001 DEMs while the 2001–2021 trends were derived from multiple DEMs using the make_stack.py script from Shean et al. (2016).

3.5 Discussion

Glaciers typically experience sustained changes in their terminus position as a response to either external forcing or the alteration of internal conditions, but can sometimes react to a combination of the two (e.g., Dunse et al., 2015; Sevestre et al., 2018; Benn et al. 2019b; Haga et al., 2020). The predominant external forcing is climate since temperature and precipitation are

the main controls on regional mass balance conditions (e.g., Noël et al., 2018), which, in turn, dictate whether a glacier is losing mass over time, making it susceptible to terminus retreat, or gaining mass and thus likely advancing. Internal ice flow instabilities, namely glacier surging, occur when a long period of low flow below the glacier's balance velocity is interrupted by a large and sudden increase in flow, typically by one or two orders of magnitude (Meier & Post, 1969). A marked advance of the terminus and a rapid redistribution of mass down glacier typically follows this large acceleration, causing significant elevation changes along the glacier surface. To assess the likely cause of the long-term advance of Airdrop Glacier we therefore consider whether changes in mass balance or surging can explain the observed changes of the glacier over the past ~70 years, and then compare the dynamics of Airdrop Glacier to other surge-type glaciers on Axel Heiberg Island.

3.5.1 Mass balance

In situ mass balance measurements in the Canadian High Arctic have been almost continuously negative since they began in 1959 (Koerner, 2005, Gardner et al., 2011; Thomson et al., 2017;), and recent studies have shown that the rate of mass loss has increased throughout the 21st century (Gardner et al., 2011; Lenaerts et al., 2013; Millan et al., 2017; Mortimer et al., 2018; Noël et al., 2018; Ciracì et al., 2020). For example, long term in situ mass balance measurements from White Glacier, located ~60 km south of Airdrop Glacier, has shown a negative glaciological balance of –213 ± 28 mm w.e. a^{-1} and a geodetic balance of –178 ± 16 mm w.e. a^{-1} for 1960–2014 (Thomson et al., 2017). Noël et al. (2018) used the regional climate model RACMO2.3 to reconstruct the daily surface mass balance (SMB) of glaciers in the CAA for the period 1958–2015. Their findings show that the northern CAA (NCAA; Ellesmere,

Devon, Axel Heiberg, and Meighen Islands) was subject to a negative mass budget of 11.9 ± 11.5 Gt a^{-1} for 1958–1995, and that the rate of mass loss more than doubled to a total of 28.2 ± 11.5 Gt a^{-1} for 1996–2015 (Noël et al., 2018). A more recent study by Ciracì et al. (2020) that used Gravitational Recovery and Climate Experiment (GRACE) and GRACE Follow-On data from April 2002 to September 2019 quantified an even higher mass loss of 41.2 ± 7 Gt a^{-1} for the NCAA. The recent increase in mass loss in the CAA is linked to an increase in runoff and longer melt seasons induced by rising summer air temperatures (Gardner et al., 2011; Lenaerts et al., 2013; Mortimer et al., 2018; Ciracì et al., 2020). Surface melt, which increases runoff, accounted for ~90% of the mass loss in the Queen Elizabeth Islands from 2005 to 2014, while the remaining ~10% was from ice discharge (Van Wychen et al., 2014). In comparison, ice discharge made up only 52% of the total mass loss from 1991 to 2002, when surface melt rates were lower (Millan et al., 2017).

This sustained mass loss has resulted in the retreat, slowdown, and thinning of most glaciers in the CAA, and most notably land-terminating glaciers (Thomson et al., 2011; Schaffer et al., 2017; Strozzi et al., 2017; Thomson et al., 2017; Thomson & Copland, 2018; Mortimer et al., 2018). In situ differential GPS measurements on White Glacier show a 31–38% slowdown at lower elevations (400 and 600 m a.s.l.) between 1960–1970 and 2012–2016, but no detectable changes in annual velocities at higher elevations (~850 m a.s.l.; Thomson & Copland, 2018). The observed slowdown has been associated with a decrease in internal ice deformation as a result of glacier thinning and a reduction in basal motion likely due to increased hydraulic efficiency (Flowers, 2015; Thomson & Copland, 2018), reducing basal water pressure and, in turn, increasing friction at the glacier bed (Iken & Bindschadler, 1986). SMB data compiled by Noël et al. (2018) reveal ice equivalent average losses over Airdrop of -0.37 ± 0.18 m a^{-1} for 1958–

1995 and 0.76 ± 0.18 m a^{-1} for 1996–2015 (https://doi.pangaea.de/10.1594/PANGAEA.881315), assuming an ice density of 850 ± 60 kg m^{-3} (Huss, 2013). Therefore, the negative mass balance regime in the region since at least 1958 cannot explain Airdrop Glacier's observed behaviour over the study period.

Studies have used numerical modelling to find relationships between glacier size, surface slope, elevation range, and mass balance gradient and the time it takes for an ice mass to respond to an external forcing, such as changes in climatic conditions (Bahr et al., 1998; Pfeffer et al., 1998; Raper & Braithwaite, 2009; Zekollari et al., 2020). Raper & Braithwaite (2009) showed that in cold climates glacier volume response time can increase with glacier area, with Axel Heiberg Island having the lowest mass balance sensitivity (i.e., temperature sensitivity of mass balance) of the seven regions that were studied. Their results also show that the response time of large glaciers on Axel Heiberg Island can be hundreds of years longer than small ice masses (Raper & Braithwaite, 2009). This is supported by the area change observations on Axel Heiberg of Thomson et al. (2011), who found that independent ice masses smaller than 25 km^2 experienced significant retreat or disappeared entirely between 1959 and 2000, while the considerably larger outlet glaciers from Müller and Steacie Ice Caps either advanced or retreated slightly. Some of the observed advance has been attributed to surge activity (Thomson et al., 2011). The island lost <1% (15.92 km^2) of its ice coverage during that period, although 90% of ice masses smaller than 0.2 km^2 completely disappeared. Despite the overall mass loss, eight large hydrological basins centered predominantly around Müller Ice Cap exhibited, on average, a ~5% increase in ice area and the greatest growth of 77.81 km^2 occurred in the Iceberg Bay basin (Thomson et al., 2011).

Variations in response time can also be illustrated by comparing the recent terminus changes of White, Thompson, and Good Friday glaciers. White Glacier has narrowed and retreated by approximately 250 m between 1948 and 1995 (Cogley et al., 1996b), and its area has decreased from 41.07 km^2 to 38.54 km^2 from 1960 to 2014 (Thomson & Copland, 2016; Thomson et al., 2017). Conversely, the terminus of Thompson Glacier, adjacent to White Glacier, advanced by about 950 m over the period 1948-1995, and has only started retreating sometime in the 2000s (Cogley et al., 1996b; Cogley et al., 2011). A possible explanation for the contrasting behaviour of these two neighbouring glaciers is that Thompson Glacier, being an order of magnitude larger than White Glacier (384 km^2 versus 39.4 km^2), has a longer response time (Cogley et al., 2011). Therefore, Thompson Glacier's prolonged advance in comparison to White Glacier could have been the result of a delayed response to the positive mass balance conditions that prevailed during the LIA cooling (Cogley et al., 2011).

The uninterrupted advance of Good Friday Glacier since the late 1940s has also been interpreted by Medrzycka et al. (2019) to be potentially related to the positive mass balance conditions of the LIA, suggesting that its advance could perhaps be explained as a continuing response to this environmental forcing due to its large basin size of ~800 km^2 and hence its longer response time than both White and Thompson glaciers. Considering Airdrop's similar basin size (~600 km^2) and behaviour, we propose that a delayed response to the LIA is one of the likely explanations for the glacier's advance over the last seven decades.

3.5.2 Glacier surging

A dynamic instability, particularly glacier surging, offers an alternative explanation for the observed dynamics of Airdrop Glacier. Surges are thought to arise when balances in both

enthalpy and mass flux are not met, preventing the glacier from remaining in a stable steady state by periodically increasing mass flux to evacuate the buildup of excess enthalpy at the glacier bed (Sevestre & Benn, 2015; Benn et al., 2019a). Enthalpy production is driven predominantly by internal factors, including the conduction of heat from the glacier bed to the atmosphere and the runoff of basal meltwater, but can also be affected by external factors, such as the intrusion of summer surface melt to the glacier bed through crevasses and moulins, causing a hydro-thermodynamic feedback (Dunse et al., 2018; Benn et al., 2019a).

In cold, dry environments such as the CAA where glacier velocities are typically low and thus basal enthalpy production is minimal, surge-type glaciers tend to be large and thick. This is because larger glaciers have higher basal enthalpy production from higher balance velocities, coupled with less efficient enthalpy dissipation from conductive heat losses to the atmosphere due to the greater ice thickness, making them less likely to find a balance between enthalpy production and enthalpy loss (Sevestre & Benn, 2015). In fact, the largest surge-type glaciers of all surge clusters worldwide are found in the Canadian Arctic, with an average area of 627 km^2 (Sevestre & Benn, 2015). Copland et al. (2003) and Sevestre & Benn (2015) have identified a total of 51 and 54 surge-type glaciers in the Canadian Arctic with remote sensing and modelling, respectively, but more recent studies have found additional surge-type glaciers (e.g., Van Wychen et al., 2016; Van Wychen et al., 2022).

A number of surface features, such as looped medial moraines, intense folding visible at the surface, extensive crevassing, and a heavily broken up surface can be detected using aerial photography or satellite imagery and can provide indication of possible surging activity (Copland et al., 2003). Copland et al. (2003) identified Airdrop Glacier as a surge-type glacier and inferred that the glacier was actively surging in 1999 based on the presence of heavy crevassing, surface

folding and looping, and the ~4.5 km terminus advance that occurred between 1959 and 1999. We have observed the same surface features diagnostic of surging throughout the entire study period (Figure 3.3). Other characteristics suggestive of a surge include high surface velocities over nearly the entire length of the glacier, thickening in Airdrop's lowermost ~4–8 km and thinning over the rest of its surface, as well as a recent slowdown that was interpreted as a long transition into quiescence occurring over time periods of a decade or more (Van Wychen et al., 2021).

Previous studies have proposed that Airdrop Glacier began surging sometime between 1975 and 1999 (Thomson et al., 2011), and that it was still actively surging in the mid 2000s before it started slowing down (Van Wychen et al., 2021). Our results suggest that surge initiation occurred prior to 1975 and could have instead taken place in the late 1950s or early 1960s as the glacier's terminus advance rate notably increased following its near stagnation in the 1950s. Nevertheless, the scarcity of imagery prior to 1972 impedes our ability to precisely determine when the glacier would have started surging, and the earliest available aerial photograph from 1950 was oblique, making it challenging to accurately determine its position relative to the next photo in 1959. In addition, Airdrop's flow rate for 1972–2021 has generally varied little, other than the constant slowdown that has occurred since the mid 2000s (Figure 3.4), and surface elevation change patterns show a long-term pattern of thickening near the terminus and thinning across the rest of the glacier since at least 1977 (Figure 3.5; Figure 3.6). Although surge cycles are hypothesised to attain up to 500 years in Svalbard (Dowdeswell et al., 1991), the longest active phase ever recorded of 50+ years has been observed on Split Lake Glacier, in the Canadian Arctic. Therefore, if Airdrop Glacier is indeed surging and was already

surging in the 1950s, the glacier would have a similar, or even greater, active phase length of more than 70 years.

3.5.3 Distinguishing between surging and advancing glaciers

A case study of two adjacent glaciers in the eastern Karakoram by Lv et al. (2020) used optical satellite imagery to construct a simple classification to distinguish surging glaciers from advancing glaciers. Their results showed three major differences between the two types: 1) advancing glaciers move forward at a steady rate, while surging glaciers advance dramatically upon surge initiation; 2) surging glaciers undergo significant fluctuations in surface velocity throughout their active phase, while advancing glaciers flow at a steady rate; 3) surface elevation changes indicate a redistribution of mass from the reservoir zone to the receiving zone for surging glaciers, but advancing glaciers seem to only thicken over their terminus part (Lv et al., 2020). Based on this classification, our observations reveal that Airdrop has behaved most similarly to characteristics of an advancing glacier, as there were no significant fluctuations in Airdrop Glacier's advance and flow rates over the study period other than the persistent slowdown that has occurred over the last ~15 years (Table 3.3; Figure 3.4), and the only evident elevation increase for 1977–2021 from geodetic mass balance data occurred near the terminus (Figure 3.5; Figure 3.6).

Unlike Airdrop Glacier, which has had an overall negative mass balance for several decades (Koerner, 2005; Gardner et al., 2011; Lenaerts et al., 2013; Millan et al., 2017; Mortimer et al., 2018; Noël et al., 2018; Ciracì et al., 2020), the advancing glacier studied by Lv et al. (2020) had a slightly positive mass balance of 270 ± 40 mm w.e. a^{-1} from 1995 to 2019, which could explain why it had not started decelerating like Airdrop. While the geodetic mass balance

values are greatest near the terminus and lowest in Airdrop's upper part, the SMB predicted from modelling (Noël et al., 2018) becomes more positive up-glacier from an ice equivalency of ~-2 m a^{-1} near the terminus to ~0.2 m a^{-1} at >40 km from the 2018 terminus as elevation increases. This suggests that the observed surface elevation changes cannot be attributed to SMB. The glacier's dynamic balance for 2001–2021, which was computed by subtracting the surface mass balance from the geodetic mass balance at 1 km spatial resolution, shows a redistribution of mass down-glacier from Airdrop's upper part, with thinning rates exceeding -1.5 m a^{-1} above ~30 km from the 2018 terminus. The glacier surface was, according to the dynamic balance from 2001 to 2021, predominantly subject to thickening up to ~28 km from the 2018 terminus. The magnitude of this thickening increased in a down-glacier direction, with typical rates of >1 m a^{-1} below ~13 km from the 2018 terminus and reaching >5 m a^{-1} near the terminus. These dynamic balance trends are in line with surging behaviour during the active phase, where mass is transferred down-glacier from the upper reservoir zone to the lower receiving zone. However, it is unclear whether the observed surface elevation changes could simply be the result of the sustained high velocities over the entire glacier length if the glacier is still responding to the climatic forcing of the LIA, resulting in a high emergence velocity in the ablation area. In that case, the recent deceleration of Airdrop, which has occurred in parallel with a reduction of its advance rate and thickening rate near the terminus, would constitute a gradual transition towards the glacier's balance velocity under the current environmental conditions rather than a transition to the quiescent phase. If this slowdown persists, Airdrop could soon start retreating akin to what has recently happened to nearby Thompson and White glaciers (Cogley et al., 1996; Cogley et al., 2011; Thomson et al., 2011).

3.5.4 Evidence for a slow surge

If Airdrop is defined as surge-type, then its long active phase would be best fitted under the category of a slow surge (Jiskoot, 2011). Unlike typical surging glaciers, which usually undergo an increase in velocity of two or three orders of magnitude (Meier & Post, 1969), slowly surging glaciers have flow rates 5–10 times higher than during the quiescent phase (Jiskoot, 2011). Slow surges also tend to be longer, with an active phase duration of more than 20 years, and sometimes result in no change in terminus position (Jiskoot, 2011). Slowly surging glaciers have been observed in a few regions with differing climatic conditions such as Yukon, Svalbard, and the Canadian Arctic (Frappé & Clarke, 2007; Sund et al., 2009; Flowers et al., 2011; Van Wychen et al., 2022). Flow speeds during a slow surge can be much lower than during an ordinary surge as exemplified by the ~20-year surge of Trapridge Glacier in the St. Elias Mountains, Yukon, which saw only a slight acceleration from 16 m a^{-1} to 42 m a^{-1}, but still experienced a ~450 m advance (Frappé & Clarke, 2007). The only slowly surging glacier that has been previously described in the CAA is a land-terminating glacier called Split Lake Glacier (437.8 km^2), on SE Ellesmere Island, which has been advancing since ~1970 at flow rates that reach >600 m a^{-1} (Van Wychen et al., in press). Large variations in Split Lake Glacier's ice motion were recorded around 1970 when the glacier started surging and between 1999 and 2002 when the glacier underwent a temporary slowdown (Van Wychen et al., 2022). In contrast, Airdrop Glacier has not experienced any rapid changes in velocity typical of surge-type glaciers since at least the 1970s, yet the lack of early imagery means that the initiation phase is not well defined. Although its dynamics closely resemble the behaviour of slowly surging glaciers, the lack of evidence in the available datasets of a clear surge initiation or of any other periodic

oscillations in ice motion outside of the study period makes it difficult to determine whether the current advance is driven by a slow surge.

3.5.5 Comparison to other surge-type glaciers on Axel Heiberg Island

A total of three glaciers on Axel Heiberg Island (Airdrop: ~600 km^2, Good Friday: ~800 km^2, and Iceberg: ~1000 km^2) have been previously classified as surge-type and constitute the island's three largest outlet glaciers (Müller, 1969; Copland et al., 2003). The presence of large looped moraines, heavy crevassing, extensive surface folding and looping, and significant advances of ~4.5–7 km between 1959 and 1999 was used to infer that all three glaciers were surging in the 1990s (Copland et al., 2003). These glaciers alone added 85.45 km^2 of ice to the island's glacier inventory between 1959 and 2000 (Thomson et al., 2011).

Iceberg Glacier is the only ice mass on Axel Heiberg Island that has shown a cyclic behaviour that is typical for surge-type glaciers since it has now been observed in both the active and quiescent phases of the surge cycle (Copland et al., 2003; Van Wychen et al., 2016; Medrzycka et al., 2019; Chapter 2). Iceberg's surge lasted from approximately 1981 to 2003, with a rapid rise in ice motion at surge initiation and velocities attaining >2000 m a^{-1} at the terminus in summer 1991, more than an order of magnitude higher than the highest velocity on record for Airdrop Glacier. Surface elevation change trends reveal that the glacier gains mass in its reservoir zone and loses mass in its receiving zone during quiescence, while the opposite occurs during a surge. The major difference between the two glaciers is that Airdrop has only encountered relatively small fluctuations in its patterns and rates of terminus change, flow, and ice thickness, while Iceberg experienced dramatic changes in its dynamics over the same period as the glacier underwent an entire surge cycle. For example, Iceberg Glacier accelerated by a

factor of >50 in parts of its terminus region in 1981 compared to its 1972–1980 average velocity, while the glacier's flow rate decreased by a factor of three in less than a year in 1999/2000 as the glacier was nearing surge termination (Chapter 2). In comparison, Airdrop Glacier took 15 years to slow down by a factor of ~2.3 within 7 km of its 2018 terminus position. It is perplexing as to why two adjacent glaciers would behave in such different manners, but perhaps the tidewater dynamics at Iceberg Glacier's front could play a role in regulating velocities since the flow of such glaciers are controlled by a number of additional mechanisms occurring at the ice/ocean interface (Nick et al., 2009).

In contrast, Good Friday Glacier's overall dynamics resemble Airdrop's much more than Iceberg's despite it being marine-terminating for the majority of the last 50 years (Medrzycka et al., 2019). The main difference between the two glaciers is that velocities are currently highest at Good Friday's terminus (Medrzycka et al., 2019), while velocities at Airdrop's terminus sharply decrease. These are typical velocity patterns for marine-terminating and land-terminating glaciers in the CAA (Van Wychen et al., 2021). The glacier has advanced by ~9.3 km since observations began in 1948 and has maintained relatively high velocities of >100 m a^{-1} across most of its length (Medrzycka et al., 2019). Similarly to Airdrop, Good Friday Glacier has slowed down by ~50–100 m a^{-1} over much of its length throughout the last decade accompanied by a considerable decrease in the glacier's rate of advance in the last few years (Medrzycka et al., 2019). Medrzycka et al. (2019) suggested surging and a delayed response to the positive mass balance regime of the LIA as possible causes for the observed dynamics, but also suggested an alternate explanation stating that the glacier terminus could have experienced a single period of unstable advance resulting from perturbations in bedrock topography. There are no available

data concerning Airdrop Glacier's underlying topography, so this hypothesis cannot be tested in this study.

With the lack of clear evidence of a surge initiation or surge termination, it remains unclear as to whether the observed dynamics of Airdrop and Good Friday Glaciers are related to surging. If they are indeed surging, then the available evidence suggests that they would be best categorized as slowly surging, similar to Split Lake Glacier (Van Wychen et al., 2022). Although the recent slowdown of both Airdrop and Good Friday has previously been interpreted as a gradual shift into quiescence (Medrzycka et al., 2019; Van Wychen et al., 2021), the nearly simultaneous decrease in the flow rates for two similarly sized glaciers raises the alternate explanation that the glaciers could be starting to adjust to the negative mass balance conditions of the last several decades following positive mass balance conditions of the LIA.

3.6 Conclusions

The observations in this study indicate that Airdrop Glacier has undergone a continuous advance of ~6 km since the 1950s, related to sustained high centreline velocities of >100 m a^{-1} during most of the study period. This has resulted in a drawdown of mass and pronounced thickening over the glacier's terminus region, causing surface elevation changes that are significantly different to those predicted from SMB modelling (Noël et al., 2018). These patterns markedly contrast with the dominant regional trend of glacier retreat, slowdown, and thinning over the past several decades in the CAA in response increasingly negative mass balance conditions (Gardner et al., 2011; Thomson et al., 2011; Lenaerts et al., 2013; Millan et al., 2017; Schaffer et al., 2017; Strozzi et al., 2017; Thomson et al., 2017; Thomson & Copland, 2018; Mortimer et al., 2018; Noël et al., 2018; Ciracì et al., 2020).

The glacier's dynamics paired with the presence of surface features indicative of surging, such as heavy crevassing and extensive folding and looping of moraines, suggest that the observed advance could have resulted from a surge. The progressive slow down of >50 m a^{-1} that has occurred over the last ~15 years could then be interpreted as the glacier transitioning to the quiescent phase of the surge cycle. If the glacier is indeed surging, the active phase that potentially spans more than seven decades, and the relatively low velocities compared to other nearby surge-type glaciers (e.g., Iceberg Glacier; Chapter 2), would be best aligned with the definition of a slow surge (Jiskoot, 2011). The seeming acceleration in the rate of terminus advance in the 1960s and 1970s compared to the 1950s could possibly indicate the onset of a surge, but the sparsity of imagery between 1950 and 1972, and the change in terminus width as it passed a bedrock constriction, makes it difficult to know precisely how and why the glacier was changing prior to the satellite era. The observed surface features, terminus advance, high ice velocities, and surface elevation change trends do not in themselves provide conclusive evidence of surging or any other dynamic instability. The lack of evidence of periodic oscillations in velocities or any previous fast flow events prevents us from deducing that the glacier's behaviour over the last 70 years is cyclic in nature.

An alternate explanation for Airdrop's discrepant behaviour with similar glaciers in the CAA, and with recent climatic conditions, is its long response time to external forcing. Previous studies have found a relationship between a glacier's size and its response time (Bahr et al., 1998; Pfeffer et al., 1998; Raper & Braithwaite, 2009; Zekollari et al., 2020), which is reflected on Axel Heiberg Island by the asynchronous start of terminus retreat between glaciers of different sizes following the persistent negative mass balance conditions of the last several decades (Cogley et al., 1996; Cogley et al., 2011). This out of sync behaviour between adjacent

glaciers has been interpreted as being potentially linked to variations in response times to the climatic conditions of the LIA, which favoured a positive mass balance regime (Cogley et al., 2011; Medrzycka et al., 2019). Considering that Thompson Glacier (384 km^2) kept advancing until the 2000s (Cogley et al., 2011), Airdrop Glacier could still be responding to the LIA cooling considering its longer response time owing to its larger size (~600 km^2). Airdrop and Good Friday (~800 km^2) experienced a nearly synchronous decrease in their flow and advance rates over the last ~10–15 years, which could indicate that these two glaciers are starting to respond to the negative mass balance conditions that have prevailed throughout the ~70-year study period.

Future investigations should keep track of Airdrop's velocities to determine whether its ongoing slowdown stabilises to the typical flow rates for land-terminating glaciers in the Canadian Arctic of 20–50 m a^{-1} along the trunk and <75 m a^{-1} near the terminus (Van Wychen et al., 2014), or drop below the glacier's balance velocity to stagnant levels (i.e., <20 m a^{-1}). Testing the enthalpy balance theory of surging proposed by Benn et al. (2019) could verify whether their model can predict the glacier's observed sequence of events and could provide insights into why adjacent Iceberg Glacier's surge dynamics greatly differs from Airdrop's, although better definition of boundary conditions, such as ice thickness and internal thermal conditions, would be needed for this.

Our findings highlight the complex behaviour and dynamics of glaciers in the Canadian Arctic and emphasise the fact that not all glaciers respond in the same way to external forcing. Comprehensive studies of glacier surging in the Canadian Arctic, which has been scarcely analysed, along with additional research on the role of long-term mass balance trends in driving glacier dynamics could help identify the range of factors causing the observed variety of glacier

dynamic behaviour and improve our understanding of how these dynamics might evolve in a changing climate.

Chapter 4: Conclusion

4.1 Summary

Although glacier surging has been thoroughly examined in other regions, surge-type glaciers in the Canadian Arctic have only been analysed in relatively few studies (e.g., Hattersley-Smith, 1964, 1969; Müller, 1969; Copland et al., 2003; Short & Gray, 2005; Medrzycka et al., 2019; Van Wychen et al., 2021, 2022), and observations throughout an entire surge cycle are lacking. This thesis provides a detailed reconstruction from the 1950s to present of the surge history and dynamics of two adjacent glaciers located on western Axel Heiberg Island with profoundly contrasting behaviours. This work has used a wide range of imagery to quantify changes in terminus position, along with ice surface flow and elevation. Airdrop Glacier, a land-terminating outlet of Müller Ice Cap, has shown a consistent advance during the study period with no clear sign of any cyclic behaviour, while Iceberg Glacier, a large marine-terminating outlet of Müller Ice Cap, has experienced substantial fluctuations in its dynamics as the glacier underwent a complete surge cycle.

Airdrop Glacier has advanced continuously for a total of ~6 km since the 1950s, while Iceberg Glacier experienced a >7 km advance in just 17 years (1980–1997), but retreated at a relatively fast rate since then. Similarly, Airdrop's flow rate has seen minimal fluctuations since 1972 besides a gradual decrease over the last ~15 years, while Iceberg Glacier's fastest recorded ice flow in summer 1991 was >200 times higher than the glacier's current average centreline velocity. These dynamics are also reflected within the glaciers' surface morphologic variations, with Airdrop having continuously thickened near its terminus at an average rate of ~3 m a^{-1} since at least 1977 and thinned throughout the remaining of its surface and Iceberg experiencing a

large transfer of mass from the reservoir zone to the receiving zone during its surge, resulting in average absolute elevation changes over the entire surface of 2 ± 1 m a^{-1} during the active phase and $\sim 0.9 \pm 0.4$ m a^{-1} during the current quiescent phase.

While Airdrop's relatively high velocities were sustained until recently, the apparent drawdown of mass to lower elevations and the large terminus advance could signify that the glacier has been undergoing a slow surge with a possible initiation in the 1950s or 1960s. Alternatively, the advance could have been driven by the glacier's long response time to the LIA cooling, which resulted in positive mass balance conditions. Medrzycka et al. (2019) also suggested this as a possible explanation for Good Friday Glacier's ~9 km advance over the last seven decades, and its near synchronous slowdown with Airdrop Glacier since the mid-2000s could be indicative of the two ice masses starting to respond to the negative mass balance conditions of the last several decades.

On the other hand, our observations confirm Iceberg Glacier's surge-type classification, and the available evidence suggests that the glacier surged for ~22 years from approximately 1981 to 2003. We propose that a combination of the following mechanisms likely contributed to surge initiation: internal thermodynamic processes driven by a steepening of the glacier surface during quiescence, a retreat of a large portion of the terminus from a pinning point into deep fiord waters (resulting in accelerated retreat and thinning rates until flotation was likely reached in the 1970s), and the removal of the sea ice's buttressing force as it completely retreated from the ice front in August 1981. The surge appears to have initiated at the terminus and spread up-glacier, perhaps through the formation and upward migration of a crevasse field (Sevestre et al., 2018), bringing meltwater to the glacier bed and initiating sliding. The surge resulted in significant ice flow acceleration, with velocities as high as ~2300 m a^{-1} at the terminus in

summer 1991, an abrupt terminus advance, and a large drawdown of mass. Following surge initiation in ~2003, the glacier decelerated to stagnant velocities over the entire trunk, and started building up mass again in its upper reservoir zone and losing mass in its lower receiving zone through SMB, and has retreated by more than 2.5 km.

Iceberg and Airdrop glacier's dynamics throughout the study period do not reflect the sustained negative mass balance conditions that have existed over the region throughout the last several decades, which have resulted in extensive terminus retreat, decelerating ice flow, and glacier thinning (Schaffer et al., 2017; Strozzi et al., 2017; Thomson et al., 2017; Thomson & Copland, 2018; Mortimer et al., 2018). In fact, the long-term geodetic mass balance of Iceberg Glacier has been continuously negative at ~0.14–0.15 km^3 a^{-1} despite the switch between quiescent and active phases over the study period. The contrasting behaviour of these two glaciers shown by this thesis highlight the complex dynamics of glaciers in the Canadian Arctic and how ice masses respond differently to external forcing. In this study, we have provided observations throughout an entire surge cycle for the first time in the Canadian Arctic and have revealed the anomalous advance, velocities, and elevation changes of Airdrop Glacier, which was previously believed to be subject to normal surging behaviour. This thesis also offers important insights into the mechanisms that regulate surging in the region, which need to be better understood to determine how glacier surging in the Canadian Arctic may continue to evolve in a warming climate.

4.2 Future work

Future studies should continue to monitor Airdrop Glacier's recent slowdown to determine whether velocities stabilise to a typical low flow rate of land-terminating glaciers in

this region. This would indicate that the glacier is close to equilibrium with present-day climate and that the observed advance over the last seven decades would more likely be attributed to a delayed response to the LIA cooling rather than surging activity.

The significantly higher spatial and temporal resolutions offered by recent satellite imagery in comparison to early Landsat imagery allows for the close examination of recent and future surges with a level of detail that could not be obtained beforehand. This provides the opportunity to carry out thorough analyses of surging in the Canadian Arctic and to test the applicability of the enthalpy balance theory of surging in different contexts. Testing this model throughout the Canadian Arctic could provide insights into which factors underlie the variety of glacier surge dynamics observed within this region, help differentiate between stable and unstable glacier behaviours, potentially establish what causes some glaciers to have dynamics that are out of sync with other ice masses in the same region, and help understand whether associated surge frequency and intensity is changing over time. In fact, climate change could bring the Canadian Arctic within the optimal climatic envelope for surging defined by Sevestre & Benn (2015), which would potentially make glaciers in this region more prone to surging. An increase in surging activity in the Canadian Arctic would result in periodic increases in iceberg discharge to the ocean, which could pose a risk to ships and increase the region's contribution to sea level rise. A thorough understanding of the factors triggering these velocity fluctuations is also necessary to help constrain global sea level rise projections and to provide insight into the mechanics of other unstable glacier changes, such as the collapse of ice streams and ice shelves.

References

Aðalgeirsdóttir, G., Björnsson, H., Pálsson, F., & Magnússon, E. (2005). Analyses of a surging outlet glacier of Vatnajökull ice cap, Iceland. *Annals of Glaciology*, *42*, 23-28.

Aschwanden, A., Bueler, E., Khroulev, C., & Blatter, H. (2012). An enthalpy formulation for glaciers and ice sheets. *Journal of Glaciology*, 58(209), 441-457.

Bahr, D. B., Pfeffer, W. T., Sassolas, C., & Meier, M. F. (1998). Response time of glaciers as a function of size and mass balance: 1. Theory. *Journal of Geophysical Research: Solid Earth*, *103*(B5), 9777-9782.

Barrand, N. E., & Murray, T. (2006). Multivariate controls on the incidence of glacier surging in the Karakoram Himalaya. *Arctic, Antarctic, and Alpine Research*, 38(4), 489-498.

Benn, D. I., Fowler, A. C., Hewitt, I., & Sevestre, H. (2019a). A general theory of glacier surges. *Journal of Glaciology*, 65(253), 701-716.

Benn, D. I., Jones, R. L., Luckman, A., Fürst, J. J., Hewitt, I., & Sommer, C. (2019b). Mass and enthalpy budget evolution during the surge of a polythermal glacier: a test of theory. *Journal of Glaciology*, 65(253), 717-73S1.

Björnsson, H., Pálsson, F., Sigurđsson, O., & Flowers, G. E. (2003). Surges of glaciers in Iceland. *Annals of glaciology*, 36, 82-90.

Box, J. E., Colgan, W. T., Wouters, B., Burgess, D. O., O'Neel, S., Thomson, L. I., & Mernild, S. H. (2018). Global sea-level contribution from Arctic land ice: 1971-2017. *Environmental Research Letters*, 13(12), 125012.

Ciracì, E., Velicogna, I., & Swenson, S. (2020). Continuity of the mass loss of the world's glaciers and ice caps from the GRACE and GRACE Follow-On missions. *Geophysical Research Letters*, 47(9), e2019GL086926.

Clarke, G. K. (1976). Thermal regulation of glacier surging. *Journal of Glaciology*, 16(74), 231-250.

Clarke, G. K., Schmok, J. P., Ommanney, C. S. L., & Collins, S. G. (1986). Characteristics of surge-type glaciers. *Journal of Geophysical Research: Solid Earth*, 91(B7), 7165-7180.

Clarke, G. K. (1991) Length, width and slope influences on glacier surging. *Journal of Glaciology*, 37(126), 236–246.

Copland, L., Sharp, M. and Dowdeswell, J. (2003): The distribution and flow characteristics of surge-type glaciers in the Canadian High Arctic. *Annals of Glaciology*, 36, 73-81.

Cogley, J. G., Adams, W. P., Ecclestone, M. A., Jung-Rothenhäusler, F., & Ommanney, C. S. L. (1996a). Mass balance of white glacier, Axel Heiberg Island, NWT, Canada, 1960–91. *Journal of Glaciology*, 42(142), 548-563.

Cogley, J. G., Ecclestone, M. A., & Adams, W. P. (1996b). Fluctuations of the terminuses of White and Thompson Glaciers, Axel Heiberg Island, NWT, Canada. In *Eastern Snow Conference Proceedings* (Vol. 53, pp. 83-94).

Cogley, J. G., Adams, W. P., & Ecclestone, M. A. (2011). Half a century of measurements of glaciers on Axel Heiberg Island, Nunavut, Canada. *Arctic*, 371-375.

Debella-Gilo, M., & Kääb, A. (2011). Sub-pixel precision image matching for measuring surface displacements on mass movements using normalized cross-correlation. *Remote Sensing of Environment*, *115*(1), 130-142.

Dolgoushin, L. D., & Osipova, G. B. (1975). Glacier surges and the problem of their forecasting. *IAHS Publ*, 104, 292-304.

Dowdeswell, J. A., Hamilton, G. S., & Hagen, J. O. (1991). The duration of the active phase on surge-type glaciers: contrasts between Svalbard and other regions. *Journal of Glaciology*, 37(127), 388-400.

Dowdeswell, J. A., Hodgkins, R., Nuttall, A. M., Hagen, J. O., & Hamilton, G. S. (1995). Mass balance change as a control on the frequency and occurrence of glacier surges in Svalbard, Norwegian High Arctic. *Geophysical Research Letters*, 22(21), 2909-2912.

Dowdeswell, J. A., & Benham, T. J. (2003). A surge of Perseibreen, Svalbard, examined using aerial photography and ASTER high resolution satellite imagery. *Polar research*, *22*(2), 373-383.

Dunse, T., Schellenberger, T., Hagen, J. O., Kääb, A., Schuler, T. V., & Reijmer, C. H. (2015). Glacier-surge mechanisms promoted by a hydro-thermodynamic feedback to summer melt. *The Cryosphere*, *9*(1), 197-215.

Flink, A. E., Noormets, R., Kirchner, N., Benn, D. I., Luckman, A., & Lovell, H. (2015). The evolution of a submarine landform record following recent and multiple surges of Tunabreen glacier, Svalbard. *Quaternary Science Reviews*, *108*, 37-50.

Flowers, G. E., Roux, N., Pimentel, S., & Schoof, C. G. (2011). Present dynamics and future prognosis of a slowly surging glacier. *The Cryosphere*, *5*(1), 299-313.

Flowers, G. E. (2015). Modelling water flow under glaciers and ice sheets. *Proceedings of the Royal Society A: Mathematical, Physical and Engineering Sciences*, *471*(2176), 20140907.

Frappé, T. P., & Clarke, G. K. (2007). Slow surge of Trapridge Glacier, Yukon Territory, Canada. *Journal of Geophysical Research: Earth Surface*, *112*(F3).

Gardelle, J., Berthier, E., Arnaud, Y., & Kääb, A. (2013). Region-wide glacier mass balances over the Pamir-Karakoram-Himalaya during 1999–2011. *The Cryosphere*, *7*(4), 1263-1286.

Gardner, A. S., Moholdt, G., Wouters, B., Wolken, G. J., Burgess, D. O., Sharp, M. J., ... & Labine, C. (2011). Sharply increased mass loss from glaciers and ice caps in the Canadian Arctic Archipelago. *Nature*, *473*(7347), 357-360.

Gardner, A. S., Moholdt, G., Scambos, T., Fahnstock, M., Ligtenberg, S., Van Den Broeke, M., & Nilsson, J. (2018). Increased West Antarctic and unchanged East Antarctic ice discharge over the last 7 years. *The Cryosphere*, *12*(2), 521-547.

Gardner, A. S., Fahnestock, M. A., & Scambos, T. A. (2019). ITS_LIVE Regional Glacier and Ice Sheet Surface Velocities. *Data archived at National Snow and Ice Data Center*.

Girod, L., Nuth, C., Kääb, A., McNabb, R., & Galland, O. (2017). MMASTER: improved ASTER DEMs for elevation change monitoring. *Remote Sensing*, *9*(7), 704.

Gudmundsson, G. H. (1999). A three-dimensional numerical model of the confluence area of Unteraargletscher, Bernese Alps, Switzerland. *Journal of Glaciology*, *45*(150), 219-230.

Grant, K. L., Stokes, C. R., & Evans, I. S. (2009). Identification and characteristics of surge-type glaciers on Novaya Zemlya, Russian Arctic. *Journal of Glaciology*, 55(194), 960-972.

Haga, O. N., McNabb, R., Nuth, C., Altena, B., Schellenberger, T., & Kääb, A. (2020). From high friction zone to frontal collapse: dynamics of an ongoing tidewater glacier surge, Negribreen, Svalbard. *Journal of Glaciology*, 66(259), 742-754.

Harcourt, W. D., Palmer, S. J., Mansell, D. T., Le Brocq, A., Bartlett, O., Gourmelen, N., ... & Young, D. A. (2020). Subglacial controls on dynamic thinning at Trinity-Wykeham Glacier, Prince of Wales Ice Field, Canadian Arctic. *International Journal of Remote Sensing*, 41(3), 1191-1213.

Hattersley-Smith, G. (1964). Rapid advance of glacier in northern Ellesmere Island. *Nature*, *201*(4915), 176-176.

Hattersley-Smith, G. (1969). Recent observations on the surging Otto Glacier, Ellesmere Island. *Canadian Journal of Earth Sciences*, *6*(4), 883-889.

Hugonnet, R., McNabb, R., Berthier, E., Menounos, B., Nuth, C., Girod, L., ... & Kääb, A. (2021). Accelerated global glacier mass loss in the early twenty-first century. *Nature*, *592*(7856), 726-731.

Huss, M. (2013). Density assumptions for converting geodetic glacier volume change to mass change. *The Cryosphere*, *7*(3), 877-887.

Iken, A., & Bindschadler, R. A. (1986). Combined measurements of subglacial water pressure and surface velocity of Findelengletscher, Switzerland: conclusions about drainage system and sliding mechanism. *Journal of Glaciology*, *32*(110), 101-119.

Jiskoot, H., Boyle, P., & Murray, T. (1998). The incidence of glacier surging in Svalbard: evidence from multivariate statistics. *Computers & Geosciences*, 24(4), 387-399.

Jiskoot, H, Murray, T and Boyle, P (2000) Controls on the distribution of surge-type glaciers in Svalbard. *Journal of Glaciology*, 46(154), 412–422.

Jiskoot, H., Murray, T., & Luckman, A. (2003). Surge potential and drainage-basin characteristics in East Greenland. *Annals of Glaciology*, 36, 142-148.

Jiskoot H. (2011) Glacier Surging. In: Singh V.P., Singh P., Haritashya U.K. (eds) *Encyclopedia of Snow, Ice and Glaciers. Encyclopedia of Earth Sciences Series*. Springer, Dordrecht.

Kamb, B., Raymond, C. F., Harrison, W. D., Engelhardt, H., Echelmeyer, K. A., Humphrey, N., ... & Pfeffer, T. (1985). Glacier surge mechanism: 1982-1983 surge of Variegated Glacier, Alaska. *Science*, 227(4686), 469-479.

Kochtitzky, W., Jiskoot, H., Copland, L., Enderlin, E., McNabb, R., Kreutz, K., & Main, B. (2019). Terminus advance, kinematics and mass redistribution during eight surges of Donjek Glacier, St. Elias Range, Canada, 1935 to 2016. *Journal of Glaciology*, 65(252), 565-579.

Kochtitzky, W., Winski, D., McConnell, E., Kreutz, K., Campbell, S., Enderlin, E. M., ... & Jiskoot, H. (2020). Climate and surging of Donjek glacier, Yukon, Canada. *Arctic, Antarctic, and Alpine Research*, 52(1), 264-280.

Koerner, R. M. (2005). Mass balance of glaciers in the Queen Elizabeth Islands, Nunavut, Canada. *Annals of Glaciology*, *42*, 417-423.

Lenaerts, J. T., van Angelen, J. H., van den Broeke, M. R., Gardner, A. S., Wouters, B., & van Meijgaard, E. (2013). Irreversible mass loss of Canadian Arctic Archipelago glaciers. *Geophysical Research Letters*, *40*(5), 870-874.

Luckman, A., Murray, T., & Strozzi, T. (2002). Surface flow evolution throughout a glacier surge measured by satellite radar interferometry. *Geophysical research letters*, *29*(23), 10-1.

Lv, M., Guo, H., Yan, J., Wu, K., Liu, G., Lu, X., ... & Yan, S. (2020). Distinguishing glaciers between surging and advancing by remote sensing: A case study in the Eastern Karakoram. *Remote Sensing*, *12*(14), 2297.

McNabb, R., Girod, L., Nuth, C., & Kääb, A. (2020, May). An open-source toolset for automated processing of historic spy photos: sPyMicMac. In *EGU General Assembly Conference Abstracts* (p. 11150).

Medrzycka, D., Copland, L., Van Wychen, W., & Burgess, D. (2019). Seven decades of uninterrupted advance of Good Friday Glacier, Axel Heiberg Island, Arctic Canada. *Journal of Glaciology*, *65*(251), 440-452.

Meier, M. F., & Post, A. (1969). What are glacier surges? *Canadian Journal of Earth Sciences*, 6(4), 807-817.

Millan, R., Mouginot, J., & Rignot, E. (2017). Mass budget of the glaciers and ice caps of the Queen Elizabeth Islands, Canada, from 1991 to 2015. Environmental Research Letters, 12(2), 024016.

Mouginot, J., Bjørk, A. A., Millan, R., Scheuchl, B., & Rignot, E. (2018). Insights on the surge behavior of Storstrømmen and L. Bistrup Brae, Northeast Greenland, over the last century. *Geophysical Research Letters*, *45*(20), 11-197.

Mortimer, C. A., Sharp, M., & Van Wychen, W. (2018). Influence of recent warming and ice dynamics on glacier surface elevations in the Canadian High Arctic, 1995–2014. *Journal of Glaciology*, 64(245), 450-464.

Müller, F. (1969). Was the Good Friday Glacier on Axel Heiberg Island surging? *Canadian Journal of Earth Sciences*, 6(4), 891-894.

Murray, T., Strozzi, T., Luckman, A., Jiskoot, H., & Christakos, P. (2003). Is there a single surge mechanism? Contrasts in dynamics between glacier surges in Svalbard and other regions. *Journal of Geophysical Research: Solid Earth*, 108(B5).

Nick, F. M., Vieli, A., Howat, I. M., & Joughin, I. (2009). Large-scale changes in Greenland outlet glacier dynamics triggered at the terminus. *Nature Geoscience*, *2*(2), 110-114.

Noël, B., van de Berg, W. J., Lhermitte, S., Wouters, B., Schaffer, N., & van den Broeke, M. R.(2018). Six decades of glacial mass loss in the Canadian Arctic Archipelago. *Journal of Geophysical Research: Earth Surface*, *123*(6), 1430-1449.

Nuth, C., & Kääb, A. (2011). Co-registration and bias corrections of satellite elevation data sets for quantifying glacier thickness change. *The Cryosphere*, *5*(1), 271-290.

Nuttall, A. M., & Hodgkins, R. (2005). Temporal variations in flow velocity at Finsterwalderbreen, a Svalbard surge-type glacier. *Annals of Glaciology*, *42*, 71-76.

O'Neel, S., Pfeffer, W. T., Krimmel, R., & Meier, M. (2005). Evolving force balance at Columbia Glacier, Alaska, during its rapid retreat. *Journal of Geophysical Research: Earth Surface*, *110*(F3).

Ommanney. (1969). *A study in glacier inventory : the ice masses of Axel Heiberg Island, Canadian Arctic archipelago*. McGill University.

Pfeffer, W. T., Sassolas, C., Bahr, D. B., & Meier, M. F. (1998). Response time of glaciers as a function of size and mass balance: 2. Numerical experiments. *Journal of Geophysical Research: Solid Earth*, *103*(B5), 9783-9789.

Raper, S. C., & Braithwaite, R. J. (2009). Glacier volume response time and its links to climate and topography based on a conceptual model of glacier hypsometry. *The Cryosphere*, *3*(2), 183-194.

Raymond, C. F. (1987). How do glaciers surge? A review. *Journal of Geophysical Research: Solid Earth*, *92*(B9), 9121-9134.

Rolstad, C., Amlien, J., Hagen, J. O., & Lundén, B. (1997). Visible and near-infrared digital images for determination of ice velocities and surface elevation during a surge on Osbornebreen, a tidewater glacier in Svalbard. *Annals of Glaciology*, *24*, 255-261.

Schaffer, N., Copland, L., & Zdanowicz, C. (2017). Ice velocity changes on penny ice cap, baffin island, since the 1950s. *Journal of Glaciology*, 63(240), 716-730.

Sevestre, H., & Benn, D. I. (2015). Climatic and geometric controls on the global distribution of surge-type glaciers: implications for a unifying model of surging. *Journal of Glaciology*, 61(228), 646-662.

Sevestre, H., Benn, D. I., Luckman, A., Nuth, C., Kohler, J., Lindbäck, K., & Pettersson, R. (2018). Tidewater glacier surges initiated at the terminus. *Journal of Geophysical Research: Earth Surface*, 123(5), 1035-1051.

Sharp, M. (1988). Surging glaciers: behaviour and mechanisms. *Progress in Physical Geography*, 12(3), 349-370.

Short, N. H., & Gray, A. L. (2005). Glacier dynamics in the Canadian High Arctic from RADARSAT-1 speckle tracking. *Canadian Journal of Remote Sensing*, 31(3), 225-239.

Strozzi, T., Paul, F., Wiesmann, A., Schellenberger, T., & Kääb, A. (2017). Circum-Arctic changes in the flow of glaciers and ice caps from satellite SAR data between the 1990s and 2017. *Remote Sensing*, 9(9), 947.

Sund, M., Eiken, T., Hagen, J. O., & Kääb, A. (2009). Svalbard surge dynamics derived from geometric changes. *Annals of Glaciology*, *50*(52), 50-60.

Thomson, L. I., Osinski, G. R., & Ommanney, C. S. L. (2011). Glacier change on Axel Heiberg Island, Nunavut, Canada. *Journal of Glaciology*, 57(206), 1079-1086.

Thomson, L., & Copland, L. (2016). White Glacier 2014, Axel Heiberg Island, Nunavut: mapped using structure from motion methods. *Journal of Maps*, *12*(5), 1063-1071.

Thomson, L. I., Zemp, M., Copland, L., Cogley, J. G., & Ecclestone, M. A. (2017). Comparison of geodetic and glaciological mass budgets for White Glacier, Axel Heiberg Island, Canada. *Journal of Glaciology*, 63(237), 55-66.

Thomson, L. I., & Copland, L. (2018). Multi-decadal reduction in glacier velocities and mechanisms driving deceleration at polythermal White Glacier, Arctic Canada. *Journal of Glaciology*, 63(239), 450-463.

Urbanski, J. A. (2018). A GIS tool for two-dimensional glacier-terminus change tracking. *Computers & Geosciences*, *111*, 97-104.

Van Wychen, W., Burgess, D. O., Gray, L., Copland, L., Sharp, M., Dowdeswell, J. A., & Benham, T. J. (2014). Glacier velocities and dynamic ice discharge from the Queen Elizabeth Islands, Nunavut, Canada. *Geophysical Research Letters*, 41(2), 484-490.

Van Wychen, W., Davis, J., Burgess, D. O., Copland, L., Gray, L., Sharp, M., & Mortimer, C. (2016). Characterizing interannual variability of glacier dynamics and dynamic discharge (1999–2015) for the ice masses of Ellesmere and Axel Heiberg Islands, Nunavut, Canada. *Journal of Geophysical Research: Earth Surface*, 121(1), 39-63.

Van Wychen, W., Davis, J., Copland, L., Burgess, D. O., Gray, L., Sharp, M., ... & Benham, T. J. (2017). Variability in ice motion and dynamic discharge from Devon Ice Cap, Nunavut, Canada. *Journal of Glaciology*, 63(239), 436-449.

Van Wychen, Burgess, D., Kochtitzky, W., Nikolic, N., Copland, L., & Gray, L. (2021). RADARSAT-2 Derived Glacier Velocities and Dynamic Discharge Estimates for the Canadian High Arctic: 2015-2020. *Canadian Journal of Remote Sensing*, 46(6), 695–714.

Van Wychen, W., Hallé, D. A., Copland, L., & Gray, L. (2022). Anomalous surface elevation, velocity and area changes of Split Lake Glacier, western Prince of Wales Icefield, Canadian High Arctic. *Arctic Science*, (ja).

Van Wyk de Vries, M., & Wickert, A. D. (2021). Glacier Image Velocimetry: An open-source toolbox for easy and rapid calculation of high-resolution glacier velocity fields. *The Cryosphere*, *15*(4), 2115-2132.

Van Wyk de Vries, M. (2021a). Glacier Image Velocimetry (GIV), Zenodo, https://doi.org/10.5281/zenodo.4624831.

Van Wyk de Vries, M. (2021b). Glacier Image Velocimetry (GIV), Zenodo, https://doi.org/10.5281/zenodo.4147589.

Zekollari, H., Huss, M., & Farinotti, D. (2020). On the imbalance and response time of glaciers in the European Alps. *Geophysical Research Letters*, *47*(2), e2019GL085578.

Zemp, M., Huss, M., Thibert, E., Eckert, N., McNabb, R., Huber, J., ... & Cogley, J. G. (2019). Global glacier mass changes and their contributions to sea-level rise from 1961 to 2016. *Nature*, *568*(7752), 382-386.

Appendix A: Map of non-glacierised terrain and of Iceberg Glacier's extent used in section 2.5.1 Mass Redistribution

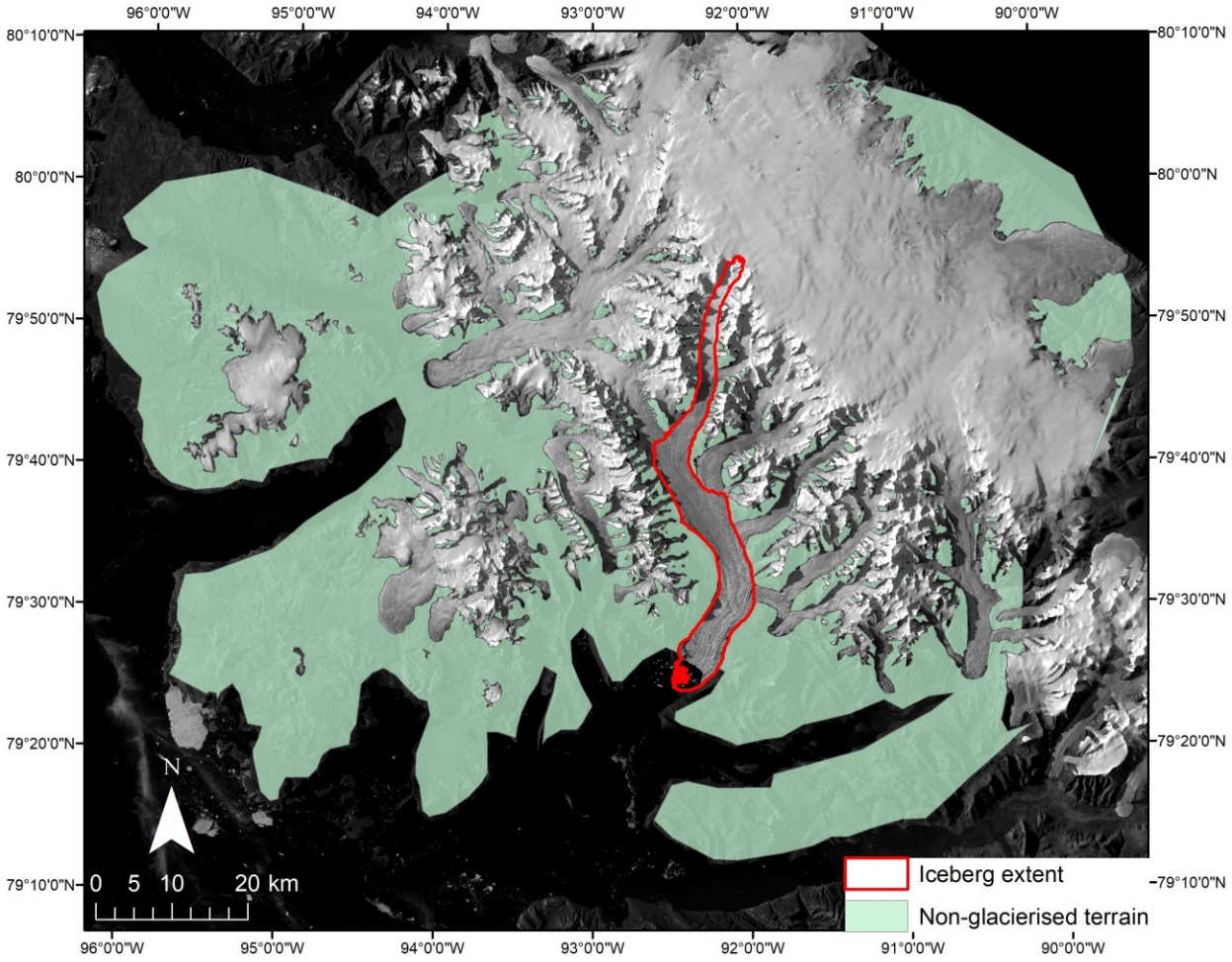

Figure A-1. Distribution of non-glacierised terrain used for the computation of off-ice uncertainties for ice velocity and elevation change data and the extent over which Iceberg Glacier's mass redistribution analysis (Section 2.5.1) was undertaken.